EXPERIMENTAL AND THEORETICAL STUDIES OF

LASER COMPRESSION OF MICROSHELLS

by

Brian James MacGowan

A thesis submitted for the degree of Doctor of Philosophy
of the University of London and for the Diploma of
Membership of Imperial College

October 1982

The Blackett Laboratory
Imperial College of Science and Technology
London SW7 2BZ

ABSTRACT

Research in the application of high intensity laser irradiation to the compression of microshells has shown an advantage in using submicron wavelength lasers. A lower level of preheating of the enclosed fuel gas is expected with shorter wavelength lasers leading to higher compression densities than those observed with one micron wavelength illumination.

Spherically symmetric $\lambda = 0.53$ μm (green) laser light has been used for the first time to implode hollow microspheres containing X-ray emitting seed gases. Two different experiments are described, both use X-ray spectroscopy to determine the implosion core density and temperature. A more sensitive Von Hamos focusing crystal X-ray spectrometer has been developed and used for some of this work.

A comparison experiment has been performed using $\lambda = 1.054$ μm light and a decrease in core density observed.

The use of Argon as a seed gas for density diagnosis of glass microshells is discussed and compared with Chlorine in polystyrene microshells. It is shown that polystyrene targets seeded with Chlorine will allow spectroscopic diagnosis of higher densities than those observable with Argon-doped glass targets.

Theoretical work has centred around using a one-dimensional Lagrangian code (MEDUSA) to simulate the process of material ablation from spherical targets. Comparison with experimental measurements of mass ablation rate has shown that heat fluxes in excess of 10% of the free streaming limit are present in the ablation plasma. This deduction disagrees with previous work indicating a maximum possible heat flow of 3% of free streaming.

Dedicated to my parents

ACKNOWLEDGMENTS

The work described in this thesis was carried out while the author was a member of the Plasma Physics Group at Imperial College.

The author would like to thank Dr. J. D. Kilkenny (his supervisor) for providing encouragement and guidance throughout this work. The author is grateful for fruitful discussion with Dr. R. G. Evans and Dr. M. H. Key of Rutherford Appleton Laboratory.

He would like to acknowledge the cooperation of Dr. D. J. Bond, D. K. Bradley, Dr. T. J. Goldsack, Dr. J. D. Hares and Dr. R. W. Lee of Imperial College and Dr. P. T. Rumsby of Rutherford. This work would not have been possible without the support of the staff of Rutherford Appleton Laboratory Central Laser Facility in target preparation, target area and laser control.

The author would like to thank KMS Fusion Inc. for making it possible for him to visit and perform an experiment using their laser system. Thanks are due to Dr. J. A. Tarvin, D. Sullivan and Dr. D. Slater as well as the bunker and laser teams.

The work in this thesis was performed whilst the student was supported by a Science and Engineering Research Council grant.

Special thanks go to Mrs. Diana Beydoun for typing this manuscript.

UNITS

S.I. units have been used in this work except where convention requires the use of alternatives. Occasionally a unit has been chosen as particularly relevant to the scale of the system being considered, e.g. specific energy depositions are quoted in J/ng (1 ng $\equiv 10^{-12}$ Kg). Temperatures are usually given in eV (1 eV $\equiv$ 1.16 10^4 Kelvin). Pressures are normally quoted in Mbar (10^6 atmospheres $\equiv 10^{11}$ Pascals). X-ray photon energies are in units of eV or keV (10^3 electron volts), whilst wavelengths are quoted in either μm (10^{-6} metre) or Å (10^{-10} metre) depending on the wavelength (laser or X-ray) being considered. In all cases where non-S.I. units are used the units are specified.

CONTENTS

LIST OF SYMBOLS

Roman

2d	Twice lattice spacing in Bragg reflecting crystal
Be	Beryllium
CsI	Caesium Iodide
D	X-ray source diameter
E_{abs}	Absorbed energy
E_F	Fraction of incident energy converted to fast electrons
E_{fe}	Specific energy deposition due to fast electrons
E_K	Energy required to ionise electron from K shell
E_r	Specific energy deposition due to radiation
E_s	Specific energy deposition due to shock heating
f	Fraction of free streaming heat flux
f	Fraction of target mass ablated by laser
f_x	Fraction of absorbed energy converted to soft X-rays
F	Form factor
F_r	Fraction of incident energy converted to soft X-ray radiation
G	Pressure amplification factor
h	Planck's constant
I_{abs}	Absorbed laser irradiance
I_{inc}	Incident laser irradiance
I_{13}	Absorbed laser irradiance (units 10^{13} W cm^{-2})
I_{14}	Absorbed laser irradiance (units 10^{14} W cm^{-2})
k, k_B	Boltzmann's Constant
k_0	Free space wave number of laser

ℓ	Separation of plasma from streak camera cathode
L	Density scale length of sub-critical region
$\dot{m}$	Mass ablation rate in 4π steradians
m_e	Electron mass
m_0	Initial target mass
$\dot{m}_s$	Specific mass ablation rate (per unit area)
$\dot{m}_s^X$	Specific mass ablation rate from time-resolved X-ray measurement
$\dot{m}_s^I$	Specific mass ablation rate from ion measurement
n_e	Electron number density
n_c	Critical electron number density
P	Pressure
P_a	Ablation pressure
P_f	Stagnation pressure of compressed core
q_{sat}	Saturated heat flux
R	Initial microballoon radius
r_c	Radius of curvature of curved crystal
R_f	Final radius of compressed core
S	Target surface area
S	Distance shell has accelerated
T_c	Cold electron temperature
T_e	Electron temperature
T_f	Final temperature of compressed core
T_h, T_H	Hot electron temperature
U	Laser power deposition rate (units Watts/Kg)
V_i	Ion ablation velocity
$\overline{v}_i, \overline{v}$	Mean ion ablation velocity
v_s	Sound speed

z	Nuclear charge
$\langle z \rangle$	Mean ion charge
$\langle z^2 \rangle$	Mean squared ion charge

Greek

β	Bragg reflecting crystal rocking angle
γ	Ratio of specific heats
ΔR	Initial thickness of shell
Δr_{CH}	Initial thickness of plastic layer
ε	Plasma dielectric constant
ε_0	Permittivity of free space
η_{fe}	Fraction of incident energy converted to fast electrons
η_ν	X-ray radiation conversion fraction for frequency range ν to $\nu + d\nu$ (units photons J^{-1} Hz^{-1})
λ	Wavelength
λ_0	Free space wavelength of laser
λ_0	Wavelength at curved crystal focus
λ_D	Debye length
λ_h	Fast electron range
$\lambda_{\mu m}$	Laser wavelength (units 10^{-6} m)
μ	Refractive index
ν	Frequency (Hz)
ρ	Density
ρ_c	Critical mass density
ρ_{CH}	Density of plastic layer
ρ_f	Final density of compressed core
ρ_i	Initial density of fill gas
ρ_s	Initial density of shell

τ_L Laser pulse duration (Full Width at Half Power Points)

ω Angular frequency (rad s^{-1})

ω_{pe} Electron plasma frequency

LIST OF FIGURES

CHAPTER 1

LASER COMPRESSION

1.0 Abstract

The process of laser compression and phenomena relevant to laser compression are briefly described. An outline of the thesis is given, emphasising the role of the author in the work. The use of laser compression in inertial confinement fusion is described.

1.1 Introduction

The concept of using a short duration high power laser pulse to compress microspheres to high density was first introduced publicly by Nuckolls and co-workers[1.01] in 1972. They proposed using MJ laser energies in nanosecond pulses to irradiate sub-millimetre diameter spheres. The pressure produced by ablation of the target surface by the laser would compress the target leading to the production of densities of the order of 1000 g cm^{-3}. Suggested applications for laser compression are the study of hot matter at densities comparable to those in the centre of the sun (Temperature $\sim$ keV, Density $\sim$ 200 g cm^{-3}), and the production of the conditions necessary for controlled thermonuclear power production. This latter application involves the compression and heating of hydrogen isotopes to thermonuclear ignition temperature (several keV) at high density in order to obtain a net power gain. Scaled-down experiments, using lower energies than those required for a fusion reactor, should produce hot matter of sufficiently high densities (> 10 g cm^{-3}) to be interesting.

Early work in laser compression has relied on high intensity exploding pusher implosions of microshells to obtain hot cores of low density (< 1 g cm^{-3}). Ablative implosions have been attempted relatively recently and are the subject of one of the Chapters in this thesis.

1.2 The Role of the Author/Summary of Thesis

This thesis describes work carried out by the author in the period October 1980 to July 1982. This chapter serves as an introduction to the thesis.

Chapter 2 describes two experiments, at different laser pulse lengths, using a single beam to irradiate planar targets. The observation is made of significant energy flowing laterally away from the focal spot. These experiments were performed with the aid of three co-workers. The author's contribution to the work was the time resolution of the spreading of energy for both pulse lengths as well as the first observation of spreading in the short pulse experiment, using a large aperture pinhole camera (e.g. Fig. 2.6).

Chapter 3 describes the development of a curved crystal focusing X-ray spectrometer for use with X-ray streak cameras. The spectrometer offers a significant gain over more conventional flat crystal instruments used previously at Rutherford Laboratory. The development of this diagnostic to the point of routine usage was entirely the work of the author.

Chapter 4 combines a discussion of the factors relevant to the ablative implosion of microshells, with a description of the first such implosions attempted using symmetric illumination by six $\lambda = 0.53$ μm beams. The X-ray diagnosis of this experiment, the data analysis and subsequent conclusions regarding preheat are the author's work. The detection of nuclear reaction products from the implosions was the work of members of the Rutherford Laboratory staff and workers from Bristol University.

Chapter 5 reports the results of two experiments pertinent to the previous chapter. The experiment was performed at KMS Fusion Inc. using their TBIS symmetric illumination system to irradiate microballoons with 0.53 μm light. These quasi-exploding pusher implosions allowed core density diagnosis by seed gas spectroscopy.

The remainder of Chapter 5 briefly describes a comparison experiment using 1.054 μm irradiation performed at Rutherford Appleton Laboratory. Conclusions are reached about the use of Argon-doped glass microballoons for density diagnosis of ablative implosions. It is suggested that for high ρR implosions, plastic microballoons with a Chlorine component in the fill gas will allow easier spectroscopic diagnosis of core density and temperature.

Chapter 6 details the modification and use of the one-dimensional hydrodynamic code MEDUSA. The program is used to simulate spherical geometry mass ablation rate experiments carried out at Rutherford Laboratory. Comparison of the code results with experiment leads to the conclusion that heat fluxes in excess of 10% of free streaming are present in the experiment. The experimental data used for the comparison was obtained by other workers (see ref. 6.27). The modification and use of MEDUSA was entirely the work of the author.

Chapter 7 draws together the conclusions of the thesis and atempts to indicate short term objectives in the achievement of high density matter by laser compression.

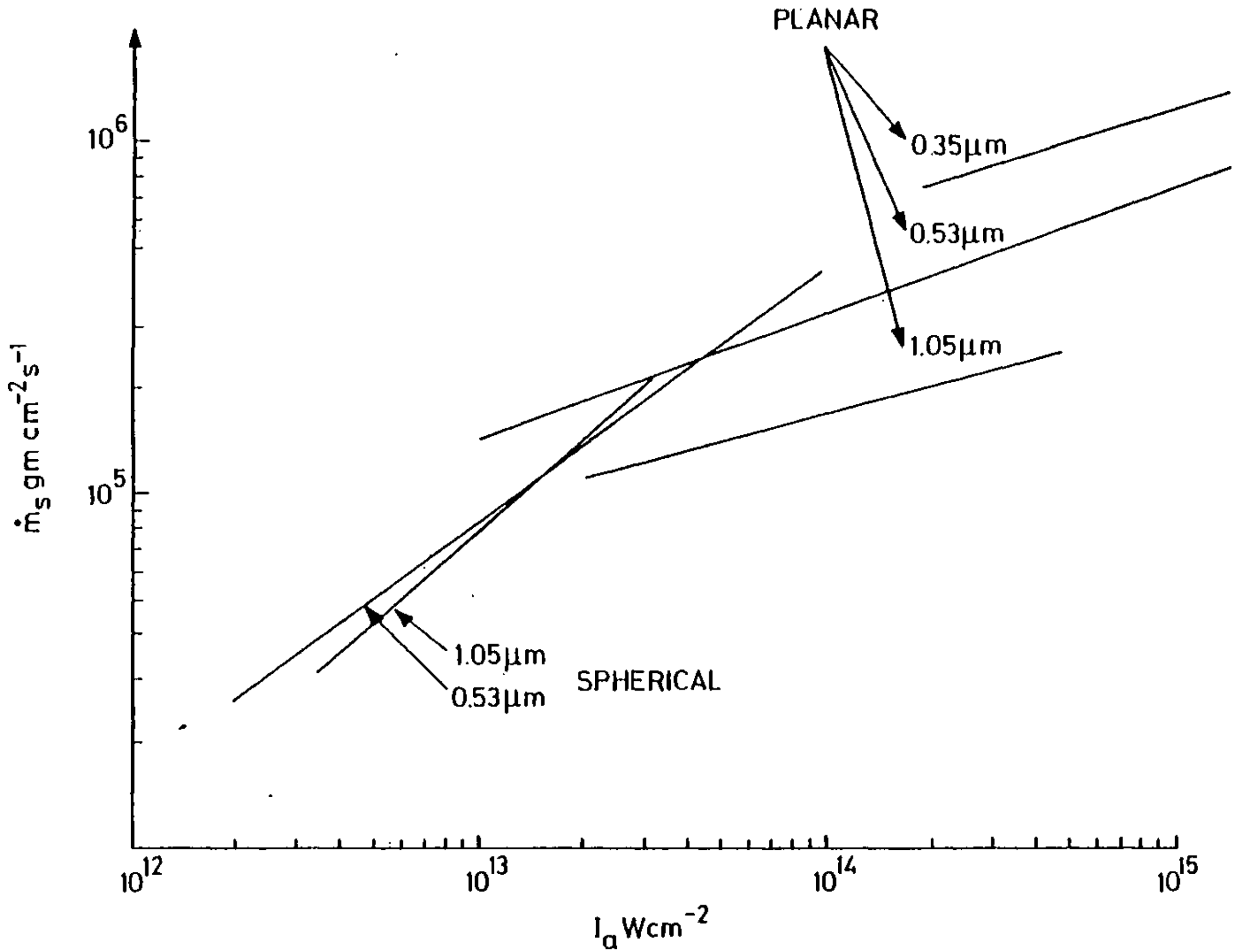

Fig. 1.1. Compilation of planar and spherical geometry mass ablation rate data for three wavelengths (refs. (1.03) and (1.04)).

1.3 The Physics of Laser-driven Compression

1.3.1 Ablation

When energy is absorbed by the surface of a target the heated material produced responds to its own pressure by moving away from the target (ablating). The rate at which mass leaves the target can be defined as a mass ablation rate $\dot{m}$ (Kg s^{-1}), or specific mass ablation rate per unit area $\dot{m}_s$ (Kg m^{-2} s^{-1}).

The pressure at the target surface causing the ablation of mass is termed the ablation pressure P_a. The material ablated is accelerated by the pressure gradient near the surface and achieves an asymptotic flow velocity v_i away from the target. The measurement of the mean ion flow velocity $\overline{v}_i$ and the specific mass ablation rate $\dot{m}_s$ allow the ablation pressure to be determined(1.02). Equating the outward momentum flux to the pressure at the target surface we get the 'rocket equation'

$$P_a = \dot{m}_s \overline{v}_i \tag{1.01}$$

The ability to predict the ablation pressure for particular conditions of laser wavelength and irradiance is required in order to plan compression experiments. Much work(1.03)(1.04)(1.05)(1.06)(1.07) has been done to measure mass ablation rates and ion ablation velocities in both planar and spherical geometry. Wavelength scaling of ablation rate has been examined in planar geometry(1.03)(1.05)(1.06)(1.07) and to a lesser extent in spherical geometry(1.03)(1.04). Fig. 1.1 is a compilation of planar and spherical geometry mass ablation rate data (1.03)(1.04). The planar geometry results scale only weakly with absorbed irradiance ($\dot{m}_s \propto I_{abs}^{0.3}$) but strongly with laser wavelength.

Spherical geometry results scale only weakly with laser wavelength but strongly with absorbed irradiance ($\dot{m}_s \propto I_{abs}^{0\cdot 8}$). The difference in scaling between planar and spherical experiments has been attributed(1·07) to lateral transport of energy away from the laser focal spot used in the planar measurements. Lateral transport becomes more significant at longer wavelength and higher irradiance (1·07) and therefore can explain the planar $\dot{m}_s$ curves of Fig. 1.1 lying below the values indicated by the spherical $\dot{m}_s$ curves.

Some analytic models for steady state ablation(1·08)(1·09) indicate a more rapid scaling of $\dot{m}_s$ with wavelength than is implied by the spherical geometry $\dot{m}_s$ curves of Fig. 1.1. However these models assume that the laser absorption occurs at one point only (critical density) on the density profile. This assumption becomes incorrect as shorter wavelengths are used due to collisional absorption in the ablation plasma. The region of absorption is then spread over the density profile and thus the mass ablation rate is below that predicted by the models(1·08)(1·09). The lack of scaling of spherical $\dot{m}_s$ with wavelength for the two wavelengths shown in Fig. 1.1 has been confirmed in computer simulations described in Chapter 6 of this thesis.

1.3.2 Absorption of laser light

There are several absorption processes occurring in a laser-irradiated material: two of the more relevant processes will be described.

1.3.2.1 Resonance absorption. As laser light incident at an angle θ_0 to a plasma density gradient propagates up the gradient it is refracted and finally reflected at a density $n_c \cos^2\theta$ (see Chapter 2, Section 2.1.1) where n_c is the critical electron number density defined by

$$n_c = \frac{\varepsilon_0 m_e}{e^2} \omega^2 = 1.12 \; 10^{27} \lambda_{\mu m}^{-2} \qquad m^{-3} \qquad (1.02)$$

where ω is the laser angular frequency and $\lambda_{\mu m}$ its wavelength in microns. If the E field of the laser has a component in the plane of incidence an evanescent wave can excite a plasma wave at critical density. The wave is damped and energy is fed into a small number of electrons which are accelerated to high energy(1.10)(1.11). These 'hot' or 'suprathermal' electrons can be characterised by a temperature T_H which can be typically over 10 keV(1.11). The production of fast electrons by resonance absorption is particularly important for short pulse ($\sim$ 100 psec) high intensity ($\sim 10^{16}$ W cm^{-2}) exploding pusher implosions.

1.3.2.2 Inverse bremsstrahlung absorption. The process of inverse bremsstrahlung occurs when ions and electrons accelerated by the laser electric field collide, the electron taking away a quantum of laser energy. The inverse bremsstrahlung absorption coefficient can be expressed(1.12) as:

$$K = 13.5 \frac{\langle z^2 \rangle}{\langle z \rangle} \frac{\ell n \Lambda(\nu)}{\lambda^2 \, T_e^{3/2}} \left[\frac{n_e}{n_c}\right]^2 \frac{1}{\left[1 - \frac{n_e}{n_c}\right]^{1/2}} \quad m^{-1} \qquad (1.03)$$

with all units S.I. This expression has been derived for the limit where the electron-ion collision frequency is much lower than the laser frequency ν, which is valid in the underdense hot ablation plasma.

The quantity $\Lambda(\nu)$ is defined as:

$$\Lambda(\nu) = \mathrm{Min}\ \{ \frac{v_T}{\omega_{pe}\ p_{min}} , \frac{v_T}{\omega\ p_{min}} \} \qquad (1.04)$$

where p_{min} is the minimum impact parameter for electron ion collisions.

$$p_{min} \simeq \mathrm{Max}\ \{ \frac{Ze^2}{4\pi\varepsilon_0 kT} , \frac{h}{\sqrt{m_e\ kT}} \} \qquad (1.05)$$

v_T is the electron thermal velocity. For absorption in the low density ablation plasma, the laser angular frequency ω is always larger than the electron plasma frequency ω_{pe}.

Inverse bremsstrahlung is most effective at low irradiance ($\lesssim 10^{13}$ W cm^{-2}) and short wavelength ($\lesssim 1$ μm). At high irradiance for low Z targets inverse bremsstrahlung becomes insignificant and resonance absorption dominates.

1.3.3 Energy transport

All absorption of the laser energy takes place at critical density and at lower densities. The ablation of material from the target surface takes place at higher density than critical density. The transport of energy between the absorption and ablation regions is therefore of importance to the process of ablation.

1.3.3.1 Thermal/flux-limited transport. The thermal transport of energy by electrons has been calculated by Spitzer(1.13)(1.14) and Braginskii(1.15) in the limit of classical collisions. The calculations are valid only for temperature scale lengths much larger than the electron mean free path.

In the region separating critical density from the target surface temperature gradients are such that the temperature scale length is comparable to the electron mean free path. The thermal energy conduction of the plasma must then be described by a more complete theory than that of Spitzer[1.14]. An absolute limit on the heat conduction of a plasma is set at the so-called 'free streaming' heat flux. This is the flux when all the electrons are travelling in the same direction with the thermal velocity. The saturation flux q_{sat} is:

$$\underline{q}_{sat} = - n_e k_B T_e \sqrt{\frac{k_B T_e}{m_e}} \frac{\underline{\nabla} T_e}{|\underline{\nabla} T_e|} \tag{1.06}$$

Heuristically saturation of heat flow would be expected at some fraction f of the free streaming flux. Two independent theories [1.16][1.17] show that heat flow can saturate at values of $f \gtrsim 0.1$.

Although a lot of evidence exists for a low value of f, i.e. $f \sim 0.03$, much of it is taken from early experiments whose interpretation could be changed by considering lateral energy transport and/or fast electron production. More recently experiments other than those described in Chapter 6 of this thesis[1.18] have demonstrated heat fluxes of 10% of free streaming in a non-turbulent plasma.

<u>1.3.3.2 Fast electron transport</u>. Suprathermal electrons produced in the absorption region of the target can deposit their energy at high density. This process is undesirable as fast electron transport will preheat the target, increasing its entropy, prior to compression hence reducing the compression achieved. Much experimental measurement of hot electron temperature (T_H) and range (λ_h) has been done[1.19][1.20].

For low Z targets (e.g. glass or plastic) a formula for the scale depth of energy deposition can be obtained by scaling experimental data[1.19] to get[1.20]

$$(\rho\lambda)_h \;\approx\; 1.8\ 10^{-4} \left[\frac{I_{inc}}{10^{14}\ \mathrm{W\ cm^{-2}}}\ \lambda^2_{\mu m}\right]^{0.9} \qquad \mathrm{g\ cm^{-2}} \tag{1.07}$$

The quantity $(\rho\lambda)_h$ is approximately constant[1.20] for a particular material although there is some Z dependence due to increased scattering of electrons for high target element Z[1.19].

The transport of fast electrons into a target requires a return current of cold electrons to maintain charge neutrality. The electric field set up to drive the cold electron return current can impede the motion of fast electrons. This process is known as resistive inhibition and has been proposed as a method of reducing preheat due to fast electron transport[1.22]. Resistive inhibition is found to be more significant for low density gold foam of 0.6% solid density than for the equivalent areal density of solid gold[1.22][1.23]. The reduction in fast electron range by a factor of 2 or 3 in the gold foam compared with solid gold makes it a possible material to use as a screen to prevent fast electron preheating of the rest of the target[1.23].

1.3.3.3 Radiation transport. Transfer of energy by X-ray radiation can be an important factor in laser irradiated targets. Preheating of the target by radiation from the ablation region can be inferred from measurements of the soft X-ray spectrum emitted by the ablation plasma [1.24]. Radiation transport calculations have been used to predict the X-ray spectrum emitted from targets[1.25].

1.3.3.4 Shock waves. The ablation pressures observed in laser irradiated targets are of the order of 10 Million atmospheres (Mbar) sufficient to drive a strong shock into the target. Hugoniot data for strong shocks propagating through many materials has been compiled (1.26) and shows that shock waves can contribute to preheating the target.

1.3.4 Shell implosions

Two mechanisms have been studied for the laser compression of a spherical shell. They are the so-called 'exploding pusher' and ablative modes of compression.

1.3.4.1 Exploding pusher compression. If the scale length λ_h for fast electron energy deposition is large compared with the shell thickness, the shell is uniformly heated by fast electrons. The shell then explodes due to the internal pressure generated by the sudden deposition of energy. Half the shell (or 'pusher') explodes inwards towards the centre of the sphere, the other half explodes outwards. The half of the pusher that moves inwards compresses and heats the fill gas. This process has been modelled by several workers[(1.27)(1.28)(1.29)]. The compressed cores produced by exploding pusher implosions are as the result of an adiabatic compression of a shock and fast electron preheated gas. The resulting compressed densities observed are therefore quite low ($\sim$ 0.5 g cm^{-3}) [(1.30)].

1.3.4.2 Ablative compression. In the absence of preheating the compression of material contained in a microshell can be achieved by ablatively accelerating the shell inwards. The compression then occurs on or near the isentropic Fermi-degenerate adiabat[(1.01)]. The realisation of a low preheat compression would probably require the use of a thick-walled microshell and a short wavelength laser. The short wavelength would be used in order to minimise fast electron preheat which is dependent on $I\lambda^2$ (1.31)(1.11). A simple model using shock wave heating as the dominant preheat mechanism has been proposed(1.21).

Experiments attempting to produce high densities ablatively have either used λ = 1.06 μm lasers to irradiate thick-walled plastic-coated shells(1.32)(1.33) or λ = 0.53 μm light to irradiate medium-thickness shells (Chapter 4 of this thesis).

1.3.5 Limits to compression

Preheat, as has already been mentioned, degrades the efficiency of a compression by increasing the fill gas temperature and decreasing the pusher density by decompression.

Other limitations on the density achievable in an implosion are illumination uniformity and fluid instabilities.

1.3.5.1 Thermal smoothing. The shell velocity uniformity required during implosion can be shown to be about 3% if a volumetric compression ratio of 1000 is to be achieved(1.34). Irregularities in illumination will produce non-uniformity in the accelerated shell velocity unless the irregularities are smoothed out by thermal conduction between the absorption and ablation regions. Recent theoretical(1.34)(1.35) and experimental work(1.36) indicates that for $I\lambda^2$ above 10^{14} W cm^{-2} μm^2 absorbed, significant smoothing of illumination non-uniformity will occur. However no experiments regarding thermal smoothing have been carried out in spherical geometry with an accelerating shell in order to determine smoothing efficiencies in actual implosions.

1.3.5.2 Fluid instabilities. Fluid instabilities during the acceleration phase of an implosion can drastically reduce the spherical convergence of the shell, hence degrading the compression. The most worrying instability is the Rayleigh-Taylor instability excited when the high density shell is accelerated by a low density ablation region.

The behaviour of the instability is analogous to instability in a layer of dense liquid overlaying a lighter liquid under gravity. The condition for unstable growth of any irregularity in the shell's mass distribution is that ∇P and $\nabla \rho$ point in opposite directions. This condition is satisfied in the ablation region of an accelerating shell.

Some experiments using corrugated 'planar' targets to excite instabilities deliberately have been performed[1.37].

1.4 Inertial Confinement Fusion

Inertial confinement by means of laser compression has been proposed[1.01] as a means of confining and heating a source of thermonuclear power.

1.4.1 Fusion reactions

Exothermic reactions that could be used in a fusion reactor to generate power are:

$$D + T \rightarrow {}^4He\ (3.5\ MeV) + n(14.1\ MeV) \tag{1.08}$$

$$D + D \begin{cases} \nearrow T(1\ MeV) + H(3\ MeV) \\ \searrow {}^3He\,(0.8\ MeV) + n(2.5\ MeV) \end{cases} \tag{1.09}$$

Power would be extracted from the reactor by allowing neutrons to be thermalised in a balnket surrounding the reactor vessel.

1.4.2 Ignition

Although neutrons will escape the target, other reaction products such as α particles (Helium nuclei) will deposit their energy within the target heating it up. Losses due to bremsstrahlung radiation from the fuel are balanced by energy production from reaction products at the ignition temperature. For the D-T reaction the ignition temperature is 4 keV, whilst for the D-D reaction it is 35 keV. Heating the compressed fuel to the ignition temperature will result in a self-sustaining 'burn' of the fusion fuel limited in duration by the confinement time of the compressed plasma.

1.4.3 Confinement, the Lawson Criterion

The Lawson Criterion[1.38] is a requirement that the ion number density confinement time product ($n\tau$) must satisfy in a fusion reactor operating with a net power gain. The criteria are:

$$n\tau \gtrsim 10^{14} \text{ cm}^{-3} \text{ sec for D-T} \qquad (1.10)$$

and

$$n\tau \gtrsim 10^{16} \text{ cm}^{-3} \text{ sec for D-D} \qquad (1.11)$$

The problem in controlled thermonuclear fusion power production is therefore to reach the ignition temperature and then confine the plasma long enough to satisfy the $n\tau$ requirement.

In the inertial confinement approach to fusion the fuel is compressed to high density and then is 'confined' at that density for a finite time due to its own inertia. The confinement time is then determined by the ion thermal velocity of the fuel at ignition temperature and the dimension of the compressed fuel. The Lawson Criterion can then be translated to be a requirement on the density radius product R of the compressed sphere when it is at ignition temperature. For D-T the requirement is:

$$\rho R \ > \ 1 \text{ g cm}^{-2} \tag{1.12}$$

CHAPTER 2

TIME RESOLUTION OF LATERAL ENERGY FLOW IN PLANAR TARGETS

2.0 Abstract

Observations are made of lateral energy loss from the focal area of plane targets irradiated with a single laser beam. Fast electrons, probably produced by resonance absorption, are seen to take their energy sideways several millimetres away from the laser focal spot. Differences in the velocity of sideways energy flow are measured for two different laser pulse lengths of 1.3 nanosecs and 80 picosecs.

2.1 Introduction

When an intense laser beam is incident on a solid target a fraction of its energy is absorbed in the dense plasma cloud which is produced during the interaction. At high irradiance a large fraction of the energy absorbed is given to producing very fast 'supra-thermal' electrons. In a plane target experiment these high energy electrons may carry energy several millimetres away from the focal spot. The lateral flow of energy may make planar geometry experiments become two-dimensional in nature.

The two experiments which will be described used intense pulses of λ = 1.054 μm light to illuminate a small ($\sim$ 50 μm diameter) focal spot. The movement of fast electrons along the target surface was monitored by time and space resolving the Kα emission from the target material using an X-ray streak camera.

2.1.1 Resonance Absorption

Laser energy incident on a target surface encounters a plasma density gradient leading up to solid density. As the laser propagates up the density gradient it is attenuated by collisions between electrons and ions driven by the laser field (inverse bremsstrahlung absorption). The laser energy not absorbed by inverse bremsstrahlung will be reflected when the electron plasma frequency ω_{pe} is equal to the laser frequency.

$$\omega = \omega_{pe} = \left[\frac{n_e \, e^2}{\varepsilon_0 \, m_e}\right]^{\frac{1}{2}} \quad \text{rad s}^{-1} \tag{2.01}$$

The real part of the plasma dielectric constant,

$$\varepsilon_r = 1 - \frac{\omega_{pe}^2}{\omega^2} \tag{2.02}$$

then goes to zero so the laser is reflected. The electron density at which reflection occurs is called the critical density.

$$n_c = \frac{\varepsilon_0 \, m_e}{e^2} \omega^2 \qquad \text{m}^{-3} \tag{2.03}$$

$$n_c = 1.12 \; 10^{27} \; \lambda_{\mu m}^{-2} \qquad \text{m}^{-3} \tag{2.04}$$

where $\lambda_{\mu m}$ is the free space laser wavelength in microns. If a fully ionised plasma with ions of mass number $A \approx 2Z$ is considered then:

$$\rho_c = 3.7 \; \lambda_{\mu m}^{-2} \qquad \text{kg/m}^3 \tag{2.05}$$

In general the laser will not be incident normal to the target surface but at an angle θ_0 to it. The plasma refractive index is a function of electron number density.

$$\mu \simeq \sqrt{1 - \frac{n_e}{n_c}} \tag{2.06}$$

The beam will therefore be refracted as it moves up the density gradient. The restriction, $\mu \sin \theta$ = constant, applies to the beam path if the density gradient is planar, therefore the beam will be reflected at a density:

$$n_e = n_c \cos^2 \theta_0 \tag{2.07}$$

The reflection point has therefore moved to a lower density than critical density. Fig. 2.1 illustrates the refraction and reflection of the laser by the density gradient.

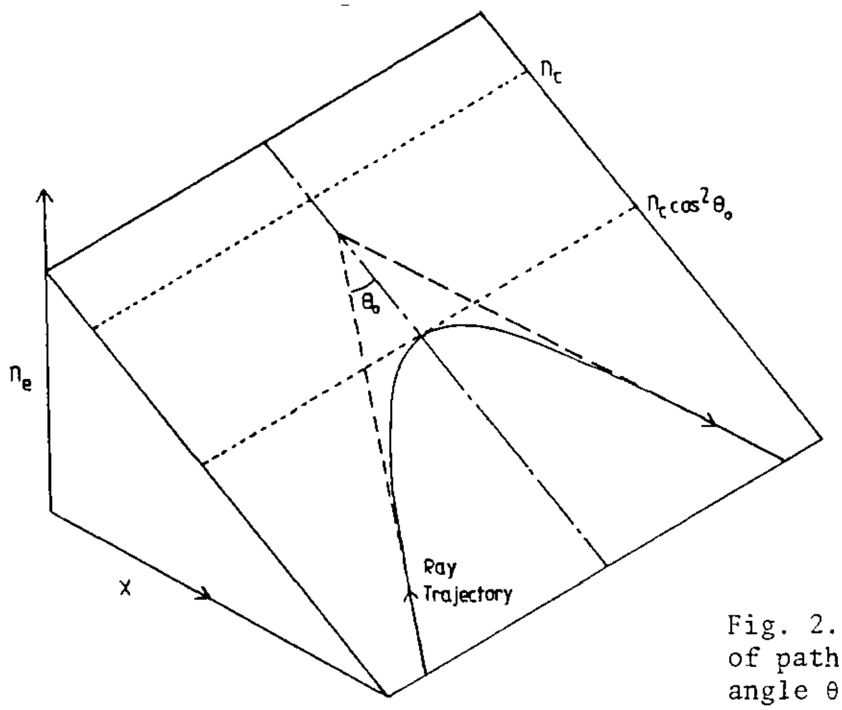

Fig. 2.1. Representation of path of ray incident at angle θ_0 to density gradient.

If the $\underline{E}$ field of the laser has a component in the plane of incidence (i.e. a p polarised component) the $\underline{E}$ field will point up the density gradient at the reflection point. Resonance absorption of laser energy occurs when the electric field of the laser resonates with the electron gas at the plasma frequency ω_{pe} and drives an electrostatic plasma wave. Energy is transferred from the wave to the electrons around critical density by wave breaking. The electrons oscillate in the x direction with amplitude $\xi(x)$ driven by the laser electric field of amplitude E.

$$\xi(x) = \frac{\varepsilon_0 E}{e\, n_c} \frac{1}{\left[1 - \frac{n_e}{n_c} - \frac{i\nu}{\omega}\right]} \quad \mathrm{m} \tag{2.08}$$

The collision term $\frac{\nu}{\omega}$ is small for the densities being considered (e.g. critical density for $\lambda = 1\ \mu\mathrm{m}$ light). Therefore there is a region near critical density where:

$$\left| \frac{d\xi(x)}{dx} \right| > 1 \tag{2.09}$$

which is the condition for wave breaking. The energy in the wave is then absorbed by the electrons at critical density.

If the laser is incident at an angle to the density gradient it is not immediately obvious that resonance absorption can occur since the beam never gets to critical density. Theoretical studies of electromagnetic waves reflecting off a plasma density gradient(2.01) have shown that if the incident wave has a p polarised component of $\underline{E}$ field then resonance absorption can occur. On reflection at $n_e = n_c \cos^2 \theta_0$ the $\underline{E}$ field of the wave can tunnel through the plasma and be non-zero at critical density hence driving the resonant plasma wave there. Simulations have indicated that typically 20% of the incident laser power can be absorbed at critical density by resonance absorption (2.02).

2.1.2 Hot Electron Production

Experiments using Neodynium YAG (1.06 μm) and CO_2 (λ = 10.6 μm) lasers to irradiate plane targets at high intensity (> 10^{14} W cm^{-2}) led to the observation of high energy X-ray emission characteristic of significant numbers of very energetic electrons. These 'fast electrons' had a distribution function corresponding to a temperature ($T_H \gtrsim$ 5 keV) far in excess of the plasma electron temperature of typically $T_c \sim$ 0.5 keV[2.03]. Detailed modelling of the interaction of the laser with the electron population near critical density has shown that the resonantly-absorbed laser energy produces a relatively small number of very high energy 'hot' electrons. These electrons form a high energy tail to the 'cold' electron distribution function characteristic of the local plasma temperature T_c[2.01][2.02].

As a consequence of their method of production, the initial motion of the hot electrons is down the density gradient away from the target. The outward-going electrons are reflected at the plasma sheath marking the limit of ion motion away from the target. Space charge effects prevent most of the electrons going beyond the sheath and they are turned around and sent back up the density gradient. The sheath is moving away from the target surface so the electrons give up energy to the ions on reflection. The velocity spectrum of the accelerated ions has been measured and the temperature T_H of the hot electrons inferred [2.04].

It has been observed that T_H is a function if $I\lambda^2$, where I is the incident laser intensity[2.05], but is virtually independent of laser pulse length in the range 80 picoseconds - 2 nanoseconds[2.06]. Evidence exists[2.07][2.08][2.09][2.10] that although T_H is almost constant with pulse length, the fraction E_F of incident energy coupling into fast electrons decreases with increasing pulse length. Values of E_F = 5% to 17% for short pulses ($\sim$ 80 picoseconds) and $E_F \lesssim$ 2% for long pulses ($\sim$ 300 picoseconds) at wavelengths of 1.054 μm and 1.3 μm have been observed(2.11).

2.2 Diagnostics

Two separate experiments were performed with laser pulse lengths of 1.3 nanoseconds and 80 picoseconds using λ = 1.054 μm light. A 50 μm to 200 μm diameter focal spot was illuminated on a plane target and the motion of the fast electrons produced inferred from the Kα emission of the target material.

2.2.1 Kα Production

Kα radiation is emitted by an atom as a consequence of the loss of a K shell electron through ionisation. Radiation or electron collision can supply the energy required for ionisation. Radiation is the more efficient when the photon energy $h\nu$ is greater than the K shell ionisation potential E_K. The X-ray continuum emission from laser plasmas if of the form

$$I(\nu) \sim e^{-\frac{h\nu}{kT_c}} \tag{2.10}$$

for $h\nu >> kT_c$, where T_c is a slowly varying function of $h\nu$.

Here T_c is the 'cold' background electron temperature which is typically 500 eV under the focal spot in the experiments to be described. Hence to use Kα emission as a diagnostic of hot electron energy we must have $kT_c << E_K$. Therefore the target material must be chosen such that E_K >> 500 eV. The target elements used in the experiments all had $E_K \sim 5$ keV so that radiation pumping of Kα could be neglected.

2.2.2 Differential Filters

To image low intensity Kα emission over a large (∼ 5 mm diameter) area of the target an X-ray pinhole camera with a large collecting aperture was used. Pinholes of ∼ 0.5 mm diameter were used in pairs covered by two different filtering materials. The filtering elements were chosen to form a Ross pair. One filter has its K absorption edge at slightly higher energy than the Kα being observed. This filter will transmit the Kα, but radiation of higher energy, in particular the bright resonance lines emitted from Hydrogen and Helium-like ions in the ablation plasma, will be strongly attenuated. The second filter has its K edge at slightly lower energy than the Kα, leading to an image without Kα. Comparison of the two pinhole images gives a two-dimensional record of the regions on the target producing Kα.

Fig. 2.2 shows the transmission of two filters which were used as a Ross pair. They are 12.5 μm of Titanium and 25 μm of Scandium which were used for observing the Kα of Vanadium.

The difference in transmission for the two filters is a factor of 100 for Vanadium Kα. Taking the transmissions and integrating them for a continuum of the form $I_0\, e^{-\frac{h\nu}{KT_H}}$ gives a ratio in total transmitted photons of 1.5 for $T_H \sim 10$ keV. The differential filters therefore distinguish Kα emission from continuum emission.

2.2.3 Time resolution of Kα

The targets were positioned angled so that the laser was incident at 6° to the normal to the surface. The focal spot could therefore be viewed, along a line perpendicular to the laser, by an X-ray streak

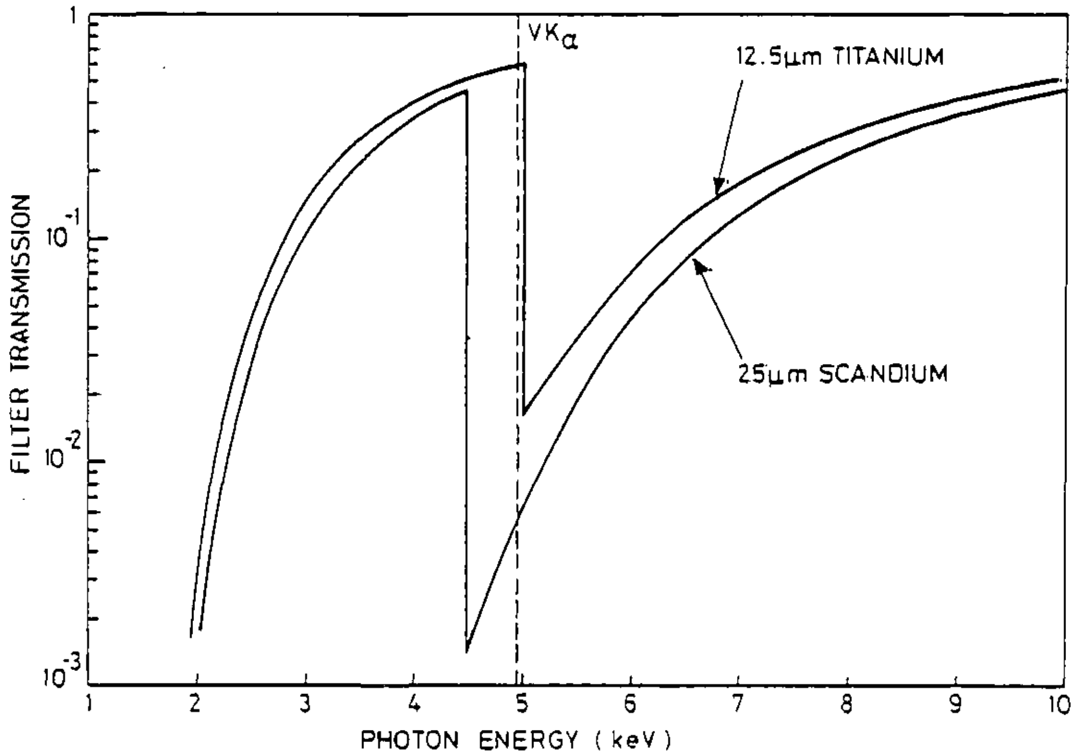

Fig. 2.2. TRANSMISSION OF TITANIUM AND SCANDIUM FILTERS

camera. The focal spot was imaged onto the photo-cathode of the camera using a 0.8 mm wide Tungsten slit, positioned perpendicular to the time-resolving slit over the cathode. A magnification of 2.7 to 3 times was used. The cathode consisted of a substrate of 25 μm Beryllium coated with 20 μm of low density CsI foam. The CsI foam had an areal density equivalent to 1 μm of solid CsI producing a peak in sensitivity at an X-ray wavelength of 2.4 Å. When used with filtering of 12.5 μm Ti plus 125 μm Be, the camera had a region of sensitivity between X-ray energies of 4 and 5 keV, bracketing Vanadium Kα. Fig. 2.3 illustrates the experimental set-up with the laser incident in the z direction polarised in the y direction.

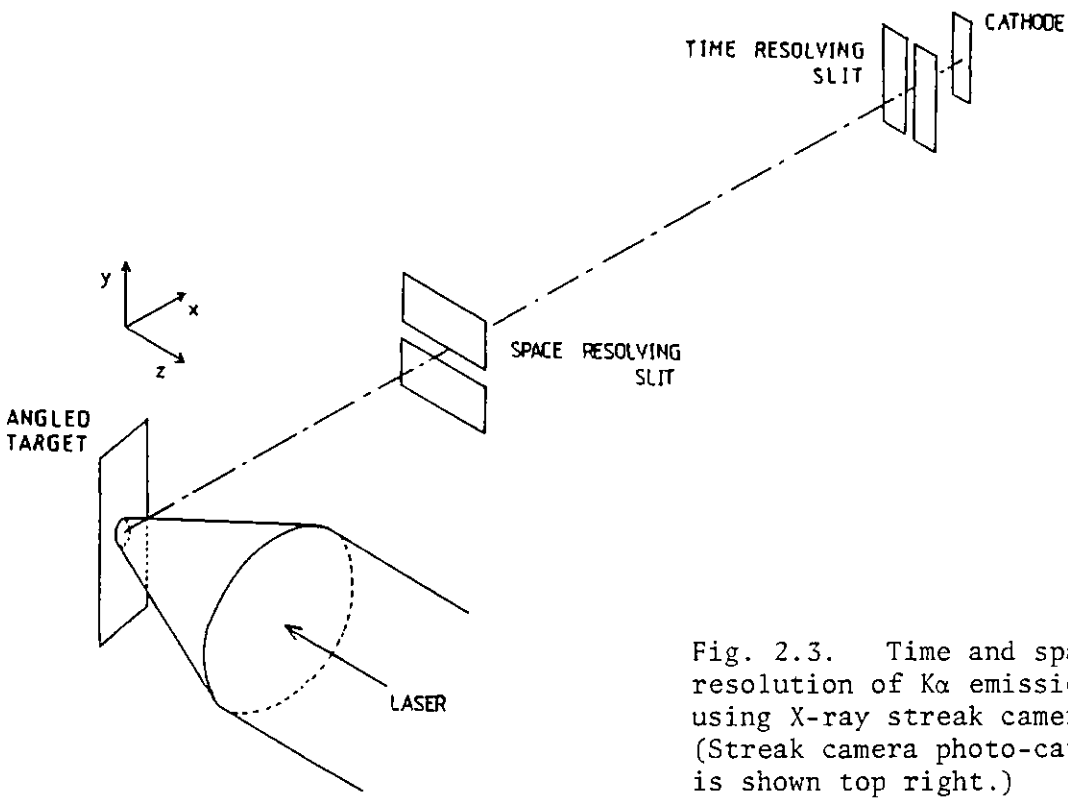

Fig. 2.3. Time and space resolution of Kα emission using X-ray streak camera. (Streak camera photo-cathode is shown top right.)

The Tungsten slit space resolved in the y direction up the target, spatially integrating in the z direction over a foreshortened target.

2.3 Long Pulse Experiment

A 50 μm diameter focal spot was illuminated with 50J of $\lambda = 1.054$ μm radiation in a 1.3 nanosecond pulse. The incident intensity of $2\ 10^{15}$ W cm^{-2} would be expected to produce hot electrons with a temperature $T_H \simeq 12$ keV[2.05]. Large aperture X-ray pinhole pictures clearly

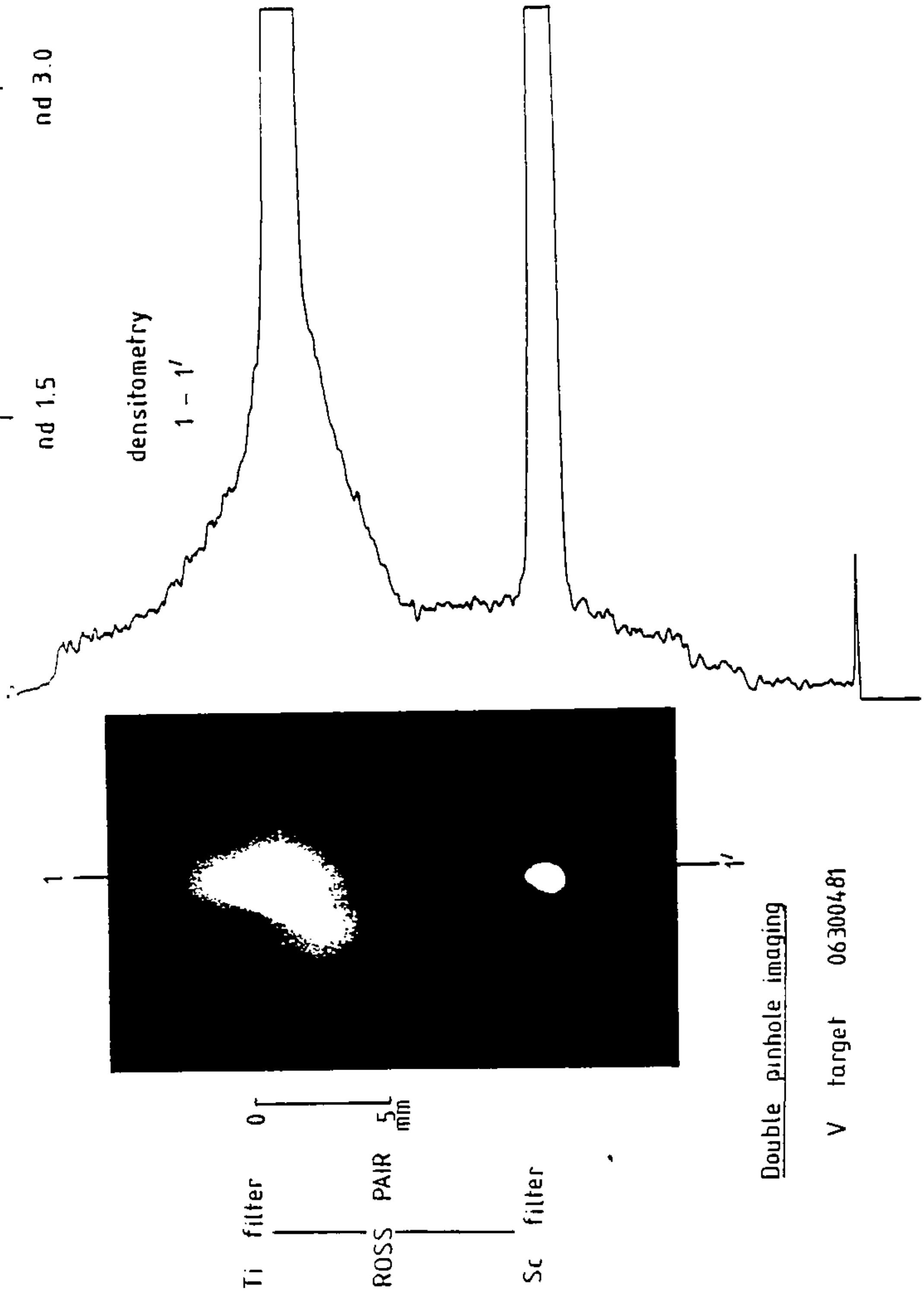

Fig. 2.4. Differentially-filtered time-integrated X-ray pinhole images of a Vanadium target irradiated with a 1.3 nanosec pulse of 1.054 μm light.

show an X-ray emitting region several millimetres from the 50 μm focal spot. Fig. 2.4 shows differentially-filtered pinhole images of the same shot. The filters of 12.5 μm Ti and 25 μm Sc are as in Fig. 2.2. The Titanium-filtered image shows bright remote emission whilst the Scandium-filtered image shows very little emission outside the bright focal spot. The focal spot is below the resolution limit of the pinhole and so the bright central spot appears larger than 50 μm in the pinhole images shown.

Comparison of the two images in Fig. 2.4 leads to the conclusion that the emission away from the focal spot is due to Kα radiation. An interesting feature of Fig. 2.4 is the asymmetry of Kα production around the focal spot. If the Kα were being caused by radiation pumping, the emission would have circular symmetry about the focus. X-ray spectra from the focal region show that the emission there is dominated by the $1s^2\ {}^1S_0$ - $1s2p\ {}^1P_1$ transition of V XXII which is not energetic enough to produce K ionisation making photoionisation as a source of Kα unlikely. Shots using targets with a small plastic dot at the laser focus showed no reduction in Kα from the uncoated remote regions, as would be expected if radiation were significant.

The isolation of the remote emission as being due to Kα radiation produced by fast electron-induced ionisation allowed an estimate of the total energy deposited by fast electrons to be made. Previously fast electron energy deposition has been measured using X-ray spectrometers to record the absolute intensity of fast electron-produced Kα(2.12). If the energy of the electrons producing the K ionisation is significantly greater than the K ionisation threshold E_K then the ratio of fast electron-induced Kα to total energy deposited by fast electrons is almost constant. The differential filters on the pinholes, in isolating the Kα radiation in one of the images, allowed the remote fast electron deposition to be measured as 5% ± 1% of the incident energy. A time-integrating X-ray spectrometer recorded Kα from the focal spot and led to an estimate of the fractional deposition by fast electrons there of $\lesssim$ 0.3% of the incident energy(2.13). The low level of preheat energy going into the target under the focal spot is in agreement with previous experiments reported(2.07)-(2.11). However only in λ = 10.6 μm plane target experiments has sideways energy transport by fast electrons been observed(2.14)(2.15)(2.16) and then only semi-qualitatively. For example, Ebrahim et al. in reference 2.14 have measured the ion emission from the front and rear sides of disc targets irradiated with 10.6 μm (CO_2) laser pulses and have inferred large energy transport to the rear surface. These observations for λ = 1.054 μm light in 1.3 nanosecond pulses are the first quantitative measurements of sideways energy transport, they are also the first at this wavelength which are time resolved. Jaanimagi et al. in reference 2.15 report observing radial spreading of energy away from the focal spot with a velocity of 10^9 cm/s for 750 picosec pulses of λ = 10.6 μm light. For the 1.3 nsec pulse 1.054 μm experiment described here time resolution of the spreading of the region of Kα emission was achieved using the X-ray streak camera set up as described in section 2.2.3. A filter consisting of 12.5 μm of Titanium plus 125 μm of Beryllium was put over the 0.8 mm Tungsten space-resolving slit. The time-resolving slit was 1 mm wide giving 110 picoseconds time resolution at the streak speed of 110 picoseconds/mm used. A typical streak is shown in Fig. 2.5, where the Kα emission from a Vanadium target irradiated with 2.6 10^{15} W cm^{-2} is time resolved. The image of the focal spot has been moved to one side of the cathode, by adjusting the space-

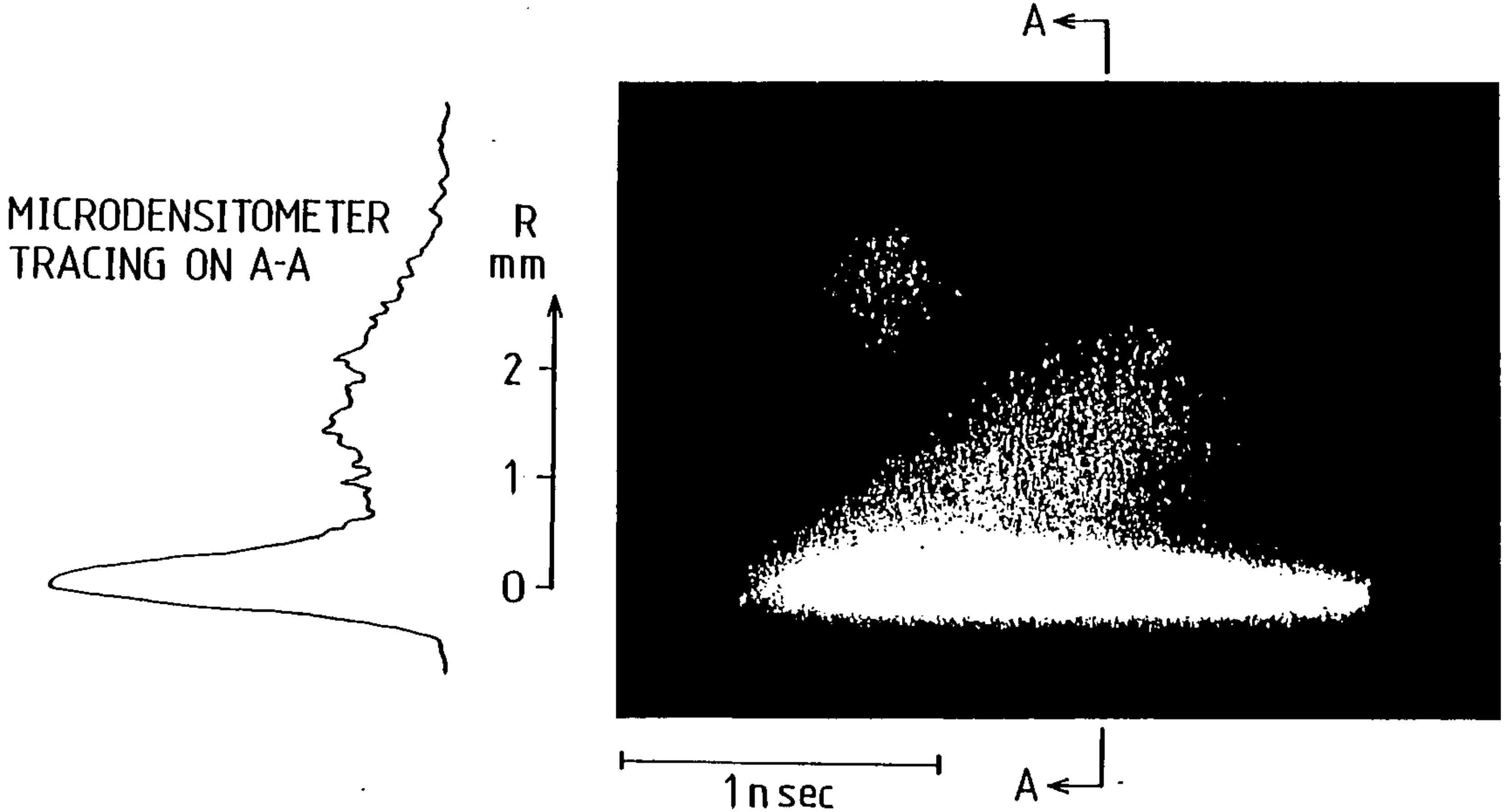

Fig. 2.5. Streaked Kα emission from a Vanadium target irradiated with 2.6 10^{15} W cm^{-2} in a 1.3 nsec pulse.

resolving slit position, so that only spreading on one side of the focal spot is seen. The spreading velocity of fast electron induced Kα is seen to be (2.3 ± 0.2) 10^8 cm/s, which is considerably lower than the velocity of 6.5 10^9 cm/s associated with fast electrons of $T_H \sim 12$ keV. Fast electrons are limited in their motion by space charge effects at the edge of the plasma. Therefore they are limited in how fast they can progress across the target surface by the expansion velocity of the fast ion cloud. A velocity of 2 10^8 cm/s is of the right order to be a component of velocity of ions accelerated by fast electron reflection at the plasma boundary[2.17].

The Kα emission in Fig. 2.5 is seen to peak at the edge of the emitting region as demonstrated by the microdensitometer trace AA. The concentration of fast electron energy deposition at the edge of the emitting region is consistent with the idea of electrons being constrained within the limit of fast ion motion. The electric field at the edge of the plasma will direct electrons inwards towards the target surface [2.18].

2.4 Short Pulse Experiment

An 80 picosecond pulse of 1.054 μm light was used to repeat the previous experiment but at an irradiance in the range 2.6 10^{15} W cm^{-2} up to 1.8 10^{16} W cm^{-2}. A 50 μm to 200 μm focal spot was used. Fig. 2.6 shows a pair of X-ray pinhole pictures taken with 400 μm diameter pinholes. The picture is taken from a direction perpendicular to the laser with the target angled 6° towards the camera to produce a foreshortened image of the target. The images show a bright focal spot with ablation plasma streaming off it and a bright region of Kα emission around the focus. The filters used were 125 μm Be and 12.5

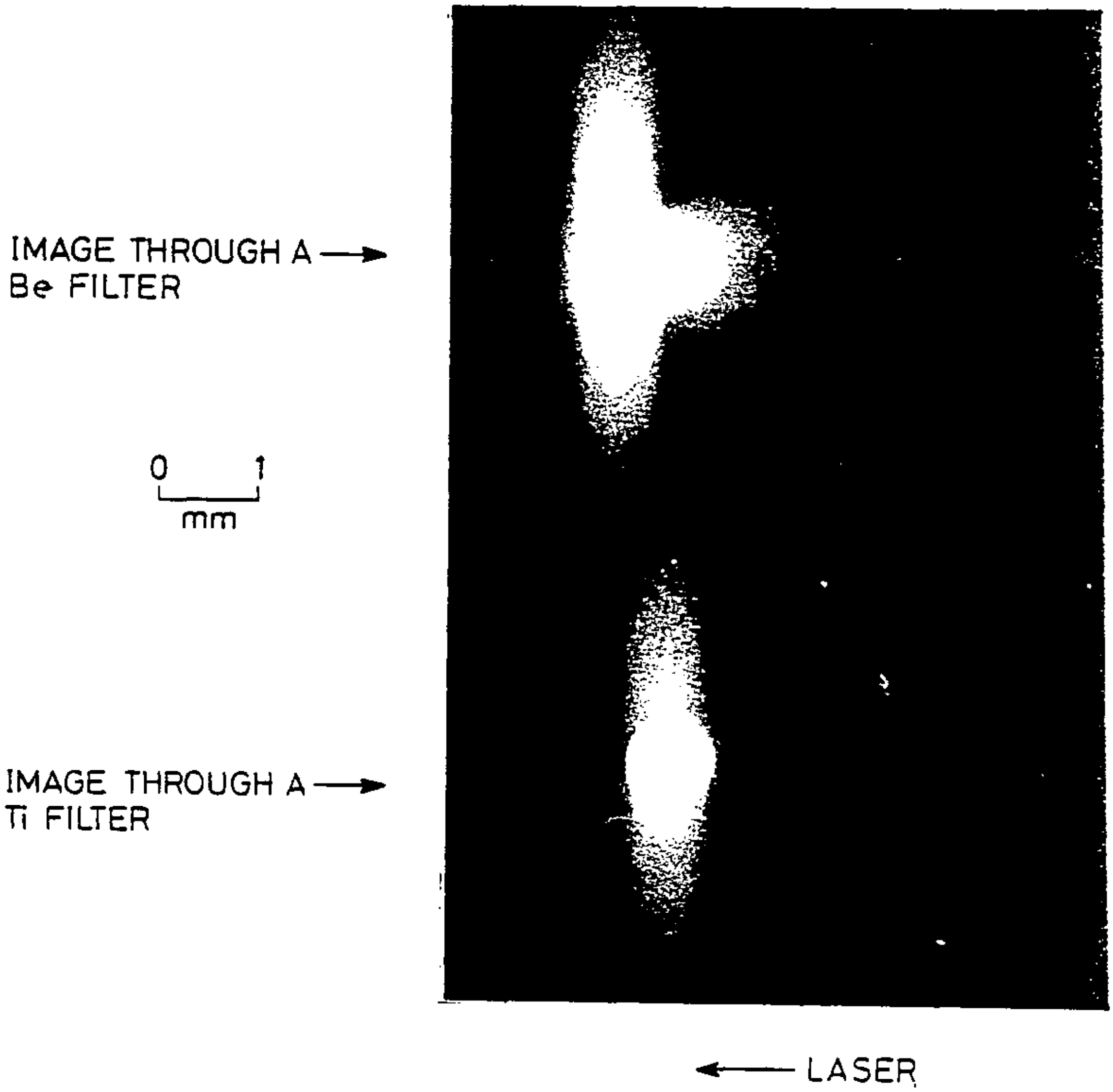

Fig. 2.6. PAIR IMAGES OF A V STRIP TARGET (09160681)

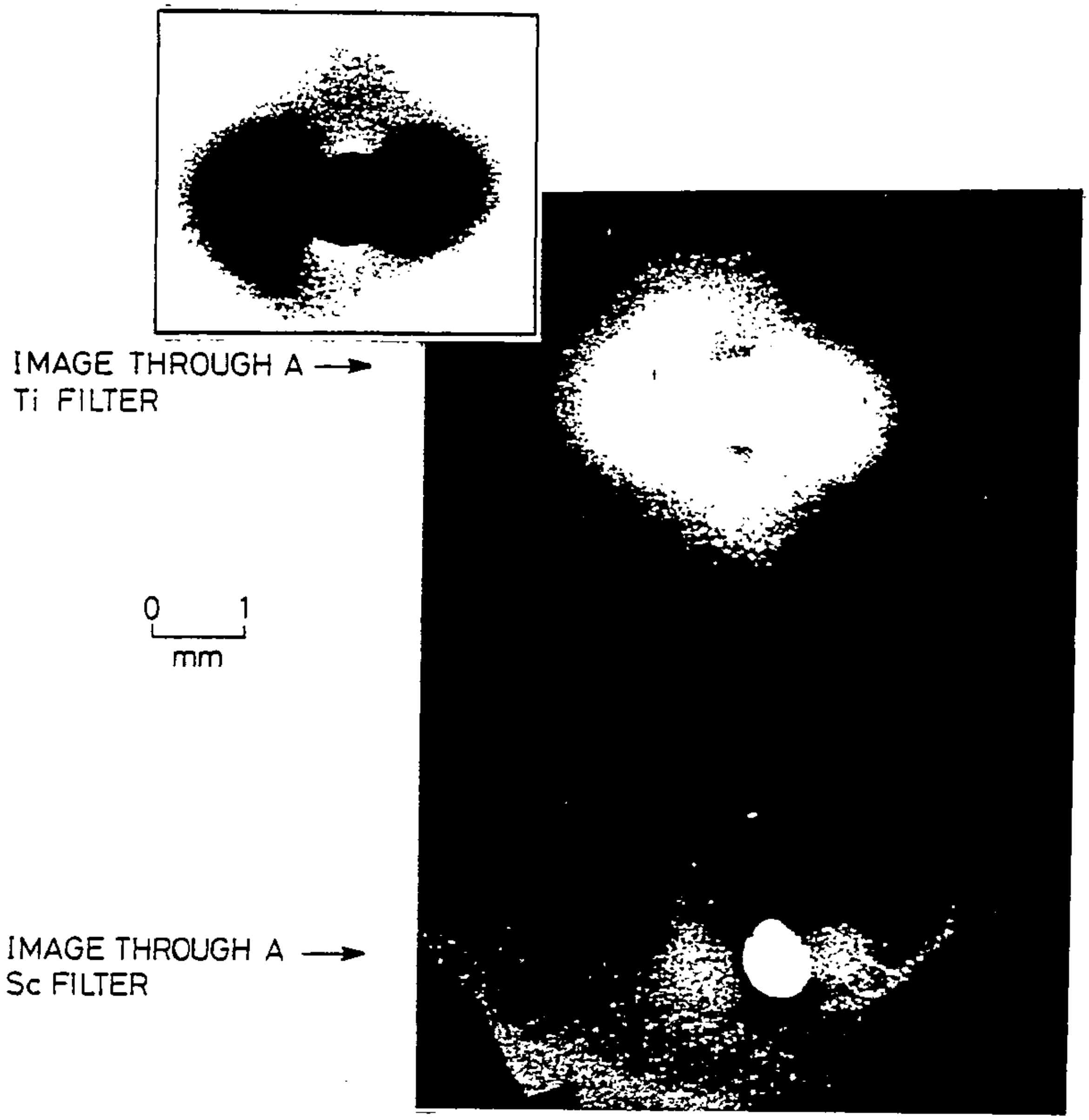

Fig. 2.7. ROSS PAIR IMAGES OF A LARGE V TARGET
(1118 0681)

μm Ti.

Figure 2.7 gives a view from the front of the target in a similar shot. The inset negative shows the structure of the Kα emission in the Titanium filtered picture.

The justifications for neglecting radiation-pumped Kα are as in the previous section. Asymmetry in the Kα was observed (as in Fig. 2.7) and also the placing of small plastic dots at the focus produced no reduction in Kα. An interesting feature of Fig. 2.7 is the brighter emission at the points where the incident light would be p polarised with respect to a spherically expanding critical density surface. It is at these points where fast electron production would be expected to peak.

The fractional energy deposition was measured as described in the previous experiment. The deposition under the focus was 7 ± 1% of incident whilst the remote deposition varied from 1 ± 0.5% (at 2.6 10^{15} W cm^{-2}) up to 10 ± 2% (at 1.8 10^{16} W cm^{-2}) over the intensity range used(2.13).

The Kα emission was time resolved as described for the previous experiment. The time-resolving slit over the cathode was ½ mm wide, giving 23 picoseconds time resolution at the streak speed of the 46 picoseconds/mm used. Fig. 2.8 shows a typical streak obtained. The Kα emitting region is seen to expand away from the focus at a speed of (2.2±.4)10^9 cm/s. The particular shot shown was of a target irradiated with an intensity of 3.7 10^{15} W cm^{-2}, which would produce a hot electron temperature of $T_H \simeq 14$ keV.(2.05). A velocity of 2.2 10^9 cm/s is reasonable for 14 keV electrons moving with a component of their velocity in the radial direction away from the focus. However the velocity measured is inconsistent with the velocity of expansion of

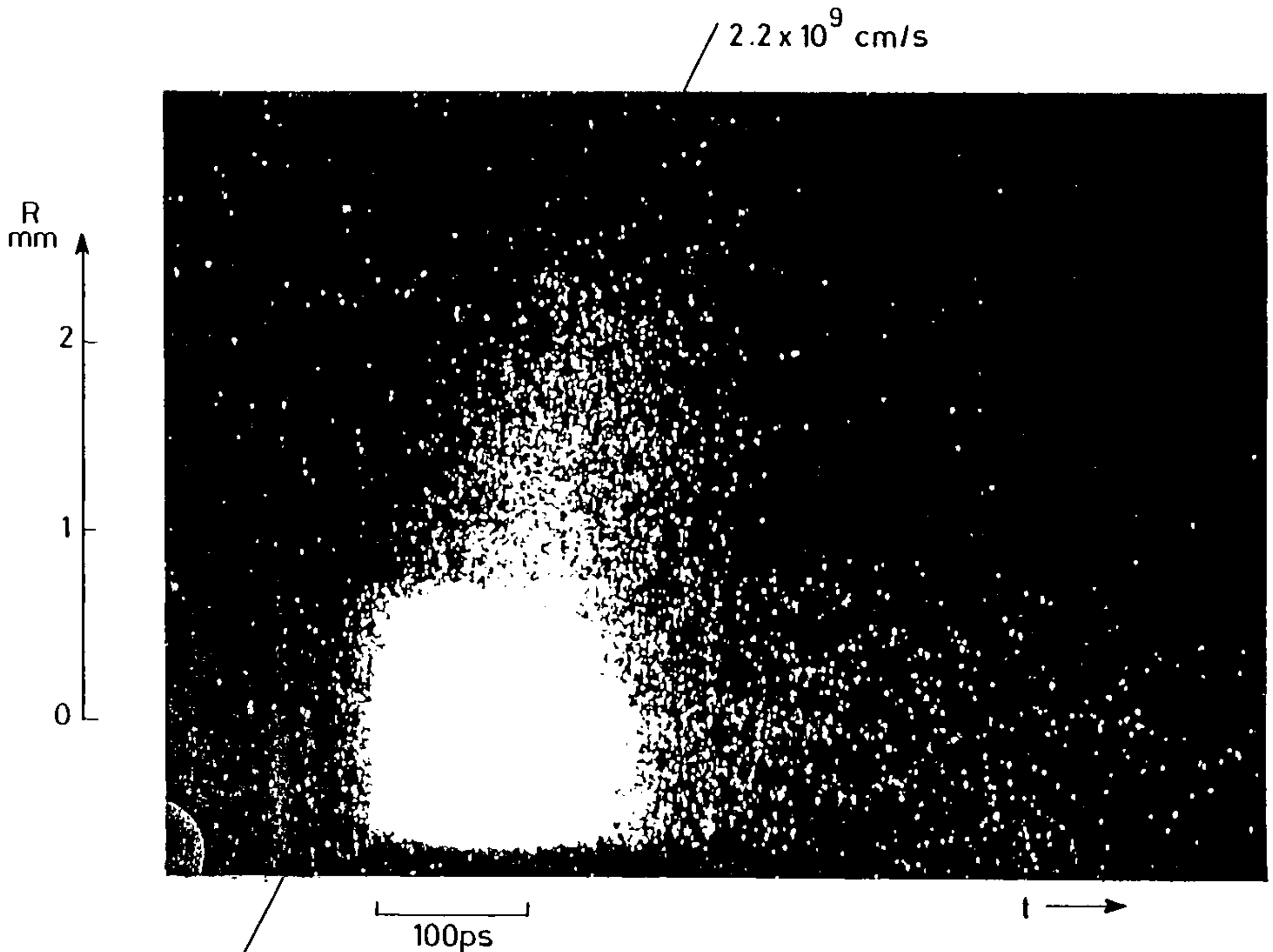

Fig. 2.8. X-RAY STREAK OF A V TARGET THROUGH A 12.5μm Ti FILTER (15180681)

the fast ion cloud. The electrons must move through a neutral plasma and a possible mechanism for the production of the plasma required is radiation from the focal spot ionising a thin surface layer on the target. Alternatively a small number of very fast electrons may provide the necessary ionisation. Gross irreproducible asymmetries in $K\alpha$ emission were observed on some of the shots and this could be due to low Z surface impurities such as vacuum pump oil or oxides providing a more readily ionised layer than the underlying metal. The asymmetries could also be due to the presence of very strong electric or magnetic fields in the region of the focal spot[2.18] channelling electrons towards particular areas.

2.5 Discussion

The reduction in preheat energy under the focal spot for long pulse irradiation is of possible advantage to the implosion of spherical targets to produce high densities. However an experiment must be performed in spherical geometry in order to determine where the large amount of energy, flowing sideways on the plane targets, actually goes on a microballoon. If the energy is absorbed on the balloon's surface where it can contribute to material ablation then long pulse $\lambda = 1.054$ μm irradiation may be useful as a very uniform method of illuminating fusion targets. Irregularities in the illumination due to having a finite number of laser beams (e.g. currently six at Rutherford Appleton Laboratory) may be quickly smoothed by the lateral flow of fast electron energy. Although some lateral flow is present in the short pulse case the preheat of the target fuel could make the achievement of high compression densities impossible with such short pulses.

2.6 Conclusion

Lateral energy transport by fast electrons in plane geometry has been observed and quantified for the first time for $\lambda = 1.054\ \mu m$ high intensity laser pulses. The flow of energy sideways has been time resolved for the first time at the potentially useful wavelength of $1.054\ \mu m$. A different velocity of spreading was observed in the two different pulse length regimes studied. For long pulse (1.3 nano-second) irradiation the flow is dominated by the expansion velocity of the fast ion cloud. For short pulses (80 picoseconds) the fast electrons are allowed to spread at a fraction of their velocity through a surface plasma formed by radiation from the intense focal spot, or the action of a few very energetic electrons. Investigation of the phenomenon of energy spreading is of interest to laser fusion as it affects the uniformity of energy deposition in laser fusion targets. Furthermore, spreading may complicate the interpretation of model experiments done in planar geometry which may become two-dimensional in nature in the presence of strong lateral energy transport.

CHAPTER 3

VON HAMOS CURVED CRYSTAL X-RAY SPECTROMETER

3.0 Abstract

A focusing crystal X-ray spectrometer has been developed and used as an attachment to an X-ray streak camera. The device can be used to provide significant gain in spectral intensity or as a high dispersion instrument. The spectral resolution is limited by imperfections in the crystal and not by the plasma source size, as in previous instruments.

3.1 Introduction

X-ray spectra emitted in the 1 - 5 keV region from laser plasmas have proved themselves a valuable source of diagnostic information[3.01]. Spectra are routinely recorded using flat Bragg diffracting crystals to produce the dispersion. Time-integrated spectra are obtained using minispectrometers[3.02] placed so that the entrance slit is within 6 mm of the plasma and the total separation of plasma and film is typically 6 cm. These spectrometers are thus very sensitive but their spectral resolution is limited by the plasma source size.

Time-resolved X-ray spectroscopy has been performed using the same flat crystals to diffract X-rays onto the photo-cathode of an X-ray streak camera[3.03]. Constraints due to the size of the streak camera and target chamber diagnostic space mean that the separation of plasma and cathode cannot be less than $\sim$ 20 cm. The brightness of a spectral line, if expressed in photons/cm^2 on the detector, varies as the square

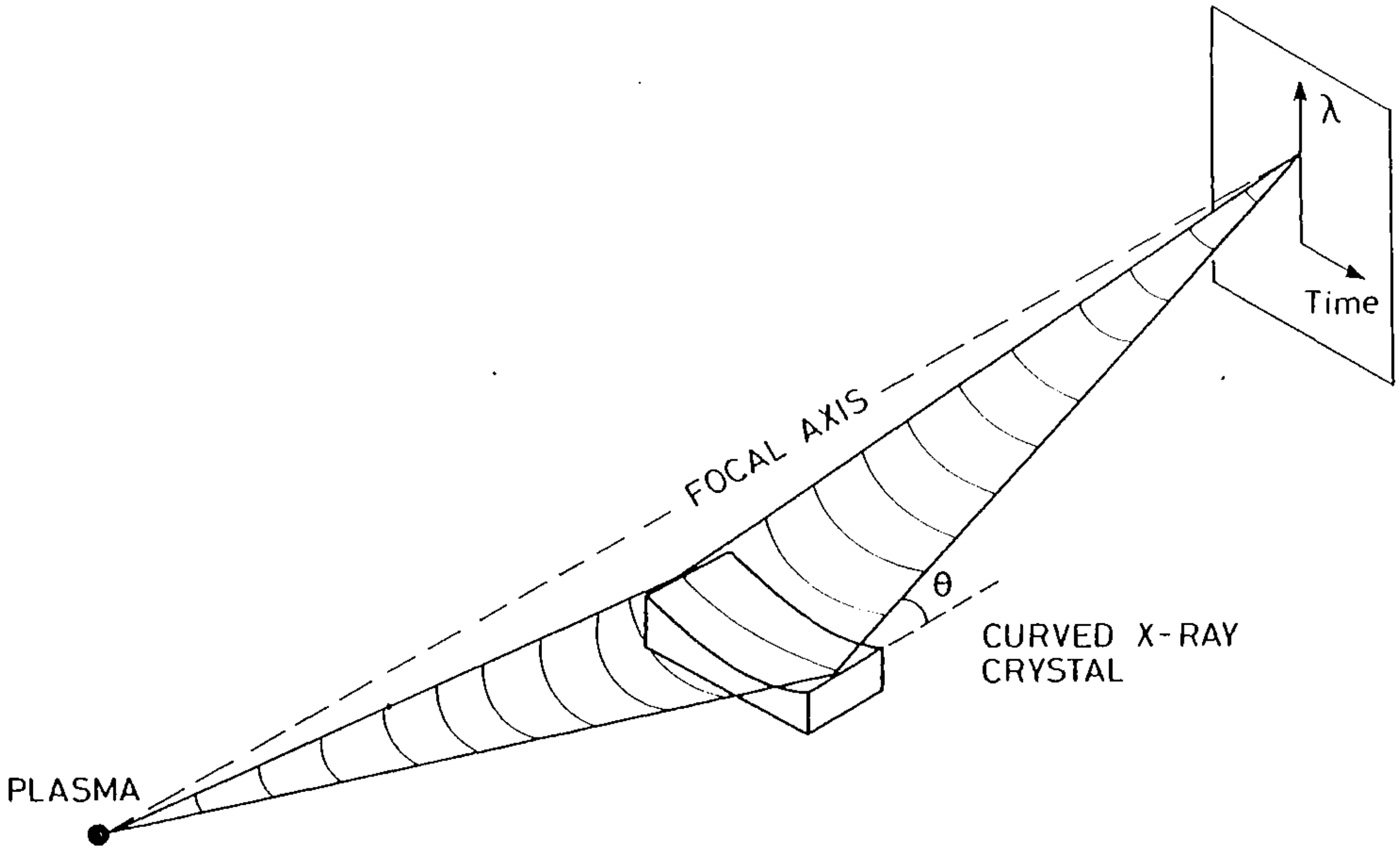

Fig. 3.1. Geometry of the spectrometer. The X-rays from the plasma are focused on to the streak camera photo-cathode on the right.

of the distance to the source, therefore using a streak camera means a drop in sensitivity. Dispersing the spectrum in time by streaking it will also reduce the brightness of the lines.

A method of increasing the sensitivity of time-resolved spectroscopy is suggested when it is realised that most of the X-rays reflected off the flat crystal are not admitted through the time-resolving slit over the streak camera photo-cathode. Instead, only a narrow slice through each spectral line is allowed through the slit in order to obtain time resolution. If the spectrum is compressed, or focused, along the spectral lines, all of the X-rays reflected by the crystal can be incident on the photo-cathode without any loss of time resolution. The focusing is achieved using a concave curved crystal arranged in the geometry shown in Fig. 3.1.

The crystal is a section of a cylinder whose axis connects the plasma to the centre of the streak camera photo-cathode. X-rays are collected over the surface of the crystal and focused back onto the axis of the cylinder. The condition for focusing is simply:

$$r_c = \frac{\ell}{2} \tan \theta \qquad (3.01)$$

where r_c is the radius of the cylinder and ℓ is the separation of the cathode and plasma. The Bragg angle θ is given by:

$$\theta = \sin^{-1} \frac{n\lambda}{2d} \qquad (3.02)$$

The crystal only focuses at one wavelength on the cathode, at the point where the cylinder axis intersects the cathode. Wavelengths dispersed either side of the focus will produce spectral lines of finite length due to off-axis aberrations. However the aberration for wavelengths off focus can be kept less than 1 mm over the spectral region of interest. The aberration sets the time resolution of the streak camera and replaces a time-resolving slit in performing this function.

The quality of the focus at right angles to the spectral direction is set by the quality of the crystal curvature and the source size. The crystal spatially resolves along the spectral lines[3.04] in a manner analogous to a concave mirror at unit magnification. The length of the spectral line at focus, in the limit of a perfectly bent crystal, is therefore the source size. Aberrations due to poor focusing and the crystal curvature quality also limit the minimum size of the spectral lines.

The spectrometer is a Von Hamos[3.05] type but used with the detector (streak camera photo-cathode in this case) perpendicular to the focal axis. Using the spectrometer in the conventional Von Hamos orientation, with the detector along the focal axis, would make the system physically impractical. A Von Hamos spectrometer, using X-ray film as the detector, was built in the conventional orientation. However, to use this orientation with an X-ray streak camera would require source to photo-cathode distances in excess of 70 cm. The dispersion of any useful crystal would be so large at these distances that the spectral range of the cathode would be minimal.

3.2 Theory of the Spectrometer

A short calculation of the focusing property of a curved crystal will be made. This calculation will be done for the more general case of the source off the focal axis, corresponding to a misalignment of the spectrometer. The intensity distribution on a photo-cathode perpendicular to the focal axis will be calculated. The first calculation is similar to that done by Yaakobi and Bhagavatula in reference 3.04 but is used to derive the intensity distribution perpendicular to the focal axis. Several important characteristics of the spectrometer will then be derived.

3.2.1 Calculation of image due to source off axis

Consider a curved crystal arranged in the geometry of Fig. 3.1. Cartesian axes are drawn in Fig. 3.2, with the x axis marking the centre of the cylinder. The (y,z) plane contains the X-ray source at S, a distance h along the y axis, with coordinates (0,h,0). The photocathode is defined by the plane $x = \ell$. A ray is reflected from the crystal at a point R, at the Bragg angle θ to the crystal planes (defined by a tangent to the crystal at that point). The point R is described by x_r (the x coordinate) and ψ, the angle between the line OR and the $z = 0$ plane.

Fig. 3.3 shows a cut perpendicular to the focal axis, through the reflection point R. The point A is the projection of S on the cut plane. The angle SRO is the complement of the Bragg angle. The angle RSB is the Bragg angle θ, where B is located by dropping a perpendicular from A onto OR. The triangle RSB is then right-angled so:

$$\tan\theta = \frac{RB}{BS} \tag{3.03}$$

From Fig. 3.3

$$RB = r_c + h\cos\psi \tag{3.04}$$

Looking at the right-angled triangle SBA

$$(BS)^2 = (SA)^2 + (AB)^2$$

$$\therefore \quad (BS)^2 = x_r^2 + h^2\sin^2\psi \tag{3.05}$$

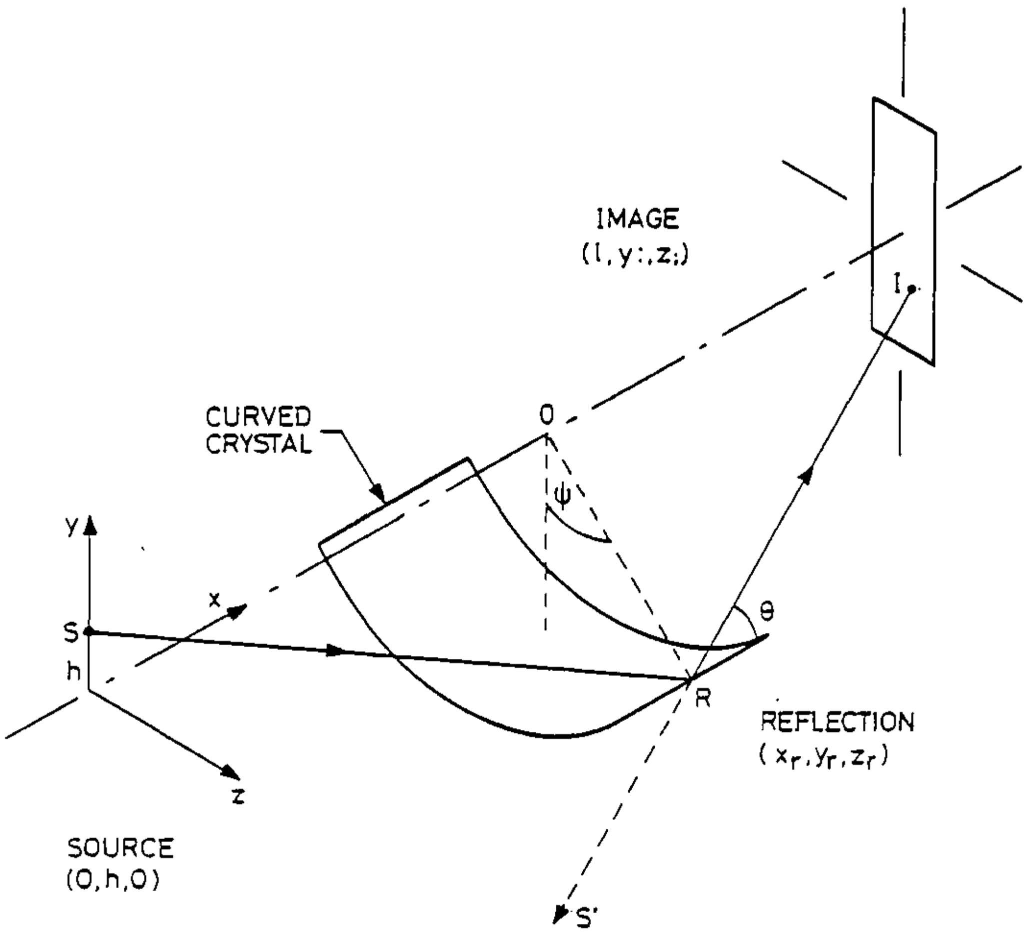

Fig. 3.2. The coordinate system.

Using equations (3.03), (3.04) and (3.05), we obtain:

$$x_r^2 = \frac{(r_c + h \cos \psi)^2}{\tan^2 \theta} - h^2 \sin^2 \psi \qquad (3.06)$$

Note that:

$$y_r = - r_c \cos \psi \qquad (3.07)$$

$$z_r = r_c \sin \psi \qquad (3.08)$$

The position of S', the projection of the reflected ray back to the x = 0 plane, is now calculated. From Fig. 3.3 the position of A' gives:

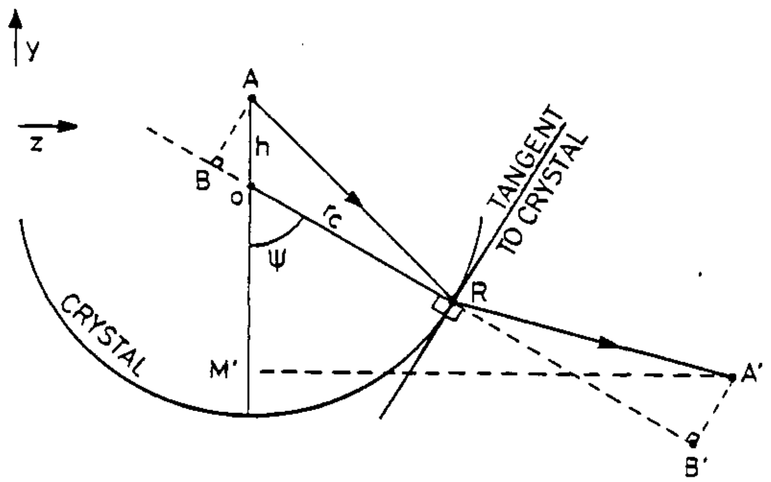

Fig. 3.3. Cut showing the plane perpendicular to the focal axis, through the reflection point R. The point A is the projection of the source point S on this plane.

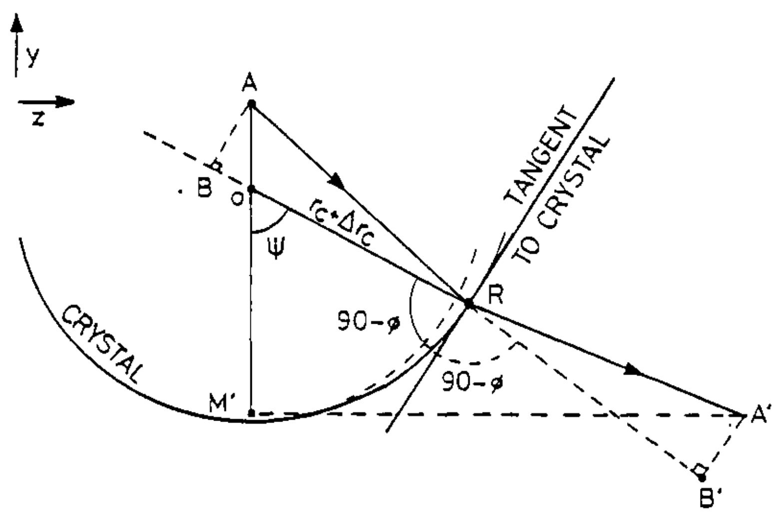

Fig. 3.4. Cut as above but the crystal is deformed such that the surface is not cylindrical (as seen from the deviation from the dashed circle near R). The radius at point R is $r_c + \Delta r_c$, the crystal planes are at an angle $90^o - \phi$ to the radius vector OR.

$$y_{s'} = h - 2 \cos \psi \, (r_c + h \cos \psi) \tag{3.09}$$

$$z_{s'} = 2 \sin \psi \, (r_c + h \cos \psi) \tag{3.10}$$

The equation defining the image coordinates (x_i, y_i, z_i) is:

$$\frac{x_i - x_{s'}}{x_r - x_{s'}} = \frac{y_i - y_{s'}}{y_r - y_{s'}} = \frac{z_i - z_{s'}}{z_r - z_{s'}} \tag{3.11}$$

Noting that $x_i = \ell$ and that $x_{s'} = 0$ and expanding to second order in $\frac{h}{r_c}$ we obtain:

$$y_i = - h - 2r_c \cos \psi \, (1 - T) + 2h \sin^2 \psi \, (1 - T) + \frac{h^2}{r_c} T \cos \psi \sin^2 \psi \, (\tan^2 \theta + 2) \tag{3.12}$$

and,

$$z_i = 2r_c \sin \psi \, (1 - T) + h \sin 2\psi \, (1 - T) - \frac{h^2}{r_c} T \sin \psi \, (\tan^2 \theta \sin^2 \psi - 2 \cos^2 \psi) \tag{3.13}$$

where

$$T = \frac{\ell}{2r_c} \tan \theta \tag{3.14}$$

Taking the particular case for $h = 0$, (3.12) and (3,13) become:

$$y_i = - 2r_c \cos \psi \, (1 - T) \tag{3.15}$$

and,

$$z_i = 2r_c \sin \psi \, (1 - T) \tag{3.16}$$

These are the equations of a circle of radius $2r_c(1 - T)$ parameterised by ψ. The spectral lines produced by the spectrometer are defined by T = constant and are thus circular about the focus, defined by $T = 1$. In the limit when the maximum value of ψ, (denoted

ψ_0) is small, the curvature of the spectral lines is negligible.

3.2.2 Dispersion of spectrometer

Taking equation (3.15) and differentiating with respect to λ we get:

$$\frac{dy}{d\lambda} = \frac{\ell}{2d} \frac{\cos \psi}{\cos^3 \theta} \tag{3.17}$$

as the wavelength dispersion up the photo-cathode.

3.2.3 Off-axis aberration

Equation (3.16) shows that the spectral lines have a finite length perpendicular to the direction of dispersion. For a crystal with sector angle equal to $2\psi_0$ the length Δz of a spectral line is

$$\Delta z = 4r_c \sin \psi_0 \ (1 - T) \tag{3.18}$$

Dividing by the y position up the cathode (3.15) we get:

$$\Delta z = 2 \tan \psi_0 \ . \ y \tag{3.19}$$

where in this approximation, for h = 0, the focus is at y = 0.

Typically the streak camera photo-cathode has a useful region 20 mm in height corresponding to y = ± 10 mm. Therefore, to keep Δz less than one mm over the whole useful region, a crystal with sector angle $2\psi_0 \lesssim 0.1$ radians must be used. However Δz will be smaller than one mm over most of this region.

3.2.4 Gain over flat crystal spectrometer

The curved crystal spectrometer is compared with a flat crystal spectrometer of the same diffracting material arranged in the same geometry. The flat crystal instrument has a time-resolving slit of width Δz_f.

For an increment of Bragg angle $\delta\theta$ the curved crystal subtends a solid angle $\delta\Omega_c$ at the plasma.

$$\delta\Omega_c = 2\psi_0 \sin\theta \, \delta\theta \tag{3.20}$$

The flat crystal instrument subtends a solid angle of $\delta\Omega_f$ at the time-resolving slit over the photo-cathode

$$\delta\Omega_f = \frac{\Delta z_f \sin\theta}{2r_c} \, \delta\theta \tag{3.21}$$

where r_c is the distance of the flat crystal from the axis connecting the plasma to the centre of the photo-cathode. In the curved crystal case r_c is also the radius of curvature of the crystal.

The ratio of the sensitivities of the two instruments is simply the ratio of the two solid angles seen by the streak camera, for the increment of Bragg angle $\delta\theta$.

$$\frac{I_c}{I_f} = \frac{\delta\Omega_c}{\delta\Omega_f} = \frac{4r_c}{\Delta z_f} \psi_0 \tag{3.22}$$

If the time-resolving slit on the flat crystal instrument is set equal to the off-axis aberration Δz of the curved crystal (equation (3.19)), we get:

$$\frac{I_c}{I_f} = \frac{2r_c \psi_0}{y \tan\psi_0} \tag{3.23}$$

For the small values of ψ_0 being considered, $\psi_0 \simeq \tan\psi_0$, so

$$\frac{I_c}{I_f} = \frac{2r_c}{y} \tag{3.24}$$

This equation implies that if the time resolution of the two spectrometers is the same then the curved crystal device will be more sensitive by at least a factor of

$$\frac{I_c}{I_f} > \frac{4r_c}{C} \tag{3.25}$$

where C is the length of the useful region of the cathode.

3.2.5 Imaging property of curved crystal

Equation (3.12) was derived for a source displaced a distance h up the y axis. At the focus, T = 1, so equation (3.12) can be re-written as

$$y_i = - y_s + \frac{y_s^2}{r_c} \cos\psi \sin^2\psi (\tan^2\theta + 2) \tag{3.26}$$

where y_s is the y coordinate of the source. Equations (3.12) and (3.13) can be transformed by rotation into the equations for a source displaced along the z axis in the x = 0 plane. They become:

$$\begin{aligned} y_i = & - 2r_c \cos\psi (1 - T) + z_s \sin 2\psi (1 - T) \\ & + \frac{z_s^2}{r_c} T \cos\psi (\tan^2\theta \cos^2\psi - 2 \sin^2\psi) \end{aligned} \tag{3.27}$$

and,

$$\begin{aligned} z_i = & - z_s + 2r_c \sin\psi (1 - T) + 2z_s \cos^2\psi (1 - T) \\ & - \frac{z_s^2}{r_c} T \sin\psi \cos^2\psi (\tan^2\theta + 2) \end{aligned} \tag{3.28}$$

Rewriting equation (3.28) for T = 1, we get,

$$z_i = - z_s - \frac{z_s^2}{r_c} \sin\psi \cos^2\psi (\tan^2\theta + 2) \tag{3.29}$$

For displacements small compared with r_c the crystal will image the source onto the cathode. Hence the minimum width of the spectrum at the focus is set by the source size, in the limit of a perfect crystal. The spectral resolution is also set by the source size in the same limit of a perfectly-curved crystal. However, at the large dispersions used, the spectral resolution limits set by the crystal curvature quality and the crystal rocking angle are more important.

The imaging property of the crystal makes alignment quite easy as any small displacement of the source from the focal axis will not affect the focusing of the spectrum.

3.2.6 Spectral resolution

For wavelengths away from the focus the limit set on the spectral resolution by the curvature of the spectral lines is from equations (3.15) and (3.17)

$$\frac{\Delta\lambda}{\lambda} \simeq \left[\frac{\lambda - \lambda_0}{\lambda}\right] (1 - \cos \psi_0) \tag{3.30}$$

where λ_0 is the wavelength at the focus (T = 1).

3.2.6.1 Crystal curvature quality. Fig. 3.4 shows a cross-section through a crystal which has a defect in curvature. The defect is parameterised by a local variation $\Delta r_c(\psi)$ in radius plus a small angle $\phi(\psi)$ between the normal to the crystal planes and the radius vector at ψ. The defect is considered to be constant in the x direction (into the page), non-uniformities in this direction will be considered in the next section.

The notation in Fig. 3.4 is that of Fig. 3.3. If the y co-ordinate of the image point, due to the ray shown, is calculated for the case h = 0, we get

$$y_i = -2r_c \cos(\psi - \phi)(1 - T) + 2r_c T \sin\phi \sin\psi - 2\Delta r_c \cos(\psi - \phi) \qquad (3.31)$$

If the deviation Δy from the image point for a perfect crystal is calculated and used to find the wavelength spread, we get an expression for the spectral resolution as:

$$\frac{\Delta\lambda}{\lambda} \simeq \frac{\cos^2\theta}{T}\left[\sin\phi \tan\psi\,(1 - 2T) + \frac{\Delta r_c}{r_c}\right] \qquad (3.32)$$

For monotonic variations in the radius defect Δr_c with ψ, the two terms in the brackets will act in opposition. However for most large scale defects (for instance, an elliptical cross-section to the crystal) the resolution requirement can be expressed as:

$$\frac{\Delta\lambda}{\lambda} \simeq \cos^2\theta \;\frac{\Delta r_c}{r_c} \qquad (3.33)$$

In the crystals used so far $\Delta r_c \sim 0.1$ mm. The crystals were glued to brass mounts that had been machined to an accuracy of ~ 0.025 mm, the 0.1 mm thick glue layer introduced further error. The radii of the crystals were 11 cm which for $\theta \sim 45^{\circ}$ leads to a spectral resolution of $\frac{\lambda}{\Delta\lambda} \sim 2000$.

3.2.6.2 Surface quality. Poor surface quality, on the crystal, will produce crystal planes which are not parallel to the x axis, but at an angle $\delta\theta$ to it. Fig. 3.5 shows a cut through the plane defined by ψ = 0 (i.e., the (x, y) plane). The defective plane is producing a Bragg reflection at angle θ a distance of Δx away from the reflection point R. The subsequent displacement Δy of the image point away from I is:

$$\Delta y = r_c \left\{ \frac{2 \tan^+}{\tan \theta} - 1 - \frac{\tan^+}{\tan^-} \right\} - y_i \left\{ \frac{\tan^+}{\tan \theta} - 1 \right\} \qquad (3.34)$$

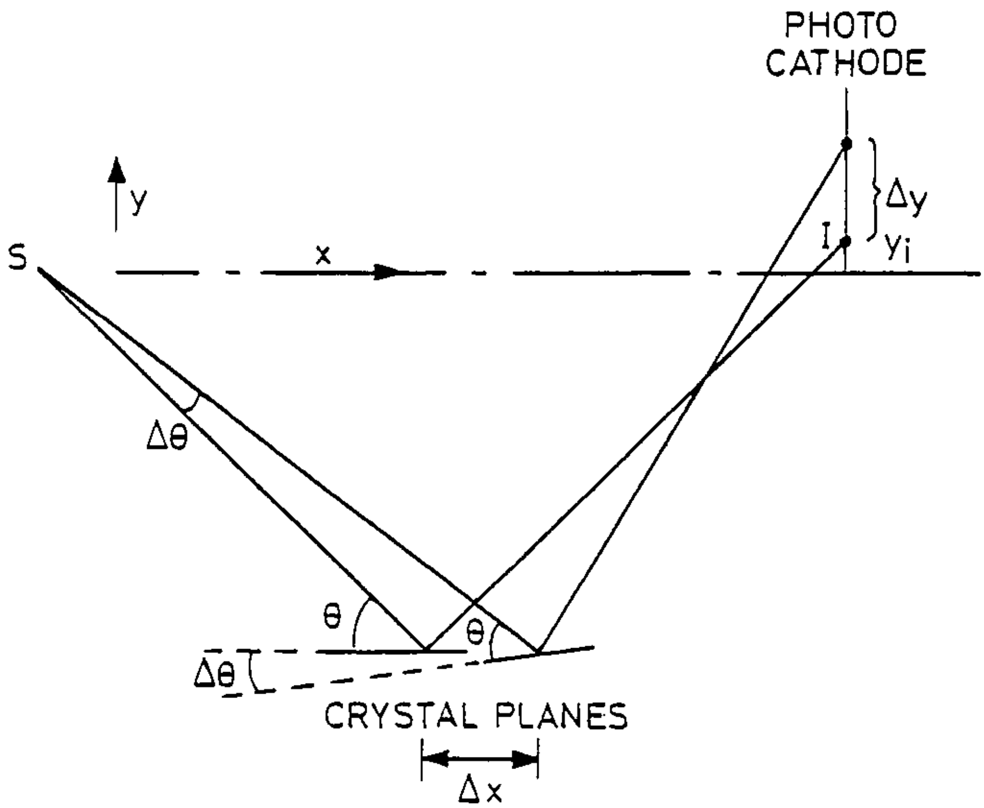

Fig. 3.5. Cut through the $\psi = 0$ plane, (x,y) plane, for a crystal with non-parallel crystal planes a distance Δx apart. The two planes produce image points a distance Δy apart on the photo-cathode.

where $\tan^+ = \tan(\theta + \delta\theta)$ and $\tan^- = \tan(\theta - \delta\theta)$. Expanding to second order in δθ we get:

$$\Delta y = \frac{y_i \delta\theta - \ell\, \delta\theta^2}{\tan \theta \cos^2 \theta} \qquad (3.35)$$

which imposes a limit on the spectral resolution of

$$\frac{\Delta\lambda}{\lambda} \simeq \frac{\frac{y_i}{\ell}\,\delta\theta - \delta\theta^2}{\tan^2\theta} \tag{3.36}$$

Equation (3.36) shows that for wavelengths near the focus ($y_i = 0$) the spectral resolution is second order in the angle $\delta\theta$. This property of the crystal is a consequence of the source and detector being equidistant from the reflection point. The property can be exploited by using a mosaic crystal which has several reflecting planes separated by small angles $\delta\theta$[3.04]. Usually a mosaic crystal provides better reflectivity because the rocking angle is larger than that of a perfect crystal. The larger rocking angle means poor spectral resolution. However in this geometry a mosaic crystal will provide greater reflectivity without significant decrease in spectral resolution, due to the separate planes producing spectra that are almost superposed to second order in $\delta\theta$. (Equation 3.36).

Equations (3.30), (3.33) and (3.36) all impose limits on the spectral resolution. A further restriction on resolution is the limit set by the source diameter D.

$$\frac{\Delta\lambda}{\lambda} = \frac{D}{2r_c}\cos^2\theta \tag{3.37}$$

Also, the crystal resolution is limited by the rocking angle, β, of the crystal. For an 11 cm radius of curvature PET crystal ($2d = 8.74$ Å), with $\psi_0 = 0.1$ radians set up for 6 Å X-rays at $\ell = 23.3$ cm, the spectral resolution limits are summarised in Table I.

Fig. 4.5 in Chapter 4 shows a streaked spectrum obtained with the 11 cm PET crystal. The microdensitometer tracing of the dielectronic satellites of the Lyα of Silicon indicates spectral resolution of $\sim$ 900.

TABLE I

Equation	Resolution Limit	Source of Limit	$\frac{\lambda}{\Delta\lambda}$
(3.30)	Curvature of lines	Curvature of lines at extremes of cathode, y_i = 10 mm	9000
(3.33)	Defects in curvature	$\frac{\Delta r_c}{r_c} \sim \frac{1}{1100}$ due to layer of glue	2200
(3.36)	Surface quality	$y_i \lesssim$ 10 mm $\delta\theta \sim$ 10 mrad From glue non-uniformity	3000
(3.37)	Source size	150 μm Diameter source	3000
$\frac{\tan\theta}{\beta}$	Rocking angle	120 arc sec rocking angle	1700
The expected resolution is $\frac{\lambda}{\Delta\lambda} \gtrsim 1100$			

3.3 Alignment

Alignment of the crystal was made relatively easy by the imaging properties of the crystal mentioned in section 3.2.5. The crystal has to be aligned so that the 'image' of the source falls on some part of the 4 mm wide cathode. The axis of the crystal has to be along a line joining the source to the cathode (the x axis as defined previously).

The two requirements mentioned above were satisfied quickly and easily by using a surrogate target consisting of a small light bulb filament. The filament is positioned using the same procedure as for a microballoon target. The crystal reflects the light from the filament to form a line focus on the cathode. The crystal is adjusted until the focus is in the centre of the cathode. The axis of the crystal is made parallel to the x axis by noting that the line image formed by the crystal is only slightly longer than the cathode. Therefore when the centre of the line is in the centre of the cathode the system is aligned. The crystal can now be moved up and down in the y direction without moving the centre of the image away from the centre of the cathode.

3.4 Results

As mentioned at the end of section 3.2, Chapter 4 contains spectra obtained with this device. The 11 cm curvature PET crystal was found to have a resolution of $\frac{\lambda}{\Delta\lambda} \sim 900$. The limit on this resolution is probably being set by the crystal rocking angle. The resolution limits set by machining and crystal assembly can be improved. The gain of this crystal over an equivalent flat crystal is, from equation (3.24), greater than 22 over 20 mm of the cathode.

Mica crystals (2d = 19.73 Å) have been bent to smaller radii than 11 cm. Owing to the cheapness of good quality mica it is very useful for making curved crystals. However, due to its large lattice spacing, in most applications very small ($\sim$ 4 cm) radii of curvature are required, giving little gain over flat crystals.

The chief use of curved crystals is to look at a narrow spectral range with good spectral resolution and high sensitivity. For example, resolving the dielectronic satellites of a Lyα line where spectral range does not have to be too large (e.g. Fig. 4.5) the high sensitivity has been found to be of use in time resolving the motion of the K absorption edge of a shock-heated material. The contrast of the edge increases with increased line density of attenuator but the signal level decreases. The use of a more sensitive curved crystal spectrometer enables better contrast to be obtained at the K edge.

3.5 Conclusions

A Von Hamos curved crystal spectrometer has been developed and used to image X-ray spectra from laser plasmas. The spectrometer can have significant gain in sensitivity over conventional flat crystal instruments, enabling higher dispersion spectra to be obtained. Spectrometers of this type are now being used routinely at Rutherford Appleton Laboratory in order to maximise the sensitivity of X-ray streaked spectroscopy.

CHAPTER 4

ABLATIVELY DRIVEN IMPLOSIONS OF MICROSHELLS

4.0 Abstract

Frequency-doubled Neodynium Glass laser light ($^{\lambda_0}/_2 = 0.53\ \mu m$) has been used for the first time to implode spherical microshells. Ablation pressures in excess of 20 Mbars, produced by the six-beam irradiation, were used to drive the ablative implosions. The compressed core material produced was of too low a temperature to permit density diagnosis by seed gas spectroscopy. The density of the glass shell, at the peak of the implosion, is estimated from X-ray pinhole images to be in the range 1 to 2 g cm^{-3}. Comparison with one-dimensional numerical simulations indicates that either preheat or asymmetry limit the compression. It is argued that decompression of the pusher, due to preheat, is the limiting factor on the final density achieved in the compression.

4.1 Introduction

Laser compression of matter to high densities has been attempted in the past using high intensity laser pulses of long wavelength. In this exploding pusher mode low densities are achieved. In the limit of low preheating of the target material, by fast electron and radiation transport processes, high pressure ($\sim 10^4$ Mbars), high density matter should be produced[4.01][4.02]. However in the long wavelength, high intensity experiments attempted, fast electrons deposit the absorbed energy uniformly throughout the target, preheating it. The fast electron range λ_h was large compared with the target shell thickness leading to an 'exploding pusher' compression producing low density cores(4.03). In contrast, if the fast electron range is small compared with the shell thickness ΔR, the shell is ablatively accelerated to compress an un-preheated core gas.

The fast electron range λ_h scales approximately as the hot electron temperature T_h squared. The hot electron temperature has been found both theoretically and experimentally to scale with $I\lambda^2$ (4.04)(4.05)(4.06). An incident $I\lambda^2$ of 10^{14} W cm^{-2} μm^2 will have a fast electron temperature of $\sim$ 2.1 keV(4.04), implying a range λ_h in glass of $\sim$ 0.7 μm(4.07). Frequency-doubled Neodynium Glass laser light has a wavelength of 0.53 μm so can be used at intensities up to 4 10^{14} W cm^{-2} on thick-walled targets ($\Delta R \sim$ 1.5 μm) with negligible fast electron preheat of the fill gas. For an unshaped laser pulse, as shown in section 4.2.2., the density achieved in an ablative implosion is not a strong function of the ablation pressure, but the peak temperature of the core material scales linearly with ablation pressure(4.08). In order to produce a hot, X-ray emitting core an ablation pressure of $\sim$ 20 Mbar is necessary, as will be shown in 4.2.2. Measurements of ablation pressure, performed in spherical geometry(4.09), indicate that incident intensities of $\sim$ 2 10^{14} W cm^{-2} for λ = 0.53 μm light, produce ablation pressures of 20 Mbars. The six-beam, λ = 0.53 μm symmetric illumination system at Rutherford Appleton Laboratory was able to provide pulses of up to 150 J, of 500 $\pm$ 100 picosecond duration. Targets of 150 μm diameter could therefore be illuminated with intensities of up to 4 10^{14} W cm^{-2} of green light in order to produce an ablatively driven implosion.

4.2 Theoretical Considerations

This section will show that, for the targets and illumination conditions used in the experiment, a hot dense core should be produced. A simple rocket model is used to calculate the energy imparted to the accelerated shell of the target. Some conclusions of a simple analytic model due to Ahlborn et al.[4.08] are presented in order to predict conditions in the compressed core. The predictions of this model are compared with one-dimensional MEDUSA simulations[4.10]. The magnitude of fast electron and radiation preheating of the target is estimated. This estimate is then included in the MEDUSA simulations in order to show the importance of preheat to the implosions.

4.2.1 The ablative acceleration of the shell

The acceleration of a shell of initial mass m_o inwards, due to the ablation of matter at a rate $\dot{m}$, can be approximated as that of a rocket ejecting mass. A mass δm is accelerated to the mean ion flow velocity $\overline{v_i}$ on ablation, to produce an increase δv in the velocity of the shell inwards. Simple momentum conservation gives:

$$\delta m \,.\, \overline{v_i} = - m_o(1 - f) \,.\, \delta v \tag{4.01}$$

where,

$$f = \frac{1}{m_o} \int_o^t \frac{dm}{dt}\, dt \tag{4.02}$$

i.e., f is the fraction of the original shell mass that has been ablated by the laser. Integrating equation (4.01) to obtain the shell velocity v and noting from (4.02) that $\delta f = \frac{\delta m}{m_o}$, we get:

$$v = \overline{v_i}\, \ell n(1 - f) \tag{4.03}$$

Integrating equation (4.03) in time to obtain the distance S travelled by the shell we obtain

$$S = \frac{m_o}{<\dot{m}>} \{ (1 - f)\ln(1 - f) + f \} \qquad (4.04)$$

Where $<\dot{m}>$ is an average mass ablation rate for the time between incidence of the laser and time = t

$$<\dot{m}> = \frac{m_o \, f(t)}{t} \qquad (4.05)$$

A time-averaged ablation pressure P_a can then be defined referenced to the initial target surface (radius R).

$$P_a = \frac{<\dot{m}>}{4\pi R^2} \, \overline{v}_i \qquad (4.06)$$

The initial shell mass m_o is given by

$$m_o = \rho_s \, . \, 4\pi R^2 \, \Delta R \qquad (4.07)$$

where R is the initial shell thickness and ρ_s the initial shell density. Therefore equation (4.04) can be rewritten as,

$$S = \overline{v}_i^{\,2} \, \frac{\rho_s \Delta R}{P_a} \{ (1 - f)\ln(1 - f) + f \} \qquad (4.08)$$

Equation (4.08) parameterizes the shell trajectory in terms of the ablated fraction f and can be used to calculate the average ablation pressure P_a as described in a later section.

4.2.2 Compression and heating of the core

The ablation pressure of $\sim$ 20 Mbars is sufficient to drive a strong shock through the shell. The shell material is accelerated and compressed to four times initial density by the strong shock[4.11]. The shock wave is reflected at the fill gas/shell interface and accelerates the interface to drive a shock into the fill gas. After the passage of the first strong shock through the shell the shell acceleration can be described by a simple rocket model, as in the last section. The shock passing through the fill gas is being driven by the shell which is accelerating. In the limit of low aspect ratio ($^R/_{\Delta R}$), i.e. thick-walled targets, the shell does not accelerate significantly during the passage of this shock through the fill gas. The subsequent implosion can then be described by a relatively simple analytic model [4.08]. The model of reference (4.08) allows the shell to accelerate uniformly until, at one-third the initial radius, it meets the reflected shock that has traversed the fill gas. The shell then is decelerated as the core gas is compressed by a series of progressively weaker shocks, reflecting between the shell and target centre, which approximate to an adiabatic compression.

For higher aspect ratios than 15 the model of reference (4.08) fails to agree with one-dimensional simulation in that the final density and temperature of the compressed material is over-estimated. However some conclusions of the model can be applied to the higher aspect ratio implosions ($\sim$ 50) in the experiment to be described. The observation is made that the shell accelerates to a radius $\frac{R}{3}$ before it encounters resistance from the core material. The 'dynamic pressure' ρv^2 of the shell when it reaches $\frac{R}{3}$ can then be used to calculate the final pressure and temperature in the core at the stagnation of the implosion. For higher aspect ratios, from comparison with simulations, the ρv^2 of the shell (and hence the kinetic energy imparted to it) peaks very near a radius of $\frac{R}{3}$. Therefore in the experiments the ρv^2 at this point will be taken as the maximum value. The shell kinetic energy U_s at this point is, from equation (4.03)

$$U_s = \frac{1}{2} m_o (1 - f) \{ \ln(1 - f) \}^2 \overline{v}_i^2 \tag{4.09}$$

where f can be obtained from equation (4.04) for $S = \frac{2}{3} R$.

The pressure of the core at stagnation P_f is approximately the peak ρv^2 of the shell multiplied by a geometrical factor G.

$$P_f = G \rho v^2 \tag{4.10}$$

The pressure amplification factor G is connected with the increase in momentum flux density in the shell as it converges towards the target centre. G is approximately the ratio of the shell's inner surface area at the $\frac{R}{3}$ point to that at the final core radius R_f at stagnation. One-dimensional simulations show that the mean density in the shell at the $\frac{R}{3}$ point is about twice the initial density ρ_s. The shell has been shock-compressed by a factor of four(4.11), which produces an average density of $\sim 2\rho_s$ due to the density decrease near the inner edge of the shell. Equation (4.10) can then be written as:

$$P_f = \frac{2}{9} \left[\frac{R}{R_f} \right]^2 \rho_s v^2 \tag{4.11}$$

Noting that the final density ρ_f is proportional to R_f^{-3}, equation (4.11) can be rewritten as:

$$P_f = \frac{2}{9} \left[\frac{\rho_f}{\rho_i} \right]^{2/3} \rho_s \{ \ln(1 - f) \}^2 \overline{v}_i^2 \tag{4.12}$$

where ρ_i is the initial fill gas density.

The adiabatic compression of the core from the $\frac{R}{3}$ point to R_f gives an expression for P_f in terms of ρ_f and the core pressure after the shock transit. The results of reference (4.08) are then:

$$\rho_f = 0.53 \frac{R}{\Delta R} \rho_s \tag{4.15}$$

and
$$T_f = 0.76 \frac{P_a}{\rho_i} \left[\frac{\rho_i}{\rho_s} \right]^{1/3} \left[\frac{R}{\Delta R} \right]^{2/3} \quad \text{eV} \tag{4.16}$$

P_a is in Mbars, ρ_i in g cm^{-3}.

Where T_f is calculated from P_f and ρ_f assuming a perfect fully ionised gas with A = 2Z, such that

$$T(ev) = 2.1 \frac{P\ (\text{Mbars})}{\rho\ (\text{g cm}^{-3})} \tag{4.17}$$

Table I includes typical values of ρ_f, P_f and T_f calculated from Ahlborn et al.(4.08). The temperatures produced in a typical laser compression for the target parameters quoted would be large enough to excite high energy X-ray spectra for core diagnosis.

Table I also shows results obtained with the one-dimensional hydrodynamic code MEDUSA(4.10) used by the author in its modified form, as described in Chapter 6. The simulation results show lower core temperatures than predicted by Ahlborn et al. but the temperatures, in excess of 1.5 keV, are still sufficient for X-ray spectroscopic core diagnosis, if reproduced in the experiment. The simulations assumed that radiation losses from the core gas were negligible; in common with Ahlborn et al.

4.2.3 Energy balance

The kinetic energy given to the inward-moving shell is expressed in equation (4.09). The ratio of the final internal energy of the core matter U_f, at temperature T_f to the peak shell kinetic energy is:

TABLE I

Comparison of analytic and numerical calculations of compressed core parameters. Targets were glass microballoons of 150 μm diameter containing $3.32\ 10^{-3}$ g cm^{-3} of Argon. An absorbed laser irradiance of $1.6\ 10^{14}$ W cm^{-2} produced an ablation pressure of 20 Mbars.

Wall Thickness		Ahlborn et al.			MEDUSA Simulation				
ΔR (μm)	$\frac{R}{\Delta R}$	ρ_f (g cm^{-3})	P_f (Mbars)	T_f (keV)	Simulation Number	ρ_f (g cm^{-3})	P_f (Mbars)	T_f (keV)	Final Shell ρR (Line Density) (g cm^{-2})
3.75	20	28	$4.9\ 10^4$	3.7	1	36	$2.0\ 10^4$	1.5	$6.4\ 10^{-2}$
2.14	35	48	$1.2\ 10^5$	5.3	2	38	$3.5\ 10^4$	2.3	$3.9\ 10^{-2}$
1.5	50	69	$2.2\ 10^5$	6.7	3	20	$2.3\ 10^4$	2.4	$1.7\ 10^{-2}$

$$\frac{U_f}{U_s} = \frac{4.8\ 10^7}{(1 - f)} \cdot \frac{R}{\Delta R} \cdot \frac{\rho_i}{\rho_s} \frac{T_f(\mathrm{eV})}{v^2(\mathrm{ms}^{-1})} \qquad (4.18)$$

for a perfect gas equation of state.

Using equation (4.03) and noting that from λ = 0.53 μm ablation experiments[4.09]:

$$\overline{v}_i = 5.8\ 10^5 (I_{14})^{0.13} \qquad \mathrm{m\ s^{-1}} \qquad (4.19)$$

where I_{14} is the absorbed irradiance in units of 10^{14} W cm^{-2}, we get:

$$\frac{U_f}{U_s} = \frac{1.43\ 10^{-4}}{\phi(f)} \frac{R}{\Delta R} \cdot \frac{\rho_i}{\rho_s} \cdot \frac{T_f(\mathrm{eV})}{(I_{14})^{0.26}} \qquad (4.20)$$

for λ = 0.53 μm, where

$$\phi(f) = \{ \ln(1 - f) \}^2 (1 - f)$$

An upper limit on the core temperature is obtained when it is noticed from simulation that a fraction of the shell is heated by the compression. For an aspect ratio of 50 the fraction g of the original shell that is heated to the final temperature T_f is about 15%. In order for energy to be conserved we must require that:

$$\frac{U_f}{U_s} < \frac{1}{1 + 3g\left(\frac{\Delta R}{R}\right)\left(\frac{\rho_s}{\rho_i}\right)} \qquad (4.21)$$

For most of the targets used in the experiment, $\rho_i \sim 8\ 10^{-3}$ g cm^{-3}. therefore for aspect ratios of 60 and below:

$$\frac{U_f}{U_s} \lesssim \frac{1}{3g} \frac{R}{\Delta R} \frac{\rho_i}{\rho_s} \qquad (4.22)$$

This is typically 20%. Substituting for $\frac{U_f}{U_s}$ from equation (4.20) we then get a limit on the expected final core temperature of:

$$T_f \lesssim 2.3 \frac{\phi(f)}{g} I_{14}^{0.26} \quad \text{keV} \tag{4.23}$$

For most of the targets used the ablated fraction was about 40%, which for an absorbed irradiance of 10^{14} W cm^{-2} gives a limit on the expected core temperature of 2.4 keV.

The expected core temperature is therefore limited by $\phi(f) \sim f^2$ in this approximation. The ablated fraction was measured directly in the experiments and also could be calculated from previous measurements of ablation rate[4.09]. The combination of an incident irradiance of 3 10^{14} W cm^{-2} with shells of aspect ratio between 30 and 60 should produce cores hot enough ($\sim$ 2 keV) to diagnose spectroscopically.

4.2.4 Preheat

The preheat produced by the shock transit through the core gas is included in the model of Ahlborn et al. If the core gas is assumed to be fully ionised to start with, then the deviation from the adiabat when it is compressed by the shock can be parameterised by equating the temperature and density, after shock compression, with that obtained after an adiabatic compression from a temperature T_{ph}. The temperature T_{ph} can then be shown to be:

$$T_{ph} \simeq 1.21 \frac{P_a \text{ (Mbars)}}{\rho_s \text{ (g cm}^{-3})} \quad \text{eV} \tag{4.24}$$

This equivalent preheat temperature is typically 9 eV for a 20 Mbar ablation pressure and a glass microballoon.

The preheat of the target due to the action of fast electrons can be quantified using compilations of experimental measurements of hot electron temperature and deposition in targets[4.06][4.07]. The characteristic depth of deposition λ_h is given by[4.07]:

$$\lambda_h = \frac{1.8}{\rho(\mathrm{g\ cm^{-3}})} \left[\frac{I_{inc}\ \lambda_{\mu m}^2}{10^{14}\ \mathrm{W\ cm^{-2}}}\right]^{0.9} \ \mu\mathrm{m} \tag{4.25}$$

where I_{inc} is the incident laser irradiance in S.I. units (i.e. W m^{-2}). For a slab with Lagrangian coordinate x, with the laser incident at x = 0, the specific energy deposition due to fast electrons is:

$$E_{fe} = 5.6\ 10^{-4}\ \eta_{fe} \left(\frac{I_{inc}}{10^{14}\ \mathrm{W\ cm^{-2}}}\right)^{0.1} \lambda_{\mu m}^{-1.8}\ \tau(\mathrm{picosec})\ e^{-\frac{x}{\lambda_h}}\ \mathrm{J/ng} \tag{4.26}$$

at a depth x in the slab. Where τ is the time since the laser was switched on and η_{fe} is the conversion factor of incident energy into fast electron preheat energy, typically 6%[4.06] for short pulse λ = 1.06 μm illumination. The factor η_{fe} would be expected to be less than 6% for the λ = 0.53 μm experiment to be described, due to the longer density scale lengths associated with a long laser pulse, and the increased importance of inverse bremsstrahlung absorption with the shorter wavelength. Fast electron transport straight into the target could also be reduced for longer pulses due to lateral transport of electrons or the increased importance of circulating fast electrons in the ablation plasma as described for plane target experiments in Chapter 2. For the conditions prevailing in the experiment to be described the fast electron preheat can be treated as negligible if at a depth x in the shell the heating due to fast electrons is much smaller than the heating by the shock when it gets to that depth[4.08]. The dominant mechanism causing the shell to decompress during acceleration would then be the heating due to the initial shock transit of the shell. The delay time for the shock to reach a depth x is:

$$\tau \;=\; x(\mu m)\left[\frac{3}{4}\,\frac{\rho_s\ (g\ cm^{-3})}{P_a\ (Mbars)}\right]^{\frac{1}{2}} 10^2 \quad \text{picosec} \tag{4.27}$$

The shell heating associated with the shock is:

$$E_s \;=\; \frac{3}{8}\,\frac{P_a\ (Mbars)}{\rho_s (g\ cm^{-3})}\ 10^{-4} \qquad J/ng \tag{4.28}$$

Comparison of this formula with tabulated Hugoniot and equation of state data[4.17] indicates good agreement for the range of ablation pressure of interest.

For an incident irradiance of 4 10^{14} W cm^{-2} of λ = 0.53 μm light incident on a glass microballoon the shock heating is 2.9 10^{-4} J/ng. Assuming $\eta_{fe} \approx 0.06$, throughout the laser pulse, the fast electron preheat before the shock arrives is, from equation (4.26), ∿ 9 10^{-4} J/ng for depths of ½ to 1 μm in the shell. Therefore fast electron preheat may be significant on some of the thin-walled (∿ 1 μm) targets. Note that an energy deposition of 1 J/ng is equivalent to an energy per atom of:

$$\varepsilon \;=\; \langle A\rangle\ 1.04\ 10^4 \qquad eV/Atom \tag{4.29}$$

where A is the mean mass number of the material. A deposition of 9 10^{-4} J/ng in glass is equivalent to 190 eV/Atom.

The preheat of the core gas by fast electrons is given by:

$$E_{fe} = 3\ 10^{-5}\left[\frac{I_{inc}}{10^{14}\ W\ cm^{-2}}\right]\frac{\eta_{fe}\ \tau(psec)}{\rho_{gas}(g\ cm^{-3})R(\mu m)}\ e^{-\left(\frac{\Delta R}{\lambda_h}\right)glass}\left\{1 - e^{-\frac{2R}{\lambda_{gas}}}\right\} \quad J/ng \tag{4.30}$$

where λ_{gas} for the fill gas is typically 240 μm (10 bar Neon, I_{inc} = $4\ 10^{14}$ W cm^{-2}, $\lambda_{\mu m}$ = 0.53). For a 1.5 μm thick shell of 150 μm diameter the core preheat for the illumination conditions quoted is of the order of $3\ 10^{-5}$ J/ng in the 50 picosecs before the shock reaches the fill gas. The above estimates of fast electron preheat are very approximate due to the lack of knowledge of fast electron behaviour in long-pulse irradiated spherical targets.

Preheat due to X-ray radiation from the ablation plasma is difficult to estimate. The frequency-dependent photon range λ_ν can be calculated from tables of X-ray mass attenuation coefficients for cold materials[4.12]. The cold material opacities are a good approximation for shell temperatures below 100 eV as the photon energies are still much greater than the electron energies present, and K shell ionisation will not be significant. When preheat is included in ablative implosion simulations, (e.g. those of Table IV), the shell stays at a temperature below 100 eV during the acceleration phase of the implosion.

If the ablation plasma, close to the shell surface, consists of a large number of isotropic sources emitting a total spectrum, I_ν (photons ster^{-1} Hz^{-1} s^{-1}), a radiation conversion factor η_ν can be defined such that:

$$\eta_\nu\, h\nu\, I_{inc} \;=\; \frac{4\pi\, h\nu\, I_\nu}{S} \qquad \mathrm{W\ m^{-2}\ Hz^{-1}} \tag{4.31}$$

where S is the target surface area in m^2. The isotropic emission of radiation by the ablation plasma means that only about half of the radiation enters the shell. The X-ray irradiance, due to radiation between ν and $\nu + d\nu$, through a surface a depth x in the shell can be shown to be:

$$P_\nu \, d\nu = \frac{4\pi \, h\nu \, I_\nu}{S} \, d\nu \, . \, \tfrac{1}{2} \int_{-\frac{\pi}{2}}^{\frac{\pi}{2}} e^{-\frac{x}{\cos\theta . \lambda_\nu}} \sin\theta \, d\theta \quad W \, m^{-2} \qquad (4.32)$$

where θ is the angle a ray makes to the normal to the target surface. The integration over θ is performed assuming that the curvature of the surface is negligible over the absorption length of a ray. Substituting from equation (4.31) and differentiating (4.32) with respect to x, we obtain the energy deposition rate:

$$E(\nu,x)d\nu = h\nu \, \eta_\nu \, d\nu \, I_{inc} \frac{1}{\rho \, \lambda_\nu} \int_0^{\frac{\pi}{2}} e^{-\frac{x}{\lambda_\nu} \frac{1}{\cos\theta}} \tan\theta \, d\theta \qquad W \, kg^{-1} \qquad (4.33)$$

The integral is an exponential integral $Ei(\frac{x}{\lambda_\nu})$ such that:

$$Ei(\frac{x}{\lambda_\nu}) = \int_{\frac{x}{\lambda_\nu}}^{\infty} \frac{e^{-u}}{u} \, du \qquad (4.34)$$

For $0.15 < \frac{x}{\lambda_\nu} < 2.4$, $Ei(\frac{x}{\lambda_\nu})$ can be replaced by:

$$Ei(\frac{x}{\lambda_\nu}) \simeq \frac{3}{2} \, e^{-\frac{\sqrt{3}\, x}{\lambda_\nu}} \qquad (4.35)$$

which is accurate to 20% within the limits quoted. Therefore the photon range λ_ν can be replaced by a reduced range:

$$\lambda'_\nu = \frac{\lambda_\nu}{\sqrt{3}} \qquad (4.36)$$

The deposition of energy due to radiative preheat is then:

$$E_r \simeq \left[\frac{I_{inc}}{10^{14} W \, cm^{-2}}\right] \frac{\tau(psec)}{\rho_s(g \, cm^{-3})} \int_0^{\infty} h\nu \, \eta_\nu \, \frac{\sqrt{3}}{2} \, \frac{e^{-\frac{x}{\lambda'_\nu}}}{\lambda'_\nu(\mu m)} \, d\nu \, 10^{-3} \qquad J/ng \qquad (4.37)$$

From equation (4.37), for glass the energy deposition rate by radiation for constant η_ν

peaks at photon energies of 1.1 keV and 1.4 keV for depths of ½ and 1 micron respectively.

Some measurements have been made of the soft X-ray spectrum produced by 1.06 μm laser irradiation of plastic and tungsten-glass targets[4.13][4.14][4.15]. The spectra measured are effectively constant in intensity (keV/keV) between $h\nu \sim 0.2$ keV and 1.2 keV, to within a factor of 2. At 1.2 keV the intensity decreases rapidly, being down by 2 orders of magnitude at a photon energy of 2 keV. Measurements for 600 psec pulses of 0.53 μm light[4.16], using X-ray diodes, show only 3% of the total X-ray energy lies above 1.8 keV and that 90% lies between 0.2 keV and 1.8 keV. The radiation conversion factor η_ν (photons J^{-1} Hz^{-1}), as defined in equation (4.31), is proportional to the intensity expressed in keV/keV, $\div\ h\nu$, an estimate of the effect of radiative preheat can be made by taking η_ν as constant between 0.2 keV and 1.2 keV and zero elsewhere. Radiation below 0.2 keV will be absorbed very close to the ablation region and will not contribute directly to preheating of the target. The integrated radiation conversion fraction:

$$F_r = \int \eta_\nu\, h\nu\, d\nu \tag{4.38}$$

has been measured[4.16] as $\stackrel{\sim}{\sim}$ 25% of the absorbed energy for Titanium targets. The Z scaling of conversion[4.14] indicates that glass will have a conversion fraction of $F_r \sim 6\%$ of incident energy in the spherical geometry experiment to be described. Solving equation (4.38) for η_ν constant between 0.2 and 1.2 keV gives

$$\eta_\nu = \frac{F_r}{27} \quad \text{photons } J^{-1}\ Hz^{-1} \tag{4.39}$$

The energy deposition rate is then:

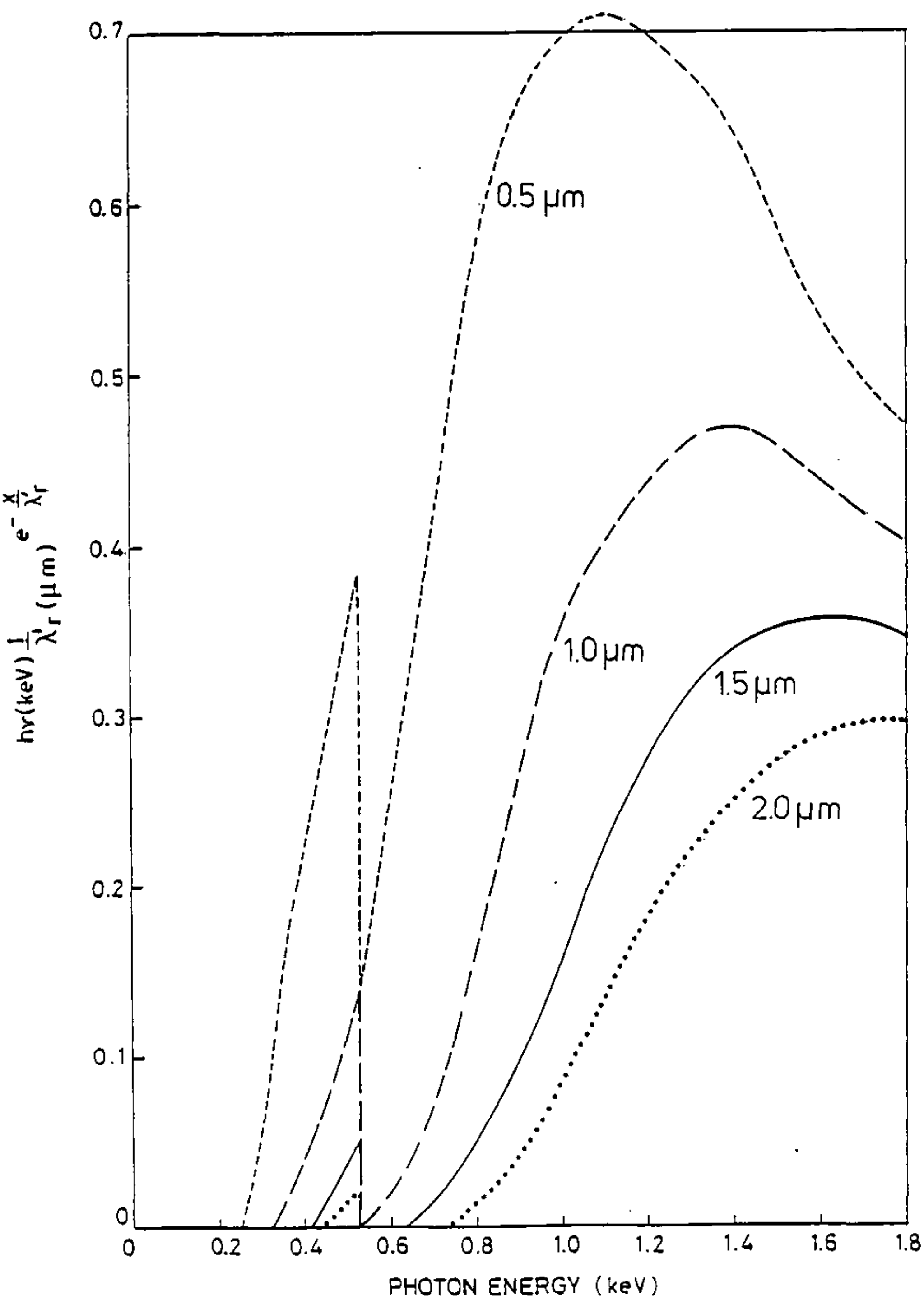

Fig. 4.1. Radiative energy deposition rate in SiO_2 for various depths x. (Ablation plasma is at x = 0.)

$$E_r(x) \simeq F_r \left(\frac{I_{inc}}{10^{14}\ \mathrm{W\ cm^{-2}}} \right) \frac{\tau(\mathrm{psec})}{\rho_s(\mathrm{g\ cm^{-3}})} A(x)\ 10^{-3}\ \mathrm{J/ng} \qquad (4.40)$$

where the integral,

$$A(x) = \int_{0.2}^{1.2} 1.24\, \frac{e^{-\frac{x}{\lambda'_\nu}}}{\lambda'_\nu(\mu\mathrm{m})}\, \varepsilon\, d\varepsilon \quad \mathrm{J\ \mu m^{-1}} \qquad (4.41)$$

can be evaluated numerically. The quantity ε is the photon energy $h\nu$ in keV. Fig. 4.1 shows the integrand of equation (4.41) plotted for various glass depths. If a preheating spectrum with η_ν not constant were used, the curves of Fig. 4.1 would be multiplied by the frequency dependence of η_ν. Integrating equation (4.41) gives values of A(x) of 0.52, 0.20, 0.12 and 0.05 for depths in SiO_2 of 0.5, 1.0, 1.5 and 2 μm respectively. Using equation (4.27) for the time the shock takes to reach a depth x and substituting into equation (4.40) we obtain:

$$E_r(x) \simeq 2.9\ 10^{-3}\ x(\mu\mathrm{m})\ A(x) \quad \mathrm{J/ng} \qquad (4.42)$$

($I_{inc} \equiv 4\ 10^{14}\ \mathrm{W\ cm^{-2}}$, $\lambda_{\mu m} = 0.53$, $\rho_s = 2.6\ \mathrm{g\ cm^{-3}}$, $P_a = 20$ Mbars, $F_r = 0.06$).

Inserting the values of A(x), for constant η_ν a preheat of $7.5\ 10^{-4}$ to $3\ 10^{-4}$ J/ng is obtained over the depth range ½ to 2 μm before the shock arrives.

The shock heating predicted by equation (4.28) is not significantly greater than the heating due to radiation or fast electrons. Therefore for the irradiance conditions considered the shell preheating due to fast electrons and radiation will dominate over shock preheat. Combining the results of equations (4.26) and (4.40) the rate of preheating of the shell during the acceleration phase is summarised in Table II below, for two incident irradiances.

TABLE II

Depth in Glass Shell (μm)	Fast Electron Preheat J ng^{-1} $psec^{-1}$		Radiative Preheat J ng^{-1} $psec^{-1}$		Total Preheat J ng^{-1} $psec^{-1}$	
	$I_{inc} = 10^{14}$ W cm^{-2}	$I_{inc} = 4\ 10^{14}$ W cm^{-2}	$I_{inc} = 10^{14}$ W cm^{-2}	$I_{inc} = 4\ 10^{14}$ W cm^{-2}	$I_{inc} = 10^{14}$ W cm^{-2}	$I_{inc} = 4\ 10^{14}$ W cm^{-2}
0.5	$1.1\ 10^{-5}$	$5.9\ 10^{-5}$	$1.2\ 10^{-5}$	$4.8\ 10^{-5}$	$2.3\ 10^{-5}$	$1.1\ 10^{-4}$
1.0	$1.1\ 10^{-6}$	$2.9\ 10^{-5}$	$4.5\ 10^{-6}$	$1.8\ 10^{-5}$	$5.6\ 10^{-6}$	$4.7\ 10^{-5}$
1.5	0	$1.4\ 10^{-5}$	$2.8\ 10^{-6}$	$1.1\ 10^{-5}$	$2.6\ 10^{-6}$	$2.5\ 10^{-5}$
2.0	0	$7\ 10^{-6}$	$1.3\ 10^{-6}$	$4.6\ 10^{-6}$	$1.3\ 10^{-6}$	$1.2\ 10^{-5}$

The units of Joules per nanogramme per picosecond are chosen as relevant to the timescale of the implosion of a microballoon. The temperature rise associated with the deposition of energy by preheat can be inferred from tabulated equation of state data[4.17]. Table III below shows the specific internal energy of SiO_2 in J/ng as a function of density and temperature. The shell is preheated for a period of the order of 300 picoseconds during the implosion, a deposition rate of 10^{-5} J ng^{-1} psec^{-1} will then give an increase in internal energy of $3\ 10^{-3}$ J/ng and a temperature rise of 50 eV.

TABLE III

SPECIFIC INTERNAL ENERGY OF SiO_2 (J/ng)

Density g cm^{-3}	1	2.6	5	10
300 ^{0}K	$3.4\ 10^{-6}$	$0.5\ 10^{-6}$	$4.3\ 10^{-6}$	$5.9\ 10^{-6}$
1 eV	$1.9\ 10^{-5}$	$1.6\ 10^{-5}$	$1.9\ 10^{-5}$	$7.3\ 10^{-5}$
2 eV	$2.7\ 10^{-5}$	$3.3\ 10^{-5}$	$3.9\ 10^{-5}$	$9.1\ 10^{-5}$
5 eV	$1.0\ 10^{-4}$	$1.0\ 10^{-4}$	$1.0\ 10^{-4}$	$1.5\ 10^{-4}$
10 eV	$3.1\ 10^{-4}$	$2.8\ 10^{-4}$	$2.6\ 10^{-4}$	$2.8\ 10^{-4}$
20 eV	$8.8\ 10^{-4}$	$7.6\ 10^{-4}$	$6.8\ 10^{-4}$	$6.4\ 10^{-4}$
50 eV	$3.2\ 10^{-3}$	$2.8\ 10^{-3}$	$2.5\ 10^{-3}$	$2.3\ 10^{-3}$

The preheated shell will expand as it is accelerated, due to its internal pressure. The rate of decompression of the shell can be estimated by assuming that it expands at the ion sound speed. However

TABLE IV

Simulation Number	Preheat Power Input J ng^{-1} ps^{-1}	ρ_f (g cm^{-3})	T_f (keV)	P_f (Mbars)	Shell peak ρv^2 (Mbars)	Compressed Shell		
						ρR (g cm^{-2})	Diameter (μm)	Density (g cm^{-3})
3.	Standard MEDUSA Fast Electron Treatment (from Table I)	20	2.4	2.3 10^4	7.0 10^3	1.7 10^{-2}	18	$\sim$ 20
4.	10^{-6}	16	2.2	1.8 10^4	6.7 10^3	1.4 $10^{=2}$	23	13
5.	3 10^{-6}	11	2.0	1.1 10^4	2.7 10^3	1.0 10^{-2}	27	7
6.	10^{-5}	4	1.7	3.2 10^3	5.7 10^2	5.0 10^{-3}	40	2
7.	3 10^{-5}	2.2	1.6	1.7 10^3	1.4 10^2	2.3 10^{-3}	$\sim$ 60	0.8
8.	10^{-4}	0.3	1.1	1.7 10^2	$\sim$ 15	7.0 10^{-4}	$\sim$ 80	$\sim$ 0.2

as the temperature rise associated with the preheat is time dependent the best way of estimating the influence of decompression is to include preheat as a variable in MEDUSA numerical simulations. MEDUSA contains an equation of state calculation that has been checked against tabulation data[4.17]. The simulation results shown in Table I had fast electron production included as a fraction of the laser energy resonantly absorbed at critical density, the fast electron temperature was calculated using empirical formulae[4.04], then energy deposition calculated from the electron range[4.18]. (See Chapter 6, section 6.1.1.) The simulation with a shell aspect ratio of 50 (simulation 3 in Table I) was re-run without the MEDUSA treatment of fast electrons but with an energy deposition, due to preheat applied uniformly throughout the shell. The energy deposition was varied from 10^{-6} J ng^{-1} psec^{-1} to 10^{-4} J ng^{-1} psec^{-1}. The results of the simulations are shown in Table IV together with the simulation from Table I for comparison. No preheat, apart from shock preheat, was applied to the fill gas.

The fast electron preheat in the usual MEDUSA simulation has less effect than an applied deposition of 10^{-6} J ng^{-1} psec^{-1}. This is probably due to the low fraction of the incident laser energy actually being resonantly absorbed at critical density. The simulations allowed for refraction of the six beams in the low density plasma and hence collisional absorption at densities lower than critical density. (See Chapter 6, section 6.1.2.3.) The small amount of preheat due to fast electrons in Simulation 3 probably reflects the reduction in fast electron production observed in long pulse experiments[4.19].

Comparison of the radiative preheat shown in Table II with the effects of that preheat in the simulations of Table IV indicates that radiative preheat alone can provide energy depositions of between 10^{-6} and 3 10^{-5} J ng^{-1} psec^{-1} through a 2 μm thick glass shell, sufficient to

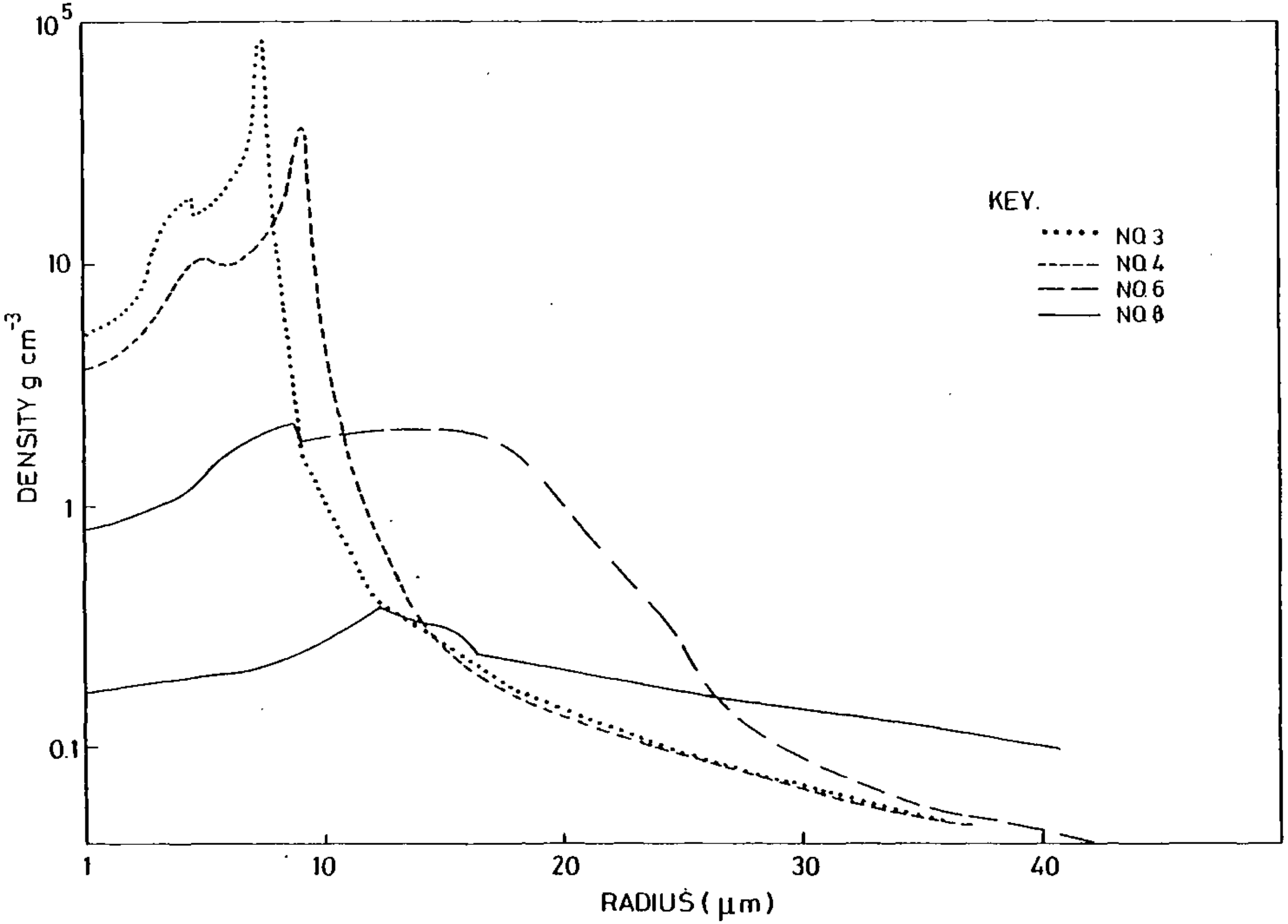

Fig. 4.2. Density-radius plots at the stagnation point of the implosion for some of the simulations of Table IV.

reduce drastically the core density and pusher ρR obtained in the experiment. Fig. 4.2 shows density-radius plots for the simulations of Table IV. The decompression due to preheat is seen to reduce dramatically the densities obtained in Simulation 3.

4.2.5 Drive uniformity

In the limit of negligible preheat, the final density and temperature obtained in an ablative implosion can be set by the degree of spherical convergence of the shell. To achieve radial compression ratios of about 14 the shell velocity must be uniform to within ± 3%[4.20]. This restriction implies that the ablation pressure must be uniform to within about 6%. The restriction on the illumination uniformity is not quite so tight because the separation between the low density absorption region and the ablation point allows a certain amount of thermal smoothing of irregularities in irradiation. The smoothing is effective where scale lengths of non-uniformities are small compared with the separation of the absorption and ablation regions[4.21]. This separation increases with laser wavelength and irradiance[4.22] and is found to produce a smoothing efficiency of pressure modulations that scales as $(I\lambda^2)^{0.67}$ [4.23]. Smoothing is found to become suddenly effective above an $I\lambda^2$ of 10^{14} W cm^{-2} μm^2 incident[4.23]. Specifically, plane target experiments at an incident irradiance of 2 10^{14} W cm^{-2}, in a 350 picosec pulse of 0.53 μm light with a spatially modulated beam, have shown that a 4:1 modulation in irradiance produces only a 10% variation in drive pressure across the target[4.23]. Two-dimensional raytracing applied to the density and temperature profiles predicted by the one-dimensional code MEDUSA (see Chapter 6) indicate that with the focusing and irradiance conditions used in the experiment to be described, (6 beams focused 3.6 target radii beyond the centre of the target), illumination uniformity of ± 20% is achieved. However the results of the plane target experiments(4.23) may not be directly applicable to the case of a spherically converging shell so a modulation may still be imprinted on the velocity of the pusher.

4.3 Experiment

The experiment used six synchronous laser beams of green light to irradiate spherical glass microshells. The targets ranged in diameter from 100 μm to 180 μm with glass wall thicknesses of typically 1 - 2 μm. A plastic layer of 1 - 2 μm was coated over the glass in some of the targets. The microballoons were filled with Argon, Neon and Deuterium - Tritium mixtures. Laser pulses of 500 picoseconds in duration with energies up to 150 J (summed over six beams) produced incident irradiances of typically $3\ 10^{14}$ W cm^{-2}. The f/1 lenses were focused 3.6 target radii beyond the centre of the target in order to improve illumination uniformity. These irradiation conditions led to measured absorption fractions of 30 to 35% of the incident energy. Data was obtained using time and space resolved X-ray spectroscopy and time-integrated X-ray pinhole imaging. Nuclear reaction products were detected from some of the targets containing Deuterium - Tritium.

4.3.1 Time integrating X-ray pinhole camera

An X-ray pinhole camera with two 10 μm diameter pinholes was used to image the X-ray emission of the target. The two pinholes were filtered with layers of Beryllium and Aluminium of different thicknesses. Fig. 4.3 shows a typical set of pinhole pictures. The picture on the left shows a ring of X-ray emission surrounding a bright spot in the

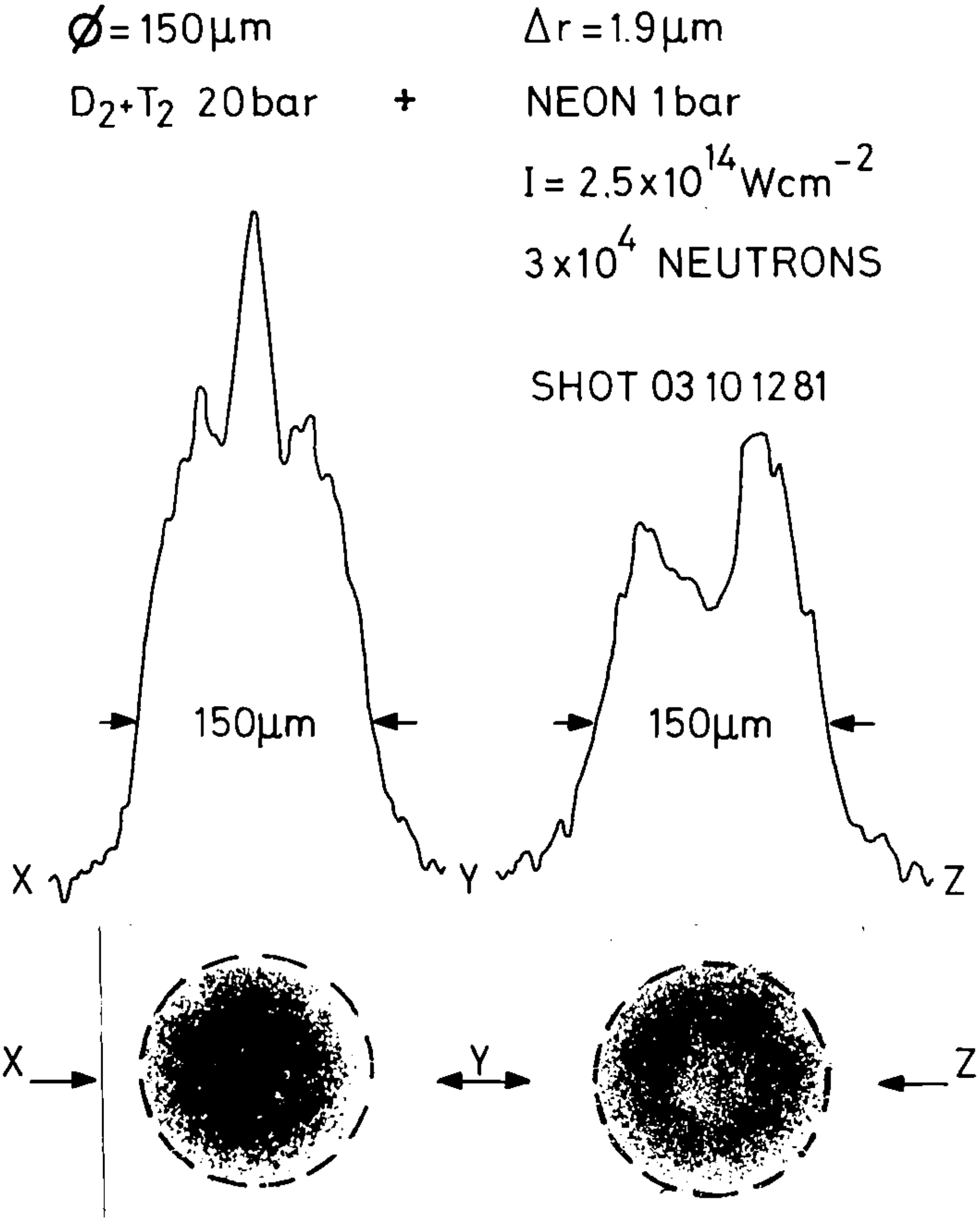

Fig. 4.3. X-ray pinhole images of implosion. Image at left is through Filter A (25 µm Al + 15 µm Be); image at right through Filter B (125 µm Be + 10 µm Al).

centre. The ring of emission corresponds to the ablation plasma at the outside of the shell, marking the shell's trajectory as it is accelerated inwards. The bright central spot consists of emission from the hot, dense core, produced by the implosion. The pinhole picture on the left had a filter of 25 μm of Aluminium plus 15 μm of Beryllium (Filter A). The central core emission is not visible in the picture on the right which was filtered with 125 μm of Beryllium plus 10 μm of Aluminium (Filter B). The transmission of the two different filter combinations is shown in Fig. 4.4. Filter A (25 μm Al + 15 μm Be) has higher transmission for X-ray energies below the Aluminium K edge at 1.56 keV. However Filter B (125 μm Be + 10 μm Al) is more transmitting for X-rays with energies above the Aluminium K edge. Integrating the transmission of the filters for an X-ray continuum of the form

$$I(\nu) \propto e^{-\frac{h\nu}{kT_e}} \tag{4.43}$$

leads to an intensity ratio of order unity for $T_e \approx 500$ eV. The ablation plasma imaged in the two pictures is of similar brightness in both, implying $T_e \sim 500$ eV. This temperature is consistent with measurements of the slope of the Silicon recombination continuum emission detected by an X-ray spectrometer. The relative brightness of the core in the two pictures is consistent with an electron temperature of 200 ± 50 eV.

The core is surrounded by a region of low luminosity which is a self backlit absorption picture of the compressed glass of the shell. In the example shown in Fig. 4.3 the opaque region has a diameter of 60 μm. If the 60% of the 1.9 μm shell that is not ablated by the laser

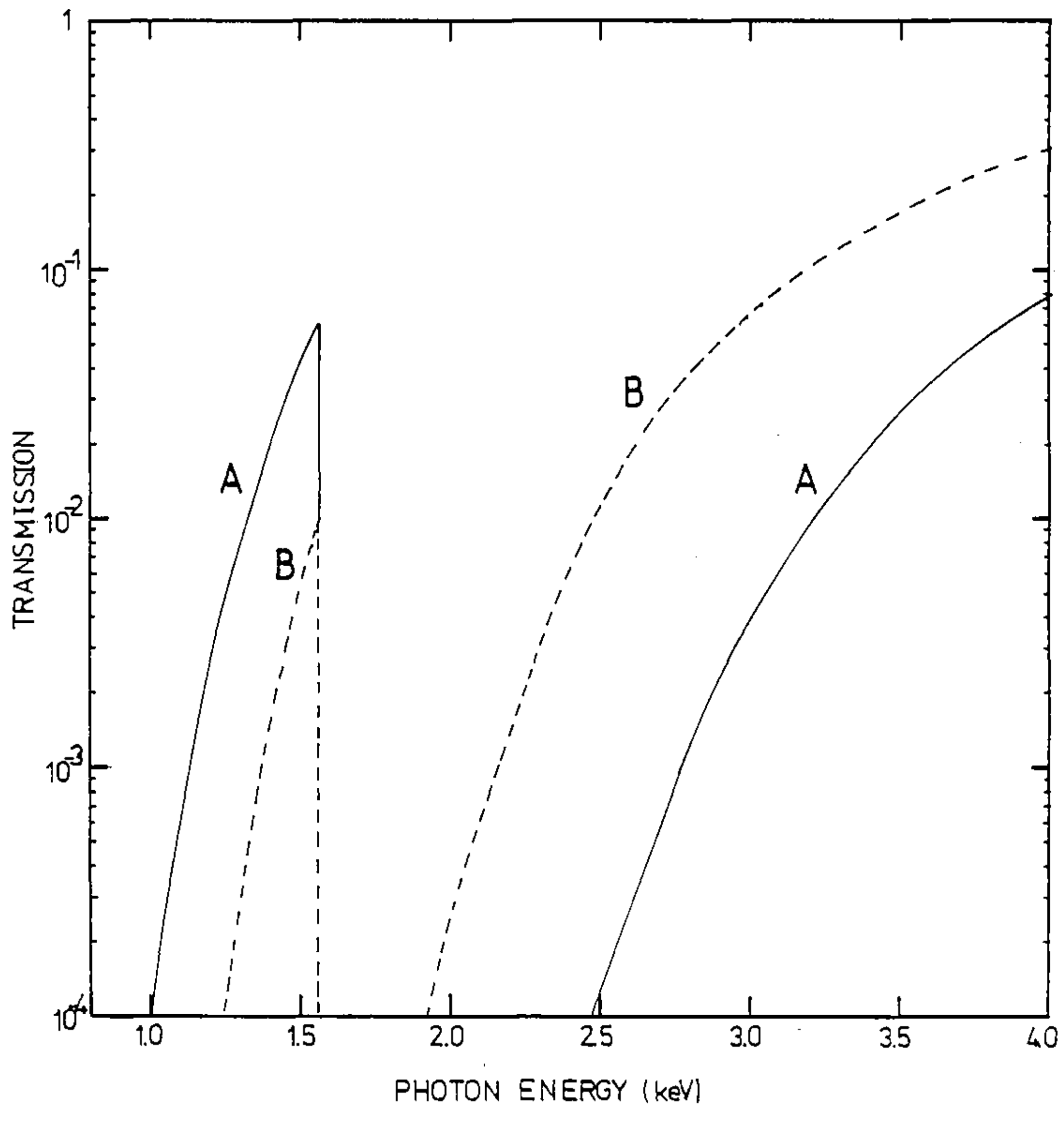

Fig. 4.4. Photon energy dependent transmission of the pinhole filters used for the images in Fig. 4.3.

Filter A: 25 μm Aluminium + 15 μm Beryllium
Filter B: 125 μm Beryllium + 10 μm Aluminium

is all contained in the opaque region then a glass density of ~ 2 g cm^{-3} is implied. The areal density of the glass can be estimated as $\sim 6\ 10^{-3}$ g cm^{-2}. Similarly, assuming that the gas fill is all in the 30 μm diameter emitting core leads to a compressed core density estimate of 0.6 g cm^{-3}. However some glass could also be in the bright central emitting region so 0.6 g cm^{-3} could be a lower limit on the density of the compressed gas.

4.3.2 Time-resolved X-ray spectroscopy

An X-ray streak camera with a Von Hamos curved crystal attached was used to time resolve X-ray spectra from the target. The crystal, described in Chapter 3, was P.E.T. (2d = 8.74 Å) and was initially used to try and detect Argon lines, emitted from the core of Argon-doped targets. The cores produced by the implosions were of too low a temperature ($\sim$ 200 eV) to produce Argon resonance lines, therefore the device was used to provide high dispersion Silicon spectra. Fig. 4.5 shows the Lyα line of Hydrogen-like Silicon, (1s - 2p of Si XIV) together with its dielectronic satellites. The satellite lines correspond to 1s - 2p transitions in Helium-like Silicon where the second electron is in an excited state, providing a perturbation on the transition. The resulting satellite line has a wavelength very close to the Lyα line. The satellites visible in the streaked spectrum have a duration similar to that of the laser pulse (500 picosec). The main Lyα line lasts for a long time after the laser pulse, as the remnants of the ablation plasma stay hot as they move away from the target. The short burst of continuum emission at point β in Fig. 4.5 corresponds to the stagnation of the implosion. The continuum from the core is escaping through the Silicon K window of the glass pusher. Fig. 4.6 is

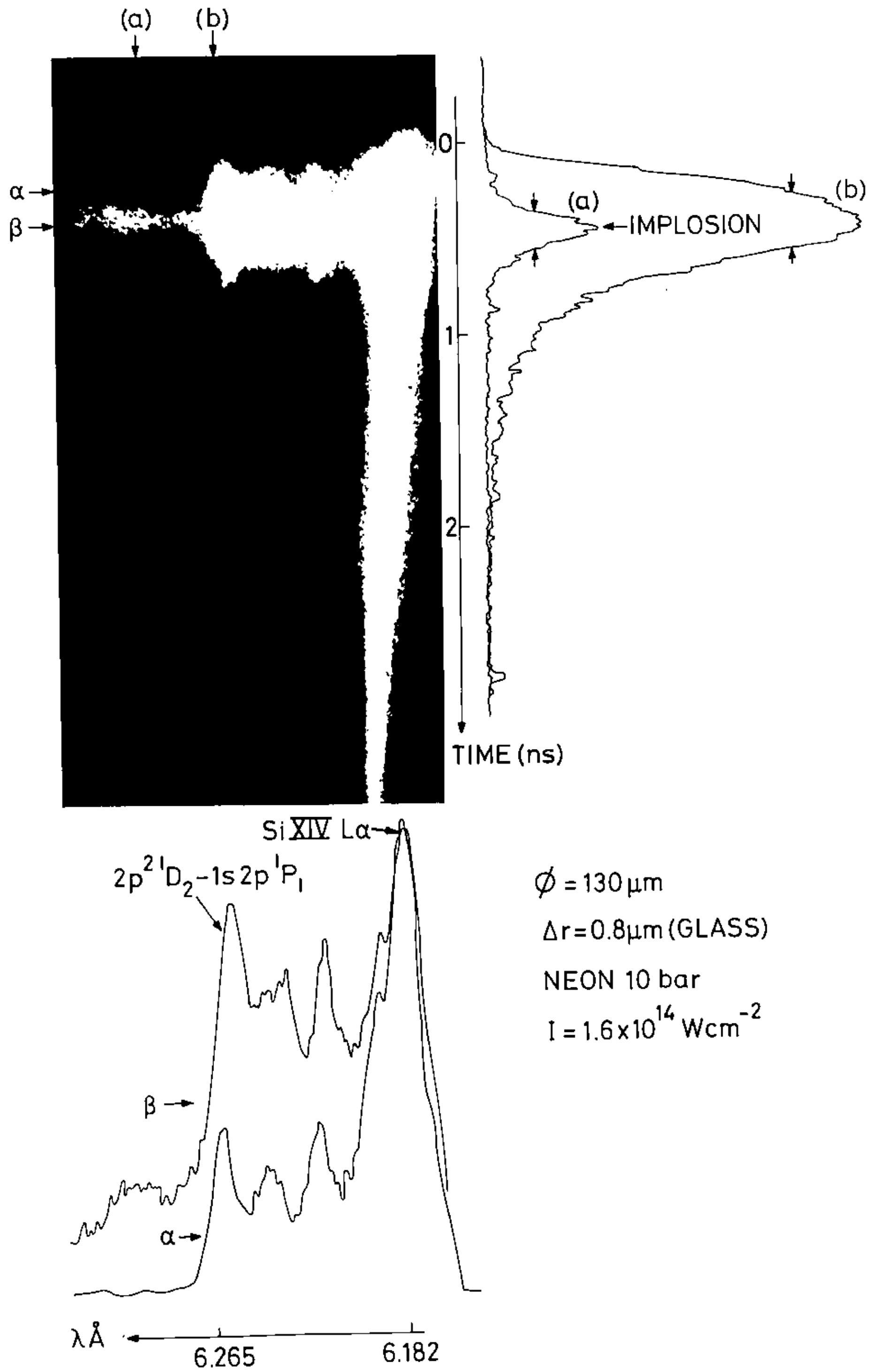

Fig. 4.5. Time-resolved Si Lyman α emission from imploding glass microballoon.

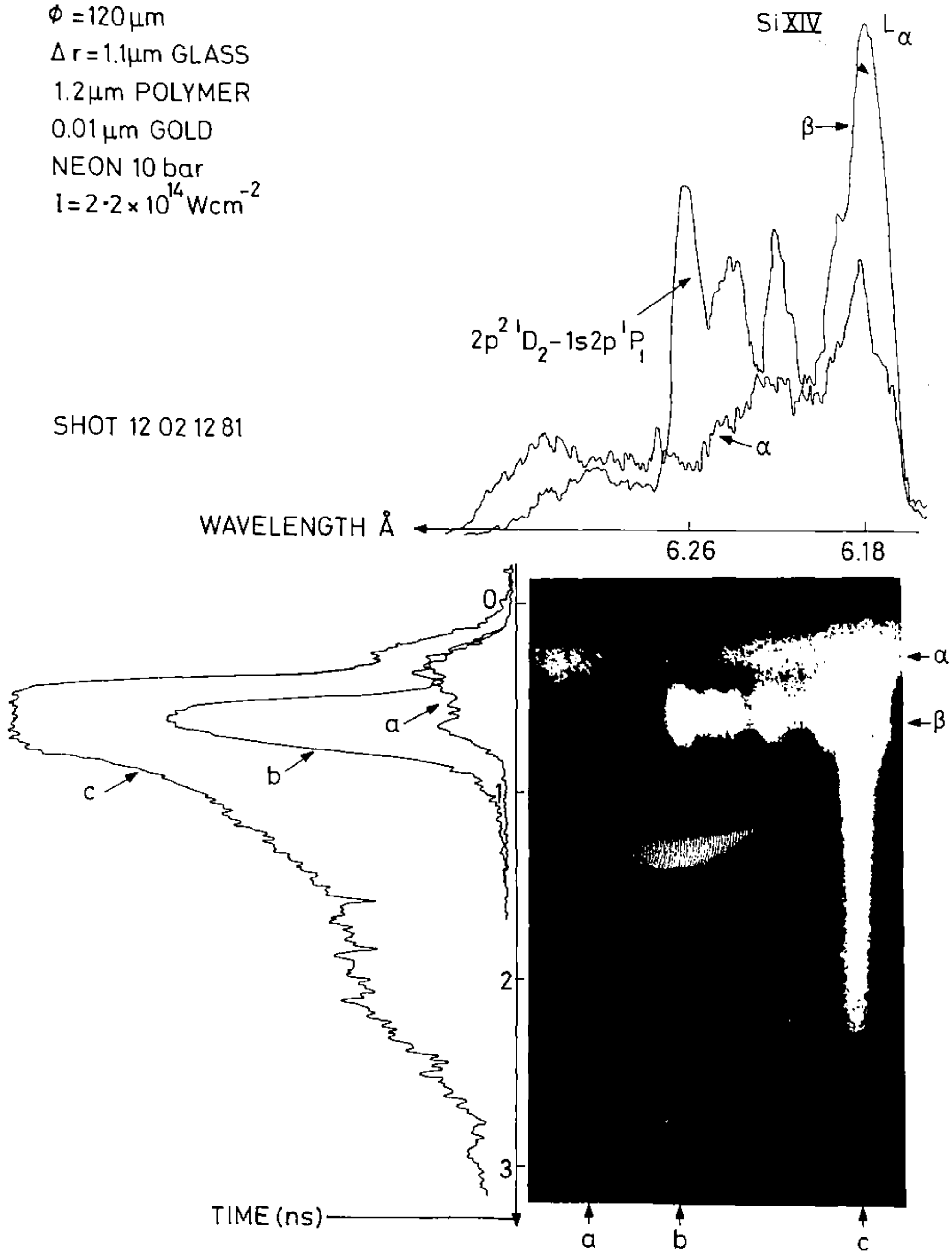

Fig. 4.6. Time-resolved Si Lyman α and Au continuum emission from imploding gold and plastic coated glass microballoon.

a streak of a target which was coated with 1.2 μm of plastic with a fiducial gold layer 10 nm thick on top. The satellites to the Lyα line are delayed until the end of the laser pulse owing to the time required to burn off the plastic. Trace 'a' on Fig. 4.6 shows a burst of continuum appears midway through the period of Silicon emission, corresponding to the stagnation point. An X-ray pinhole image from the same shot as Fig. 4.6 is shown in Fig. 4.7. The emission from the fiducial gold layer is spatially separated from the emission from the silicon by a region of low emission. This region corresponds to the period when the implosion is being driven by the ablation of the plastic layer. The delay time before silicon emission commences is 320 picosecs from Fig. 4.6, indicating a mass ablation rate of 4.6 10^5 g cm^{-2} s^{-1}, in good agreement with an extrapolation of ablation rate measurements made at lower irradiances[4.09]. The mean ablated ion velocity on this shot was 5.6 10^7 cm/s giving an ablation pressure (equation (4.06)) of 26 Mbars. The time resolution of the instant of burn through coupled with the pinhole image measurement of the displacement of the shell during acceleration leads to an alternative estimate of ablation pressure of 23 Mbars from

$$S = \frac{1}{2} \frac{Pa}{\rho_s \Delta R} t^2 \qquad (4.44)$$

Without using the time resolution, a third estimate of ablation pressure is obtained from equation (4.08) where the displacement is calculated from a rocket model. The ablated fraction f at the point of burn through into the silicon is known from the initial target manufacture and gives an ablation pressure of 28 Mbars. The mutual consistency of these three measurements is indicative that the implosion

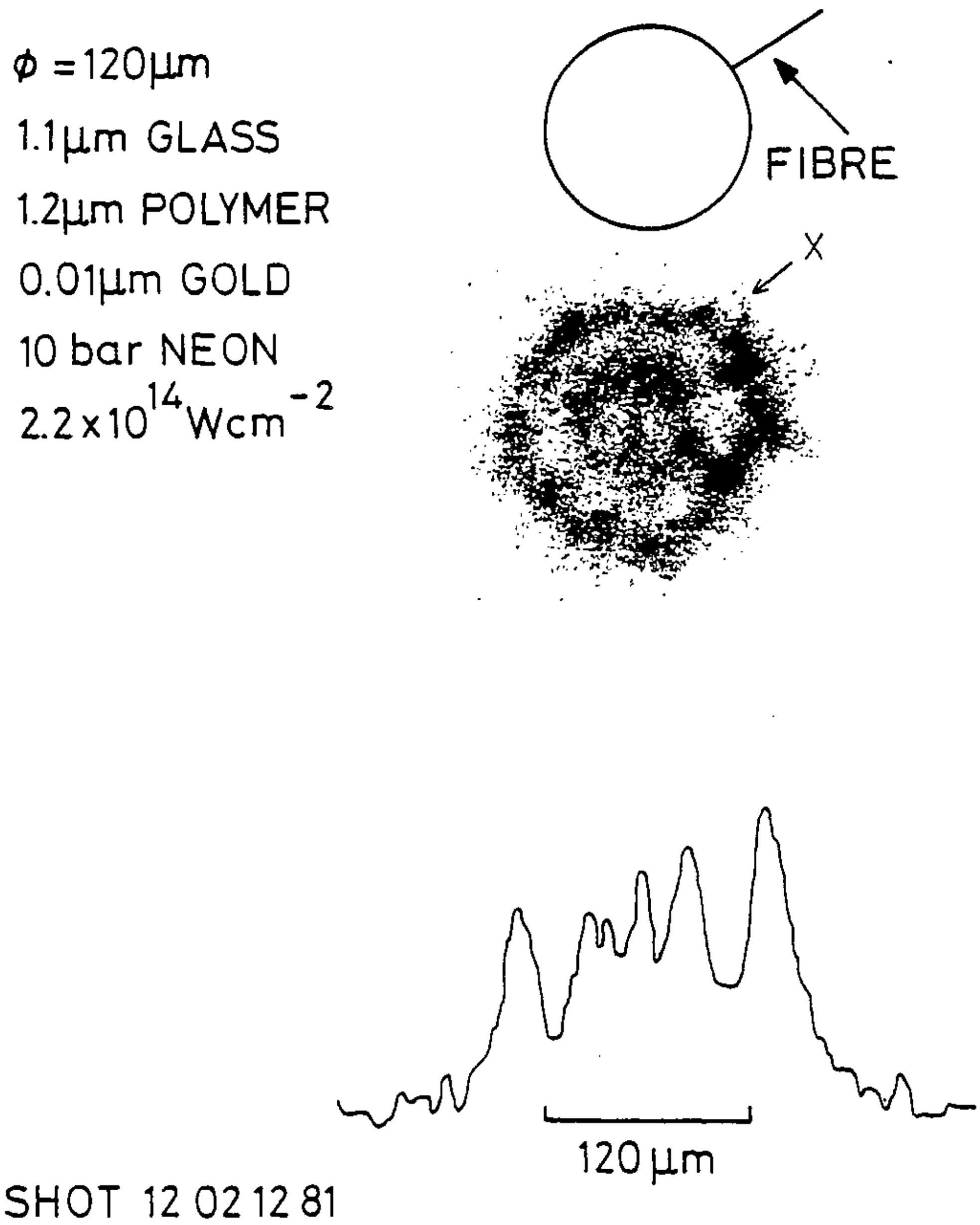

Fig. 4.7. X-ray pinhole image of imploding gold and plastic coated glass microballoon.

is being correctly described by a rocket model and that retardation of the shell due to spherical convergence is negligible in the shot. Equation (4.08) will overestimate the ablation pressure if the shell meets resistance on its way inwards. Equation (4.44) will under-estimate P_a for the same reason.

4.3.3 Space-resolved spectrometer

Using a miniature X-ray spectrometer[4.24] with a 10 μm space resolving slit enabled the spectrum of the hot core to be isolated. Fig. 4.8 shows the X-ray spectrum of a large aspect ratio (∿ 70) glass microballoon. The spectra of the core and the shell (ablation plasma) are superposed. The main resonance lines (e.g. Si XIII 1^1S_0 - 2^1P_1) in both spectra, are dominated by bright emission from the ablation plasma but the continuum stretching from 5.65 Å upwards is a feature of the core. The continuum slope can, from equation (4.43), yield a core temperature. The temperatures were typically 200 eV. Two important features are evident in Fig. 4.8. The first is the series of absorption features to the long wavelength side of the resonance lines, labelled A, B and C. A and C, which are to the long wavelength side of Helium resonance lines, correspond to absorption from Beryllium-like Silicon ions in the compressed glass pusher surrounding the core. Feature A, at 5.89 Å, can be identified as absorption due to transitions from 1s to 3p in ground state Beryllium-like Silicon ions. Feature C is due to 1s to 2p transitions in Beryllium-like Silicon, i.e. a Kα-like transition in absorption. Feature B is due to doubly excited Lithium-like ions undergoing a 1s to 2p transition.

The second feature of interest is the K absorption edge of the pusher material that has been shifted to a wavelength of 5.65 Å from its

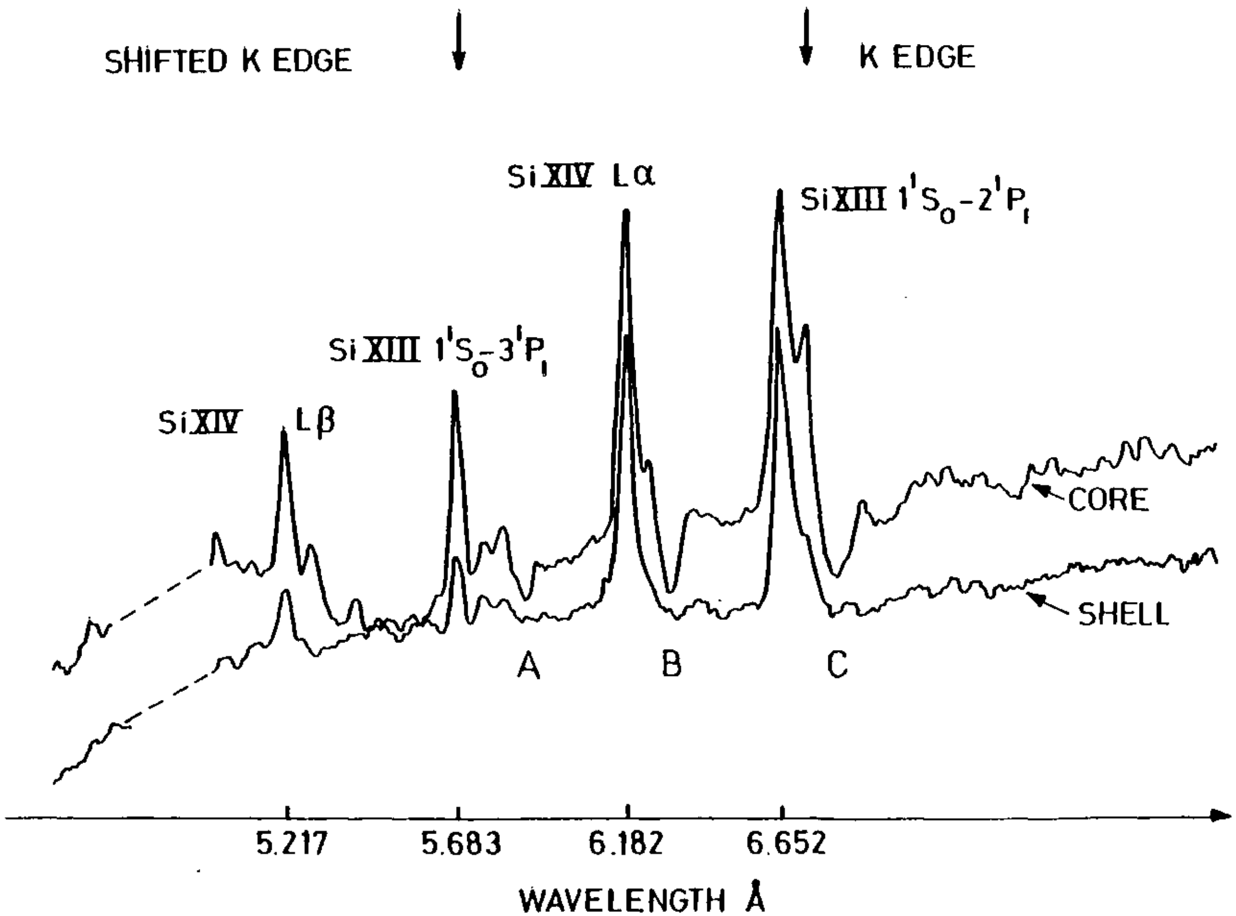

Fig. 4.8. Space-resolved X-ray spectrum of imploded glass microballoon showing spectra due to the core and shell separately. Features A, B and C in the core spectrum are due to absorption by the compressed glass pusher.

position in cold Silicon of 6.74 Å. The K edge has shifted due to ionisation reducing the screening of the nuclear charge, and thus increasing the energy required to ionise a K shell electron. Hartree-Fock calculations of the energies of the initial and final states after ionisation(4.25) enable the K edge position to be calculated as a function of ion stage. Debye shielding depresses the ionisation potential below that predicted by the Hartree-Fock calculations. The model of Stewart and Pyatt can be applied(4.26) to calculate the depression at high electron density (> 3 10^{23} cm^{-3}). Fig. 4.9 shows the results of applying ionisation potential depression to the edge shift predicted using the calculations of reference (4.25). The depression is density-dependent so curves for 1 and 3 g cm^{-3} are plotted. The K edge shown in Fig. 4.8 has been smeared out by the effects of time integration (over $\sim$ 100 picosecs as seen on the streaks) and the presence of different ionisation stages in the pusher. The edge stretches from 6.05 Å down to 5.65 Å where it is most sharply defined. Fig. 4.9 shows that for a density of 3 g cm^{-3} this range of edge positions corresponds to ion charges in the range 8 to 11. The smearing of the edge could be an indication of heat from the core raising the temperature of the pusher and hence ionising the silicon further. The absorption features A, B and C may be used to calculate the line density of the glass pusher at stagnation, however without time resolving the absorption the opacity can be underestimated leading to a poor measurement of ρR.

4.3.4 Nuclear diagnostics

Neutron yields from D-T filled microballoons were measured by Rutherford Laboratory staff using a scintillator detector. Yields were

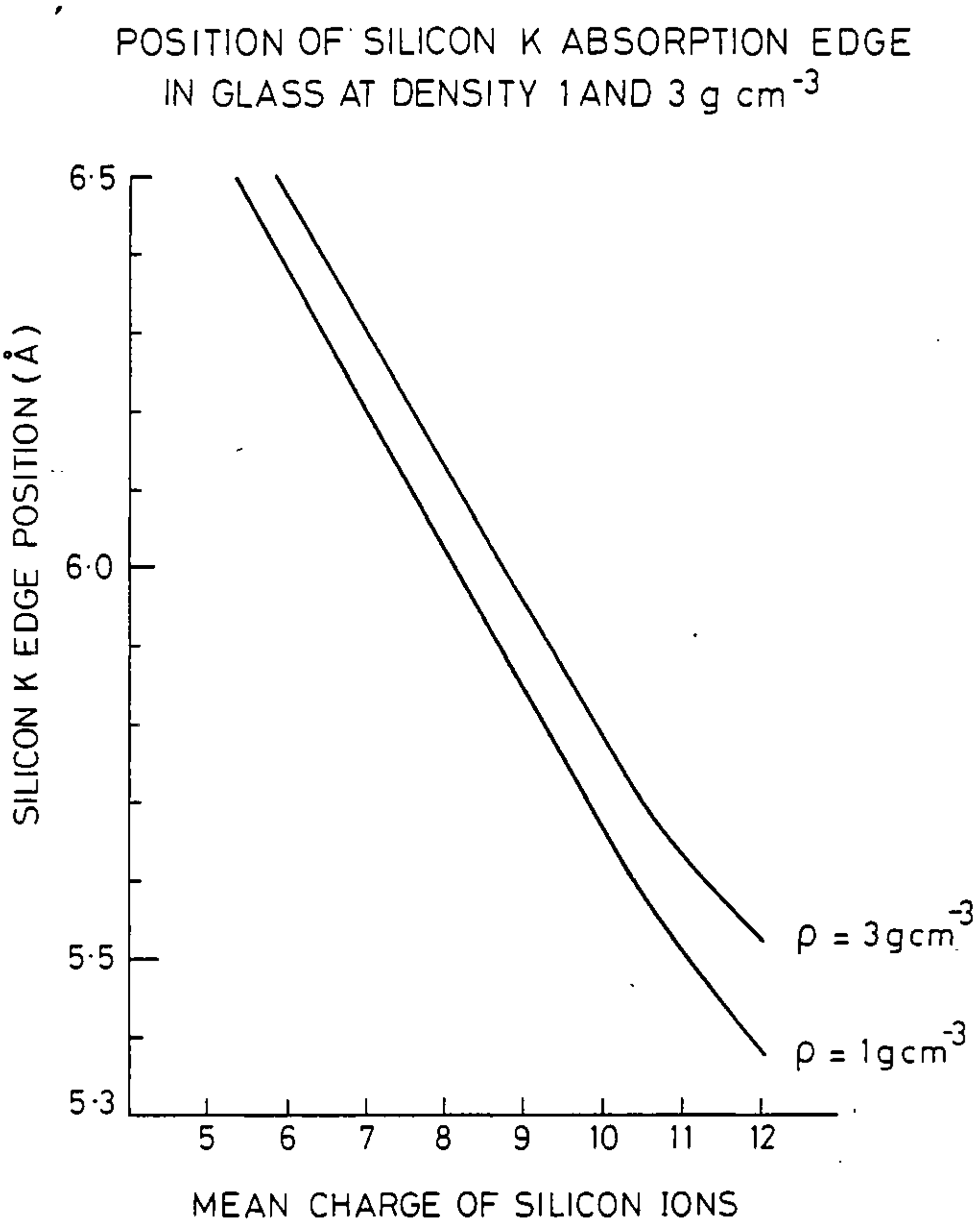

Fig. 4.9. K absorption edge position for SiO_2 as a function of mean Silicon ion charge.

in the range 10^4 - 10^5 neutrons, when observed. On some shots no neutrons were detected at all. The neutron yield can give a measure of the core ion temperature by estimating the confinement time from the ion sound speed and the expected compression ratio. The core ion temperatures deduced were than in the range 200 - 350 eV with an error of $\sim$ 20%(4.27).

Alpha particles were detected by workers from Bristol University using CR39 plastic(4.28). The α particles leave a trail of ionisation damage through the plastic which after etching with a caustic solution produces a visible track. The track shape and size provides quantitive information about the α particle energy. The α particle spectra observed from these experiments showed a peak in α particle energy down shifted to a few 100 keV.

The number of α particles detected was typically 10% of the neutron yield. The down shift in α energy plus reduction in number of α particles detected indicate that the glass pusher has a line density of the order of 3 10^{-3} g cm^{-2} (4.29), consistent with estimates based on the pinhole camera pictures. A more detailed discussion of the particle detection with CR39 plastic in this experiment is contained in the Ph.D. Thesis of A.P. Fews(4.30).

4.4 Results

4.4.1 Core temperatures

The core electron temperatures, deduced from X-ray continuum slopes and differentially filtered pinhole images, are shown in Table V.

The ρv^2 quoted in the final column is calculated from equations (4.03) and (4.04) using the ablation rate data of reference (4.08).

TABLE V

Shot	Shell Aspect Ratio $\frac{R}{\Delta R}$	Absorbed Irradiance (10^{14} W cm^{-2})	Fraction of of Shell Ablated (f)	Electron Temperature (eV)	Expected peak ρv^2 of Shell (Mbars)
05 101281	30.8	1.12	0.34	166 ± 20	3.1 10^3
03 101281	40.2	0.91	0.38	200 ± 50	3.8 10^3
06 231281	58.5	0.58	0.40	250 ± 20	3.8 10^3
06 111281	30.1	1.95	0.40	390 ± 80	5.6 10^3
10 161281	70.3	0.95	0.49	400 ± 100	7.6 10^3

The mean shell density is assumed to be twice the initial glass density; in the presence of preheat the shell density would be lower. The core electron temperature is seen to correlate with ρv^2 as indicated by equations (4.11) and (4.17), however the final electron temperatures achieved are very much lower than the predictions of the MEDUSA simulations in Table I. The temperatures are too low to allow seed gas spectroscopy to be used as a density diagnostic.

4.4.2 Compressed glass pusher density

The size of the opaque region, due to the high density compressed glass pusher, observable in the pinhole images enabled an estimate of the density of the compressed glass to be made. However due to the limit on the pinhole resolution and the uncertainty as to the amount of shell in the opaque region, the error in glass density is of the order of 50%. Table VI shows the densities and line densities observed using the unablated fraction of the shell mass[4.09] at peak ρv^2 as a measure of the mass in the opaque region.

The compressed shell densities in Table VI are all of the order of 1 - 2 g cm^{-3}. There is no obvious systematic dependence on irradiance or aspect ratio. If the shell were accelerating inward with a mean density of twice its initial density ρ_s (as assumed in equation (4.11)) the stagnation shell density would be higher than $2\rho_s$ due to the radial convergence of the shell. The low densities observed would imply that the shell is at low density ($\sim$ 1 g cm^{-3}) during the acceleration and hence the peak ρv^2 achieved is lower than predicted by a factor of the order of $1/5$. The implied reduction in shell density during the acceleration phase is possibly a consequence of radiation preheat.

TABLE VI

Shot	Shell Aspect Ratio	Diameter μm	Glass Thickness μm	Absorbed Irradiance 10^{14} W cm^{-2}	Ablated Fraction	Diameter of Opaque Region μm	Compressed Shell Density g cm^{-3}	Line Density g cm^{-2}	Core Diameter μm	Core Density g cm^{-3}
Error		5%	10%	20%		20%	50%	50%		
05 021281	43.6	139	1.6	0.64	0.34	51	2.4	6.1 10^{-3}		
03 101281	40.2	150	1.9	0.91	0.38	60	1.9	5.7 10^{-3}		
10 151281	59.9	127	1.06	1.65	0.51	41	1.9	3.9 10^{-3}		
08 161281	61.3	131.1	1.06	1.70	0.52	46	1.4	3.2 10^{-3}	14	6.9
10 161281	70.3	168.8	1.2	0.95	0.48	59	1.4	4 10^{-3}	20	5.0
11 161281	58.6	171.1	1.46	0.71	0.42	61	1.7	5.2 10^{-3}	23	3.5
01 171281	67.8	143.8	1.06	1.32	0.51	46	1.7	4 10^{-3}	19	3.7
14 171281	57.3	121.5	1.06	1.02	0.45	37	2.7	4.9 10^{-3}	16	2.1
06 171281	38.3	144.4	1.86	0.88	0.37	55	2.3	6.3 10^{-3}	16	3.5
09 171281	71.4	189.8	1.33	0.83	0.47	65	1.4	4.7 10^{-3}		
11 171281	77.2	185.2	1.2	0.78	0.48	65	1.2	4 10^{-3}		
14 171281	60.1	168.9	1.33	1.16	0.48	50	2.6	6.6 10^{-3}	27	2.1
02 181281	66.3	159.1	1.2	1.0	0.48	55	1.3	4.1 10^{-3}	17	7.0
08 181281	61.2	175	1.33	0.77	0.44	78	0.8	3.2 10^{-3}	18	7.7
03 211281	60.2	125	1.04	1.6	0.51	41	1.9	3.8 10^{-3}	14	6.5
05 221281	48.2	163	1.2(a)	1.05	0.43	63	1.7	5.3 10^{-3}	22	3.4
16 221281	37.7	110	0.93(b)	1.98	0.45	36	3.5	6.3 10^{-3}		
06 231281	58.5	156	1.33	0.38	0.40	64	1.2	3.7 10^{-3}	26	1.8
08 231281	75.3	161	1.06	1.17	0.52	49	1.7	4.3 10^{-3}	21	3.8
11 231281	78.3	146	0.93	1.37	0.54	46	1.5	3.3 10^{-3}	20	3.2
13 231281	79.7	148	0.93	1.16	0.53	44	1.8	4 10^{-3}	23	2.2
15 231281	43.5	134	1.54	1.67	0.46	42	3.2	6.7 10^{-3}		
16 231281	67.3	162	1.2	1.16	0.50	47	2.4	5.6 10^{-3}	23	2.9

(a) Coated with 1.2 μm Polystyrene
(b) Coated with 1.3 μm Polystyrene

4.4.3 Core density

The absence of hard X-ray emission from high Z seed gases in the core meant that the only method of density determination was from X-ray pinhole pictures. A core diameter was estimated by taking large magnification (x 8) pinhole pictures such as those shown in Fig. 4.10 and simply measuring the diameter of the central dark spot. The approximate core densities indicated are in the range 2 to 7 g cm^{-3}. It is possible that this measurement, which assumes no glass is in the emitting region, is an underestimate of the density.

4.5 Discussion

4.5.1 Preheat

The pusher densities presented in Table VI are consistent with preheat-induced decompression of the shell during the acceleration phase. Comparison of the compressed shell densities observed with those seen in the simulations of Table IV leads to the conclusion that preheat powers of the order of 10^{-5} J ng^{-1} $psec^{-1}$ would be sufficient to produce the decompression. The argument in section 4.2.4 has shown that radiation preheat powers of this magnitude are possible. The fast electron preheat predicted in section 4.2.4 is probably an overestimate due to the assumption of the conversion fraction η_{fe} being the same as for short pulse experiments[4.19]. However the radiative preheat alone is sufficient to provide a deposition of the order of 10^{-5} J ng^{-1} $psec^{-1}$ for the irradiation conditions of the experiment.

The estimate of the radiative preheat presented in section 4.2.4 is approximate and would greatly benefit from direct measurements of

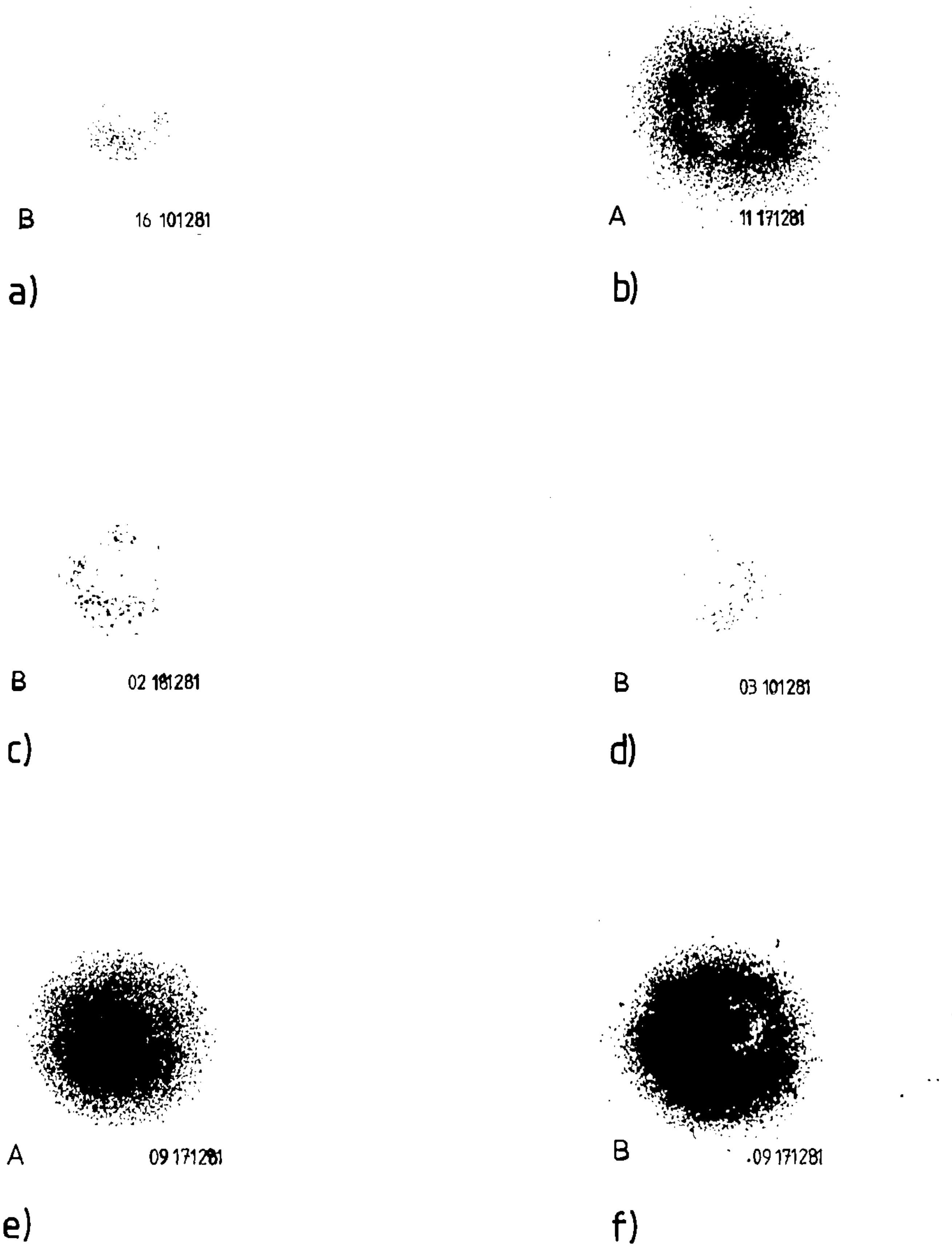

Fig. 4.10. Selection of pinhole images of X240 magnification. Pictures marked A and B refer to filters of Fig. 4.4.

soft X-ray spectra emitted from the targets used in the experiment. The Z scaling of soft X-ray intensity can be approximated from examination of comparisons of 1.06 μm irradiation of Parylene (C_8H_8) and Tungsten Glass (W_2O/P_2O_5) targets(4.14). Also 0.53 μm irradiation of Beryllium and Titanium targets presents some indication of Z scaling (4.15). For the same laser irradiance the difference in soft X-ray conversion is of the order of a factor of 3 in going from Glass (SiO_2) to Plastic targets. The reduction in X-ray intensity for plastic-coated glass targets will be offset slightly by the greater range of X-rays in the low density ($\sim$ 1 g cm^{-3}) low Z material(4.12), allowing X-rays to penetrate to the underlying glass and preheat it. Hence in Table VI the higher compressed shell density observed for Shot 16 221281 which was overcoated with a layer of plastic is not necessarily due to the low Z ablation plasma reducing radiative preheat.

4.5.2 Drive uniformity

Figures 4.10 and 4.11 are a selection of pinhole images showing the bright central cores and surrounding opaque regions characteristic of these implosions. Some of the images shown provide evidence that the ablative acceleration is not uniform for the whole shell. For example, Fig. 4.11a (Shot 05 021281) has an opaque region which is square in cross-section as well as a central bright core that has two components. The shape of the opaque region is consistent with enhanced drive pressure at the points where three neighbouring beams overlap. The initial intensity distribution on the target surface will have maxima at these three-beam-overlap points, under the focusing conditions used. Subsequently as the target is ablated, refraction in the low density plasma produced, coupled with thermal smoothing between

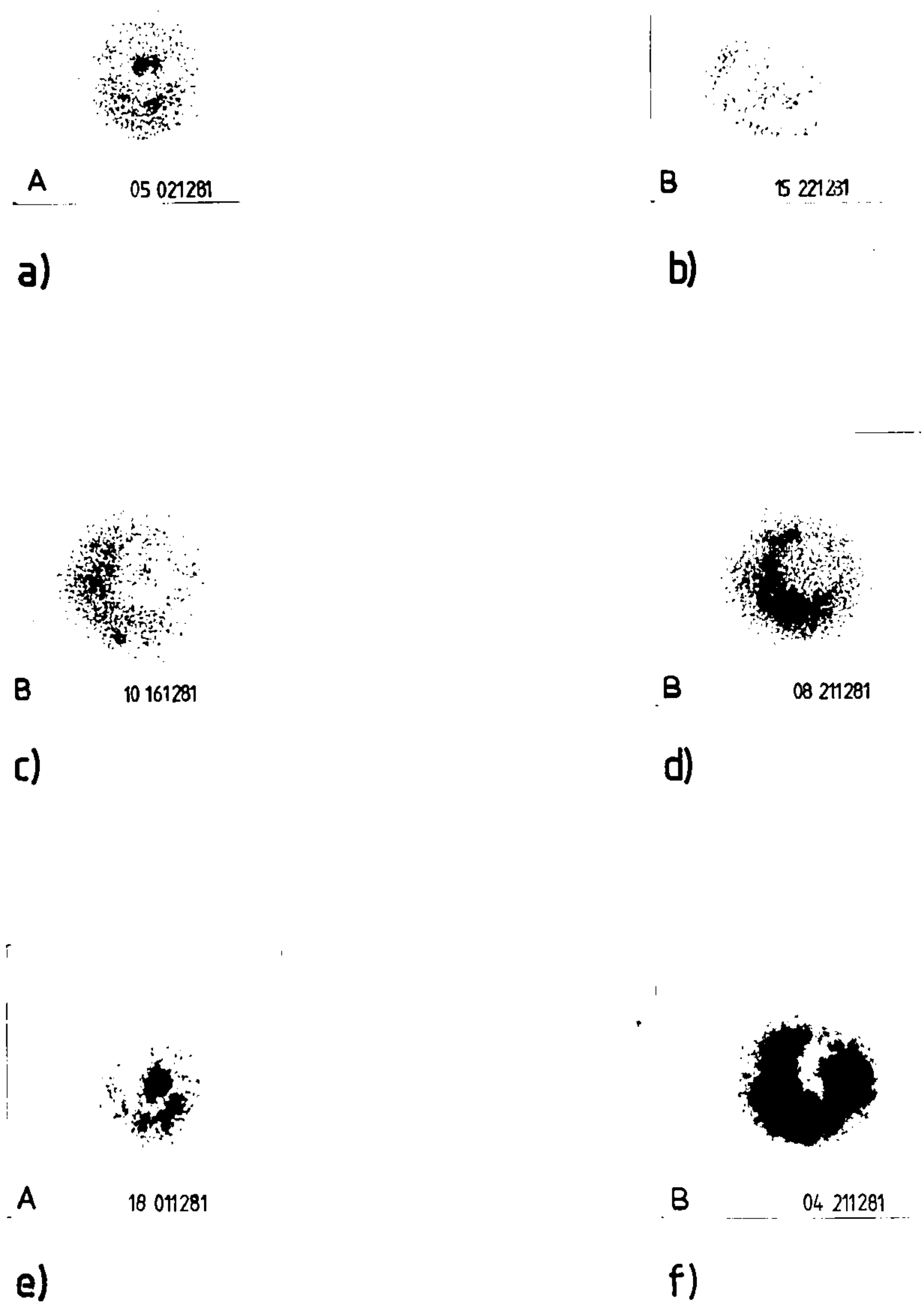

Fig. 4.11. A further selection of X-ray pinhole images.

critical density and the target surface(4.23) will create a more uniform ablation pressure distribution. However it is possible that the initial period of non-uniform irradiation can greatly affect the subsequent behaviour of the shell. For instance the initial pressure non-uniformity could alter the mass distribution in the shell, pushing mass sideways away from regions of higher ablation pressure (and hence stronger shock waves). The acceleration of the shell after the re-distribution of its mass will then not be uniform even if the ablation pressure becomes uniform.

The non-uniformity in the ablation pressure can be estimated from pinhole images such as Fig. 4.11a as of the order of 20%. This is not typical of the pinhole images produced. In general images such as Figs. 4.10a, 4.10b, 4.10c and 4.10d showed a much better uniformity.

Images such as Fig. 4.7 and Fig. 4.11b, which are of plastic and gold-coated targets, also allow a worst case estimate of pressure uniformity, using equation (4.08). The 30% difference in distance travelled by the shell before the Silicon starts emitting in Fig. 4.7 indicates imbalance in the acceleration of about 30% for this shot. Fig. 4.7 shows a minimum distance between gold and silicon emission at point X. The nearby region of Silicon emission is extended inwards indicating a longer period of glass ablation than elsewhere on the target. The opaque region representing the compressed glass is displaced away from point X indicating the effect of the higher pressure at that point. Gross non-uniformities in pressure due to faulty setting of relative beam energies produce pinhole images of this type. For example, Figs. 4.11c, 4.11d and 4.10c show opaque regions displaced relative to the centre of the balloon due to uneven illumination.

Non-uniformity in the pressure (or acceleration) will produce a poor spherical convergence and possibly account for the low core temperatures shown in Table V and indicated by neutron yields. The temperatures measured are much lower than those of the one-dimensional simulations shown in Table IV which included the effects of preheat. Therefore preheat, in reducing the ρv^2 of the pusher, will not reduce the core temperature to the values observed, but defects in the radial convergence could. The radial convergence will not have too great an effect on the compressed glass densities detailed in Table VI. The compression ratio of the shell material was typically less than three radially (e.g. a 150 μm diameter shell was compressed to fill a volume 50 μm in diameter). For the compression of the shell to be limited by pressure non-uniformity to a factor of three, the pressure would have to vary by greater than 50%. The worst cases observed showed pressure non-uniformity of 30% and these were due to irregularity in the relative incident beam energies. In general the drive pressure uniformity was better than 20% as demonstrated by the evident symmetry in Fig. 4.10d.

4.6 Conclusion

Results of the first ever experiments using 0.53 μm laser light to implode ablatively microshells have been presented. The low temperature of the cores produced precluded the use of X-ray seed gas density diagnosis. However the density of the compressed glass pusher was diagnosed as $\sim$ 2g cm^{-3}, from pinhole pictures. Comparison with one-dimensional simulations suggests that a preheat mechanism is causing the pusher to decompress during the implosion. The importance of radiative preheat was assessed and shown to be capable of providing sufficient energy deposition in the pusher to produce significant decompression.

Although observations were made of non-uniformity in the drive pressure (or acceleration non-uniformity due to re-distribution of the shell mass) it is not sufficient to explain the low pusher densities observed. However the drive non-uniformity can explain the low core temperatures observed,as an efficient conversion of pusher kinetic energy to compressed matter thermal energy would not then be achieved. The compressed core gas density was not diagnosable beyond estimates based on pinhole pictures. The non-uniformity in drive would also affect this density.

In order to obtain better uniformity in drive pressure a higher irradiance can be used so as to benefit from enhanced thermal smoothing [4.23]. However for a particular $I\lambda^2$ the degree of smoothing of illumination irregularities is a function of implosion time. The separation between critical density and the ablation front takes time to be set up. If the shell takes a long time to implode then the smoothing has a longer time to take effect. It can be shown[4.31] that for a particular target and laser wavelength the degree of smoothing is almost independent of irradiance. This fact arises due to the almost linear dependence of ablation pressure on irradiance[4.09]. The implosion time is then approximately proportional to $I^{-\frac{1}{2}}$. The smoothing efficiency has been measured to scale as approximately $I^{0.67}$ [4.23] indicating that the product of smoothing effectiveness with implosion time is almost constant with irradiance.

The possibility exists that planar measurements of thermal smoothing may not be applicable to spherical implosions due to the initial non-uniformity in illumination producing an irreversible distortion of the converging shell. Fig. 4.11f shows a microballoon imploded using six beams defocused only 2.25 target radii beyond the centre of each beam. The figure shows an opaque region with three spikes corresponding to concentrations of shell mass. The line density along these spikes (only two are easily visible in the figure) could be significantly greater than at other points in the opaque region if the density is assumed to be reasonably constant. The re-distribution of shell mass evidenced in this picture could happen on a smaller scale for the non-uniformities associated with the six-beam geometry. Such an effect would not occur so readily in the planar geometry experiments due to the lack of curvature of the target.

In summary it is felt that, although X-ray preheat of the pusher has been shown to be capable of reducing the compressed glass density, the final temperature and density achieved in the core of these implosions is probably a strong function of illumination uniformity.

CHAPTER 5

HIGH INTENSITY IMPLOSIONS

5.0 Abstract

Experiments using short pulse ($\sim$ 100 psec) $\lambda = 0.53$ μm irradiation to implode microshells are described. Density and temperature diagnosis of the core is achieved using Argon seed gas spectroscopy. A comparison experiment using 1.054 μm radiation is described. The use of Chlorine-doped plastic microshells in high density implosions is proposed and demonstrated in low density exploding pusher implosions.

5.1 Introduction

As an extension to the work described in the previous chapter it was attempted to perform high intensity 0.53 μm implosions. These implosions were of sufficient spherical uniformity that core temperatures over 500 eV were obtained, enabling core density diagnosis using Argon-doped fill gases. The experiment was performed at KMS Fusion Inc. using their spherically symmetric TBIS illumination system. Unfortunately due to limitations caused by damage thresholds in the laser system, it was not possible to do a long pulse ($\sim$ ½ nsec) experiment at the intensities required for implosion. Therefore the experiment was done using a short pulse of 100 picoseconds duration at incident irradiances of about 10^{15} W cm^{-2}. These implosions were therefore dominated by fast electrons and were hence 'quasi-exploding-pusher' implosions.

The second experiment described was performed at Rutherford Appleton Laboratory using similar incident irradiances as in the first experiment. However these implosions had a higher $I\lambda^2$ due to the use of 1.054 μm light. A comparison is possible between the results of this experiment and some of the results of the KMS experiment.

The final part of this chapter will deal with the use of plastic microballoons in high density implosions. For the line densities of the compressed pusher expected in truly ablative implosions a glass shell will be attenuating to K shell emission from an Argon seed gas. A plastic shell will have much lower attenuation to emission from a high Z dopant such as Argon (Z = 18) or Chlorine (Z = 17). High intensity λ = 1.054 μm implosions were carried out with polystyrene shells ($C_6H_5\ CH\ CH_2$) filled with Freon 12, dichlorodifluoromethane ($CCl_2\ F_2$). The Chlorine in the Freon gas fill produced X-ray spectra enabling temperature and density determination.

5.2 High Intensity λ = 0.53 μm Implosions (KMS Fusion Inc.)

Glass microshells of 70 - 150 μm diameter were irradiated with up to 10^{15} W cm^{-2} in 100 - 200 picoseconds. The experiment was carried out at KMS Fusion Inc. using the Triple Bounce Illumination System (TBIS) to provide spherically symmetric irradiation. Fig. 5.1 shows the geometry of the TBIS system, two hemispheric mirrors focus light onto the target after it has experienced three reflections. The illumination is then incident on the target from almost 4π steradians. A narrow equatorial gap between the mirrors allows diagnostic access to the target, the absence of illumination in this equatorial region is prevented by defocusing the mirrors slightly so that rays overlap on the equator.

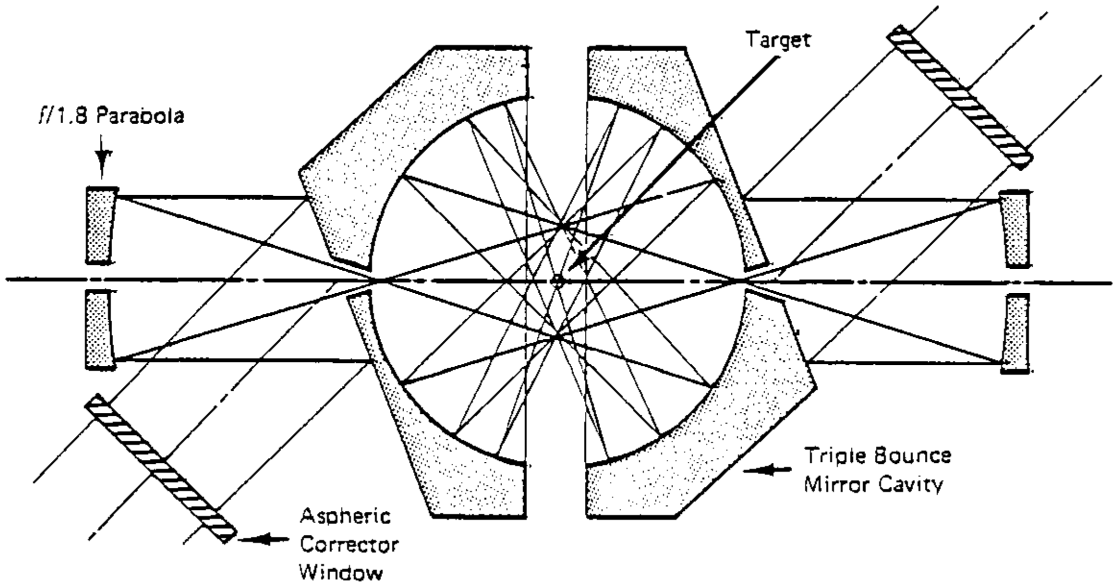

Fig. 5.1. Plan of the KMS Triple Bounce Illumination System (TBIS). Reprinted from the 1980 KMS Fusion Inc. Annual Report.

5.2.1 Targets imploded

Three different classes of target were imploded and found to emit seed gas spectra.

(i) Small (70 μm diameter), thin-walled (0.9 μm) glass microballoons filled with 0.4 atmospheres of Argon.

(ii) Larger (∿ 110 μm diameter) glass microballoons with wall thicknesses between 0.9 μm and 1.5 μm filled with 2 atmospheres of Argon.

(iii) Microballoons as in (ii) but with an extra fill of Deuterium gas (D_2) of the order of 100 atmospheres.

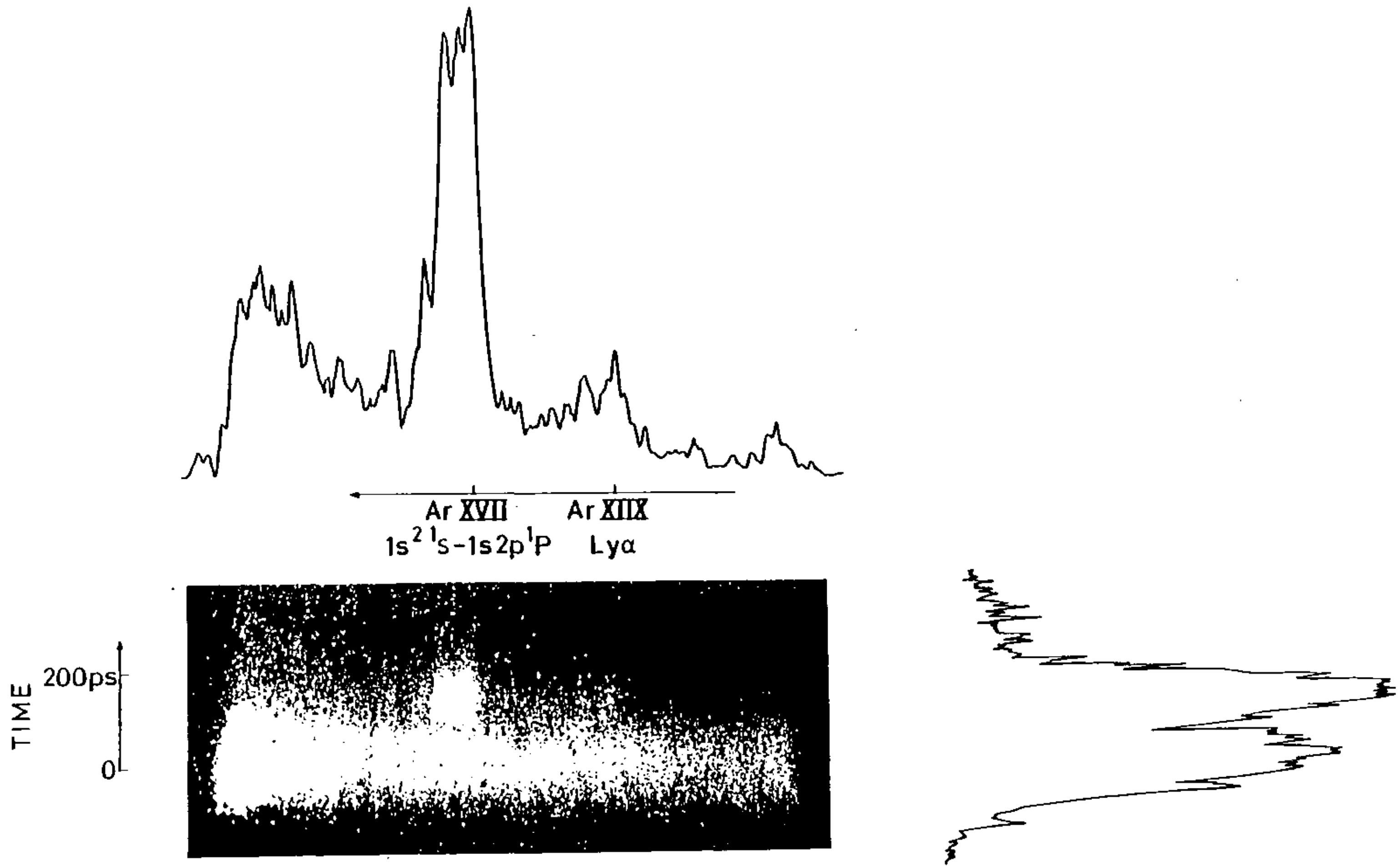

Fig. 5.2. Time-resolved Argon spectrum (Shot 5520).

5.2.2 Diagnostics

X-ray diagnostics employed in this experiment included time-resolved and time-integrated spectroscopy. Time-resolved spectra were recorded using a flat RbAP crystal (Rubidium acid phthalate, 2d = 26.12 Å) to diffract X-rays onto the photo-cathode of an X-ray streak camera (on loan from Rutherford Appleton Laboratory). A flat crystal was used, as a curved crystal (described in Chapter 3) was not available. The spectra observed were therefore limited in time resolution due to the low sensitivity of the flat crystal/streak camera combination. Fig. 5.2 is a typical streaked Argon spectrum. The time resolution is 40 picoseconds, sufficient to show the delay between the bright continuum, corresponding to the laser ablating the shell, and the appearance of Argon lines. The Argon $1s^2\ ^1S_0$ - $1s2p\ ^1P_1$ (Heα) and Lyα are seen on this streak.

Time-integrated spectra were observed using a minispectrometer[5.01] containing a PET crystal (Pentaerythritol, 2d = 8.74 Å). The spectrometer was positioned with its entrance slit 6 cm from the target instead of its usual position 5 mm from the target. The large separation between spectrometer and target (necessary due to the TBIS geometry) meant that space-resolved spectroscopy was not possible. However the larger separation meant higher dispersion spectra, at the expense of reduced spectral range. A typical Argon spectrum is shown in Fig. 5.3.

5.2.3 Electron density determination

The electron number density n_e in the compressed core was calculated from the Stark-broadened line profiles of Argon Heβ and Heγ. The profiles were taken from time-integrated spectra such as that of

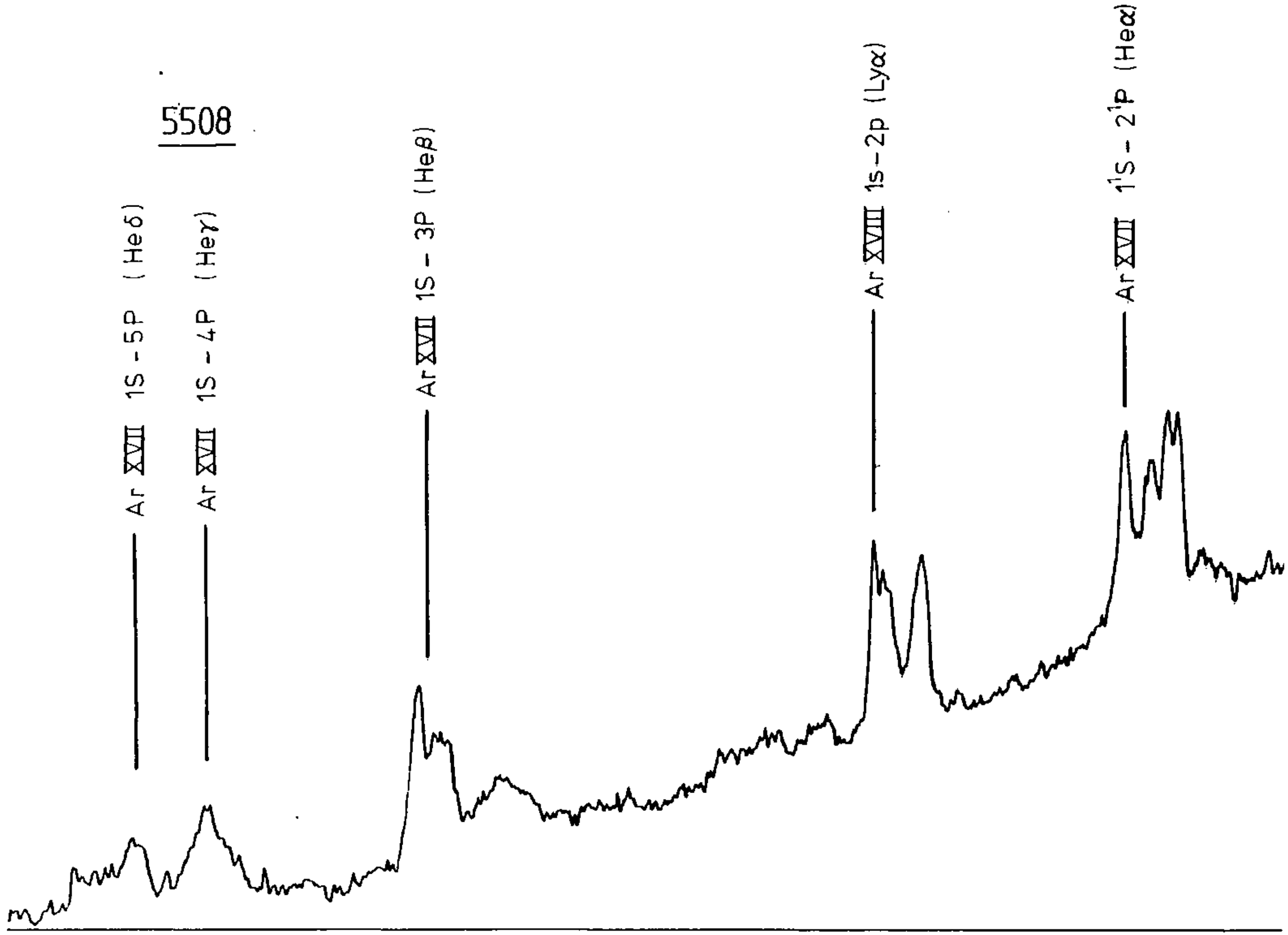

Fig. 5.3. Argon core spectrum from Shot 5508.

Fig. 5.3 and digitised. The line profiles were then fitted in n_e, $n_1 \ell$ parameter space to the optically-thin Helium-like profiles of R. W. Lee with LTE opacity broadening[5.02]. Here $n_1 \ell$ is the line density of Helium-like Argon ions (Ar XVII) in the ground state contributing to the opacity broadening of the line. Electron densities were found to be in the range 10^{23} cm^{-3} to 3 10^{23} cm^{-3}, equivalent to mass densities between 0.3 and 1 g cm^{-3}.

5.2.4 Electron temperature determination

The ratio of Helium-like to Hydrogen-like Argon lines served as a diagnostic of electron temperature in the compressed core. The relative intensities of the different lines were calculated using the population calculations of R. W. Lee. The collisional and radiative rate equations are solved for a homogeneous plasma and the optically thin line ratios calculated. The collisional excitation rates were updated to agree with the calculations of Pradhan et al.[5.03][5.04]. The results of the calculations are summarised in Fig. 5.4 where various line ratios are plotted as a function of electron temperature for two different electron number densities. The ratio used for temperature diagnosis in this experiment was that of the Lyα to Heγ. The ratio is seen in Fig. 5.4 to be rapidly varying with temperature in the range 500 eV - 900 eV and insensitive to electron density changes.

5.2.5 Results

The electron densities and electron temperatures observed are summarised in Table I. The specific absorbed energy quoted is obtained by dividing the absorbed energy, as measured by an array of four plasma calorimeters, by the initial mass of the target. The error quoted for

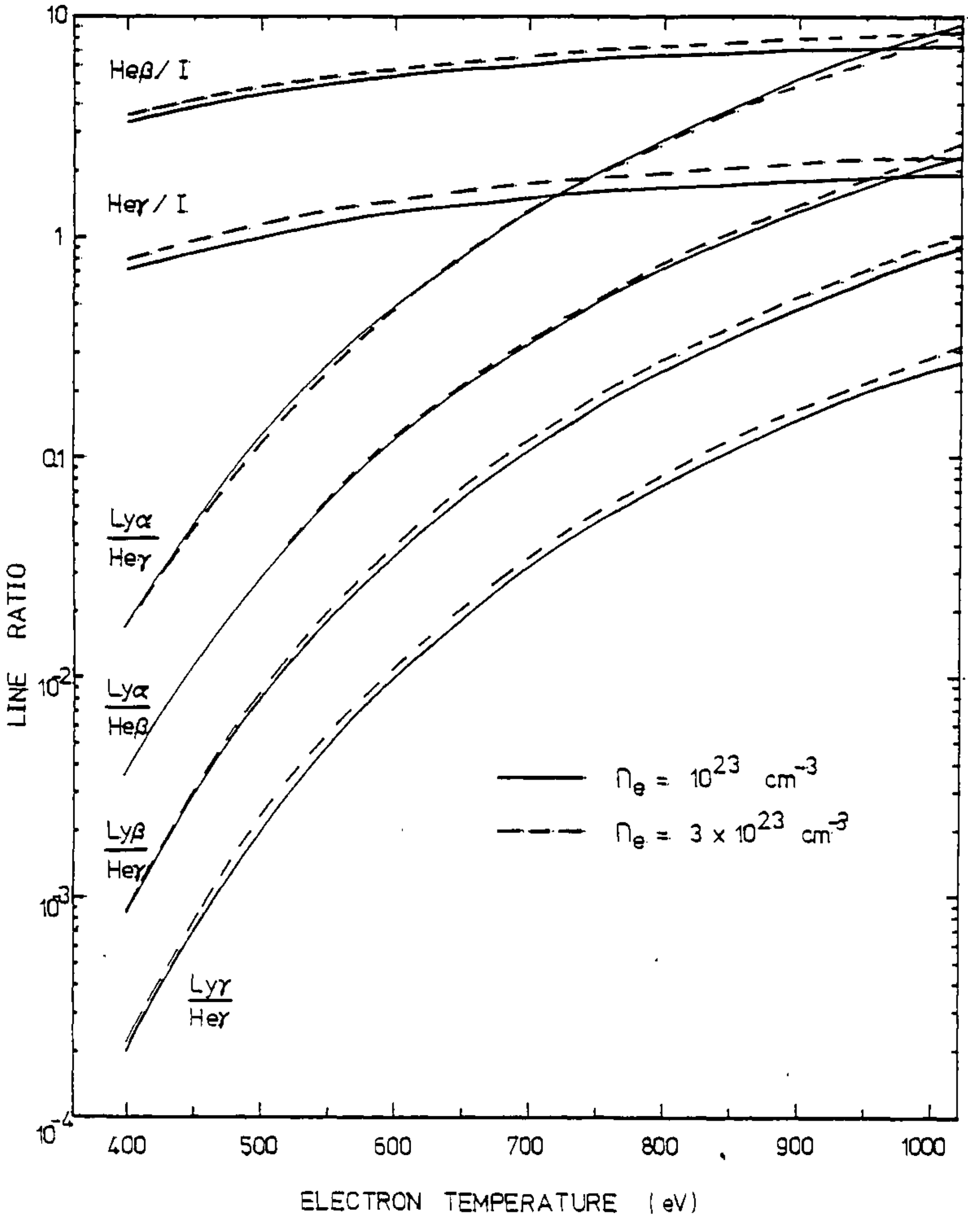

Fig. 5.4. Ratios of the intensities of the main X-ray lines of Hydrogen-like and Helium-like Argon, as a function of electron temperature for two different electron densities. The intercombination line $1s^2\ {}^1S_0$ - $1s2p\ {}^3P$ is referred to as 'I'.

TABLE I

Shot	Initial Diameter (μm)	Glass Shell Thickness (μm)	Argon Gas Fill Pressure (Atm)	D_2 Gas Fill Pressure (Atm)	Absorbed Irradiance (W cm^{-2})	Specific Absorbed Energy (J/ng)	Compressed Argon Electron Density (cm^{-3})	Compressed Argon Electron Temperature (eV)	Brightness of Spectrum (Arbitrary Units)
5507	70	0.9	0.4	None	$6.8\ 10^{14}$	0.29	$(5\pm2)\ 10^{23}$	800 ± 15	7.0
5508	106	0.9	2.0	None	$4.5\ 10^{14}$	0.18	$(2.4\pm.3)\ 10^{23}$	730 ± 15	7.1
5509	103	1.2	2.0	None	$3.7\ 10^{14}$	0.12	$(3.0\pm.5)\ 10^{23}$	730 ± 15	2.4
5518	115	1.0	2.0	115	$3.3\ 10^{14}$	0.13	$< 10^{23}$	640 ± 20	8.3
5519	117	1.2	2.0	115	$2.9\ 10^{14}$	0.09	$(2.4\pm.5)\ 10^{23}$	640 ± 20	3.8
5520*	148	1.0	2.0	125	$1.6\ 10^{14}$	0.12	$(1.0\pm.2)\ 10^{23}$	610 ± 20	8.9
5521	141	1.2	2.0	130	$2.5\ 10^{14}$	0.08	Weak lines	$\lesssim 550$	3.5
5522	102	1.1	2.0	None	$4.0\ 10^{14}$	0.14	$(2.8\pm.6)\ 10^{23}$	660 ± 20	2.6
5523	107	1.4	2.0	88	$2.9\ 10^{14}$	0.08	Weak lines	600 ± 100	1.0

* 200 picosecond laser pulse duration.

the electron temperature is from the uncertainty in measuring the line ratios. The final column in Table I gives a qualitative measure of the brightness of the time-integrated spectra obtained. The brightness quoted is proportional to the intensity of the group of lines near the Argon Heα that includes the $1s^2\ {}^1S_0$ - $1s2p\ {}^1P_1$ resonance line and $1s^2\ {}^1S_0$ - $1s2p\ {}^3P$ intercombination line.

The brightness of the spectra is a function of the shell thickness. The electron temperature is also a function of the shell thickness but varying the shell thickness also affects the specific absorbed energy. The final temperature in these quasi-exploding pusher implosions should be linearly dependent on the absorbed specific energy(5.05). Fig. 5.5 shows the electron temperatures plotted as a function of specific absorbed energy for the shots in Table I. The target type in the key of Fig. 5.5 refers to the description in section 5.2.1.

There is an obvious correlation between temperature and specific absorbed energy. Comparing shot 5508 with 5509 (in Table I) which have similar electron temperatures and densities, the brightness is seen to be lower by a factor of three in the latter shot. The target diameter and Argon fill density was similar for these two shots but the shell thickness was greater for 5509. A possible explanation for the reduced brightness in the spectrum of shot 5509 is that the higher compressed shell ρR, expected due to the greater initial shell thickness, is attenuating the Argon emission. The transmission of glass (SiO_2) as a function of pusher ρR and temperature(5.06) is plotted in Fig. 5.6 for an X-ray wavelength of 3.96 Å (Argon Heα). The possibly lower pusher temperature associated with the thicker shell of 5509 coupled with a higher expected ρR, indicates that the glass transmission could be significantly different between shot 5508 and 5509. The region of

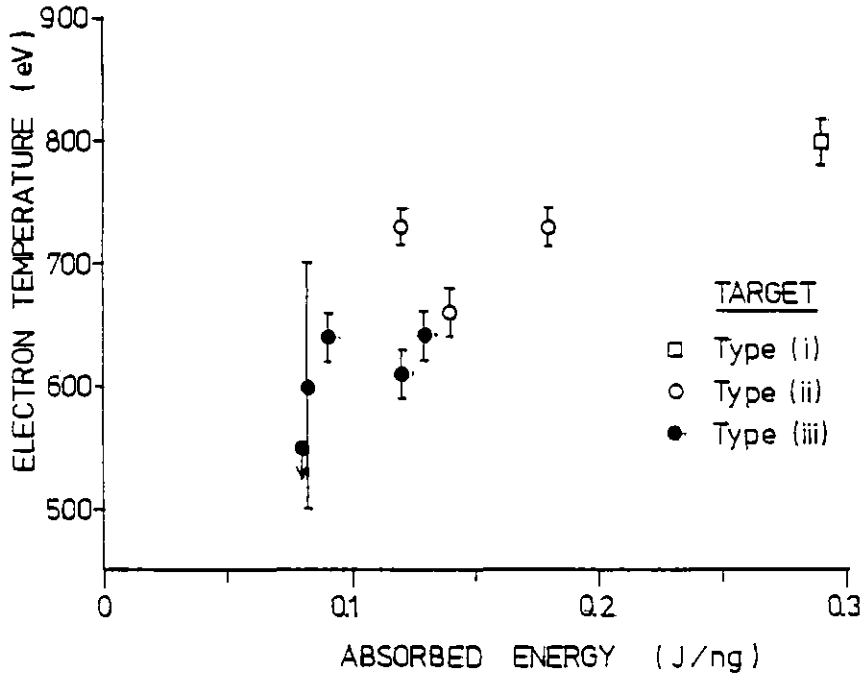

Fig. 5.5. Measured core electron temperatures from Table I plotted against specific absorbed energy. The target types are described in section 5.2.1.

rapid variation of shell transmission with ρR begins near a ρR of $2\ 10^{-3}$ g cm^{-2}. Hence in the ablative implosions described in Chapter 4, any Argon lines excited in the core would be severely attenuated by the high line density of the pusher ($3 - 6\ 10^{-3}$ g cm^{-2}).

Shot 5523, which was of similar diameter to 5508 and 5509 but had a wall thickness of 1.4 μm, produced very weak spectra (see Table I). The core temperature in this implosion was possibly lower but the weakness of the Argon lines observed meant that the electron temperature determination was less accurate.

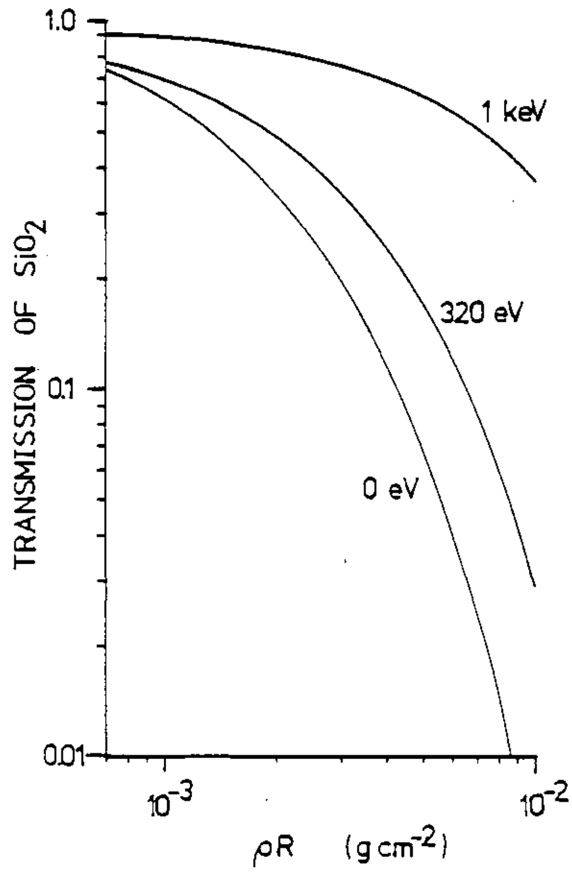

Fig. 5.6. Transmission of glass pusher as a function of line density for three different glass temperatures (at 3.96 Å).

The electron temperatures observed with D_2-filled targets (Type (iii) as described in section 5.2.1) were lower than for the pure Argon-filled targets but the specific absorbed energies were also lower (see Fig. 5.5).

5.3 High Intensity λ = 1.054 μm Implosions (Rutherford Appleton Lab.)

Following on from the experiment described in section 5.2 similar microballoons were imploded at Rutherford Appleton Laboratory using six-beam illumination of wavelength 1.054 μm. Pulses of 50 J (summed over six beams) of 100 picoseconds duration irradiated two types of target.

(i) Low pressure Argon-filled glass microballoons of $\sim$ 70 μm diameter and shell thickness between 0.5 and 0.8 μm.

(ii) High pressure Argon-filled glass microballoons of $\sim$ 100 μm diameter and shell thickness between 1.3 and 1.7 μm.

The two types of target are very similar to types (i) and (ii) defined in section 5.2.1 for the KMS experiment.

5.3.1 Electron temperature and density determination

The determination of the conditions in the compressed Argon was achieved using the methods described in section 5.2. Electron temperatures deduced from the ratio of Ar Lyα to Ar Heγ were about 840 eV for the type (i) targets and about 660 eV for the type (ii) targets. Electron number densities calculated from matching Stark-broadened line profiles were about 10^{23} cm^{-3} for all targets.

Fig. 5.7 is a spectrum produced by a type (i) (small, thin-walled) target. The absolute wavelength of the Argon X-ray lines has been determined by using the K absorption edges of Potassium (3.437 Å) and Chlorine (4.397 Å) as fiducials. A thin (1.5 μm) layer of Potassium Chloride (KCl) was placed over the spectrometer slit in order to produce the absorption edges seen in Fig. 5.7. The proximity of the Potassium edge to the Ar Heβ line (3.366 Å) allowed a measurement of any shift of the line due to density effects. For the shot illustrated (11 160682) the Heβ was found to have shifted by 2 ± 0.7 mÅ towards lower energy (i.e. the line was red shifted).

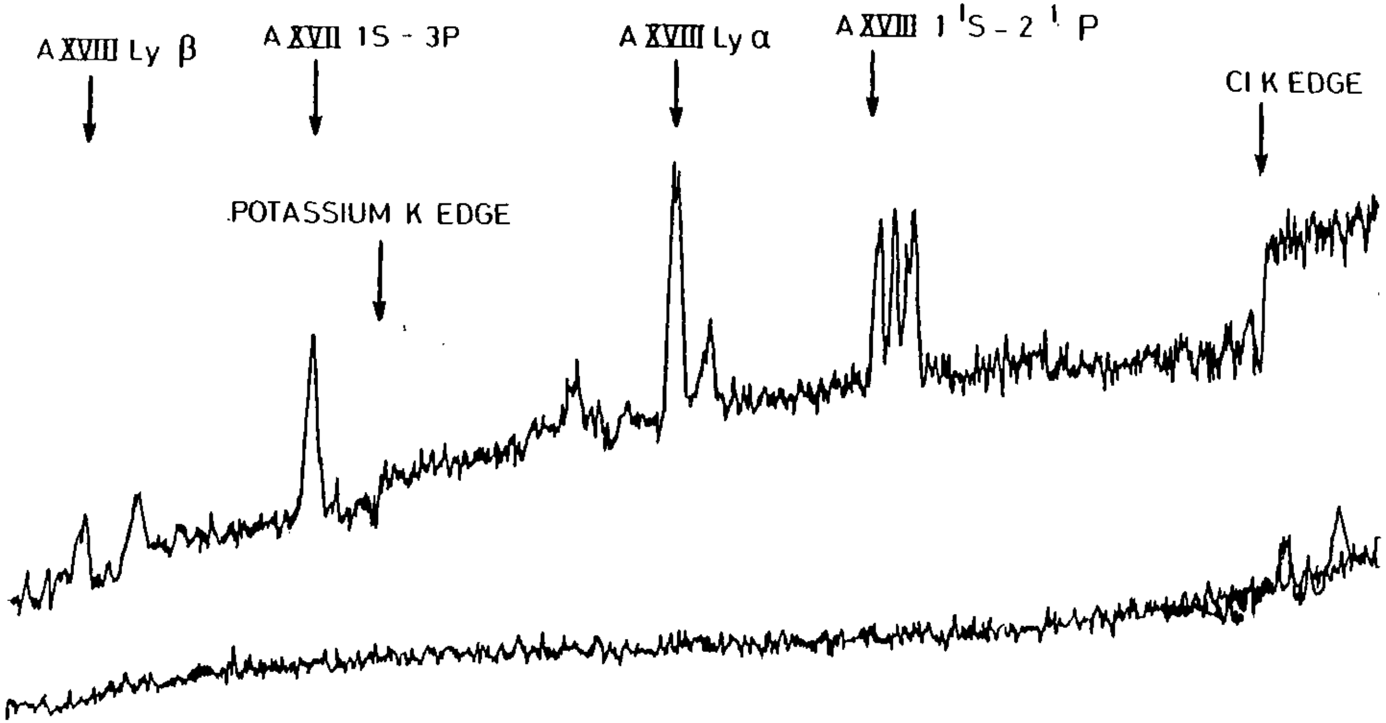

ARGON EMISSION SPECTRUM THROUGH A COLD KCl ABSORBER
TO FIX THE ABSOLUTE WAVELENGTH
SHOT 11160682

Fig. 5.7. Argon core spectrum from 73 μm diameter glass microballoon.

5.3.2 Results

The results of the temperature and density determinations are tabulated in Table II. The small (∿ 70 μm diameter) targets all had electron temperatures of about 840 eV. The irradiances and specific absorbed energies for the small type (i) targets did not vary much resulting in little spread in temperature or density.

The larger (type (ii)) targets, described in the last three rows of Table II, showed much the same densities as the other targets but the temperatures were much lower. The lower temperature is associated with the reduced specific absorbed energy. The brightness of the spectrum is defined as in section 5.2 and the units are normalised to be the same as in Table I. The effect of increased glass opacity for thicker shells is possibly an explanation for the reduced brightness of shots 09 090682 and 09 180682 (with shells 1.7 μm thick) compared with shot 03 170682 (which had a 1.3 μm thick shell) despite having similar densities and temperatures.

5.3.3 Comparison with KMS experiment

The type (ii) target shots can be compared directly with some of the KMS experiment results shown in Table I. For example, shot 5522 is of similar size to shot 03 170682 and has a similar specific absorbed energy and compressed electron temperature. However shot 5522 produced a higher density than the shots shown in Table II.

The type (i) target shots of Table II can be compared with shot 5507 from the KMS experiment. Again higher densities were produced in the KMS experiment for the same target type and irradiance conditions but different laser wavelength.

The higher $I\lambda^2$ of the 1.054 μm experiment would lead to a higher

TABLE II

Shot	Initial Diameter (μm)	Glass Shell Thickness (μm)	Argon Gas Fill Pressure (Atm)	Absorbed Irradiance (W cm^{-2})	Specific Absorbed Energy (J/ng)	Compressed Argon Electron Density (cm^{-3})	Compressed Argon Electron Temperature (eV)	Brightness of Spectrum (Arbitrary Units)
05 110682	70	0.6	0.25	8.3 10^{14}	0.53	$(1.1 \pm .2)\ 10^{23}$	850 ± 20	-
07 110682	71	0.5	0.25	7.9 10^{14}	0.61	$(0.8 \pm 0.3) 10^{23}$	840 ± 20	-
03 150682	69	0.8	0.25	7.4 10^{14}	0.36	$(1.0 \pm .15) 10^{23}$	840 ± 20	-
11 160682	73	0.8	0.25	6.7 10^{14}	0.32	$(1.1 \pm .2)\ 10^{23}$	840 ± 20	-
09 090682	102	1.7	2.0	3.2 10^{14}	0.07	$(1.1 \pm .2)\ 10^{23}$	630 ± 20	4.0
03 170682	99	1.3	2.0	3.3 10^{14}	0.10	$(1.3 \pm .2)\ 10^{23}$	680 ± 20	8.0
09 180682	89	1.7	2.0	4.0 10^{14}	0.09	$(1.8 \pm .6)\ 10^{23}$	685 ± 20	2.9

fast electron temperature and hence a greater preheating of the fill gas. The reduced density observed in the Rutherford Laboratory experiment is consistent with increased preheat compared with the KMS experiment.

5.4 Implosion of Polystyrene Microshells

The attenuation of Argon lines by the increased opacity of thick glass shells has been mentioned in previous sections as a possible explanation for the observation of reduced Argon core emission from thick-walled balloons. For high ρR implosions (i.e. above 6 10^{-3} g cm^{-2}) plastic-walled microballoons will have lower opacity than glass, at photon energies above the Silicon K edge due to the low Z of Carbon compared with the Silicon in glass microballoons.

Polystyrene shells (C_6 H_5 CH CH_2) are available in a variety of sizes and wall thicknesses. The most massive element in the shell is Carbon which will be K ionised by quite modest temperatures ($\sim$ 100 eV). The X-ray emission of a high Z material such as Argon (Z = 18) would be transmitted even by large line densities of pusher. For an unheated polystyrene shell the transmission for X-rays of 4.19 Å wavelength is 42%, for a ρR of 10^{-2} g cm^{-2}. Figure 5.6 which graphs the transmission of SiO_2 at a wavelength of 3.96 Å, shows that even at a temperature of 320 eV, glass only transmits 3% for a ρR of 10^{-2} g cm^{-2}. Once the carbon in the polystyrene shell becomes K ionised the transmission will be much higher than for the unheated case.

Choice of a suitable gas for filling the plastic balloons is restricted by the high permeability of the shell to small molecule gases such as Argon. Freon 12 (C Cl_2 F_2) was chosen as a fill gas as it could be diffused into the targets over a period of a few hours and

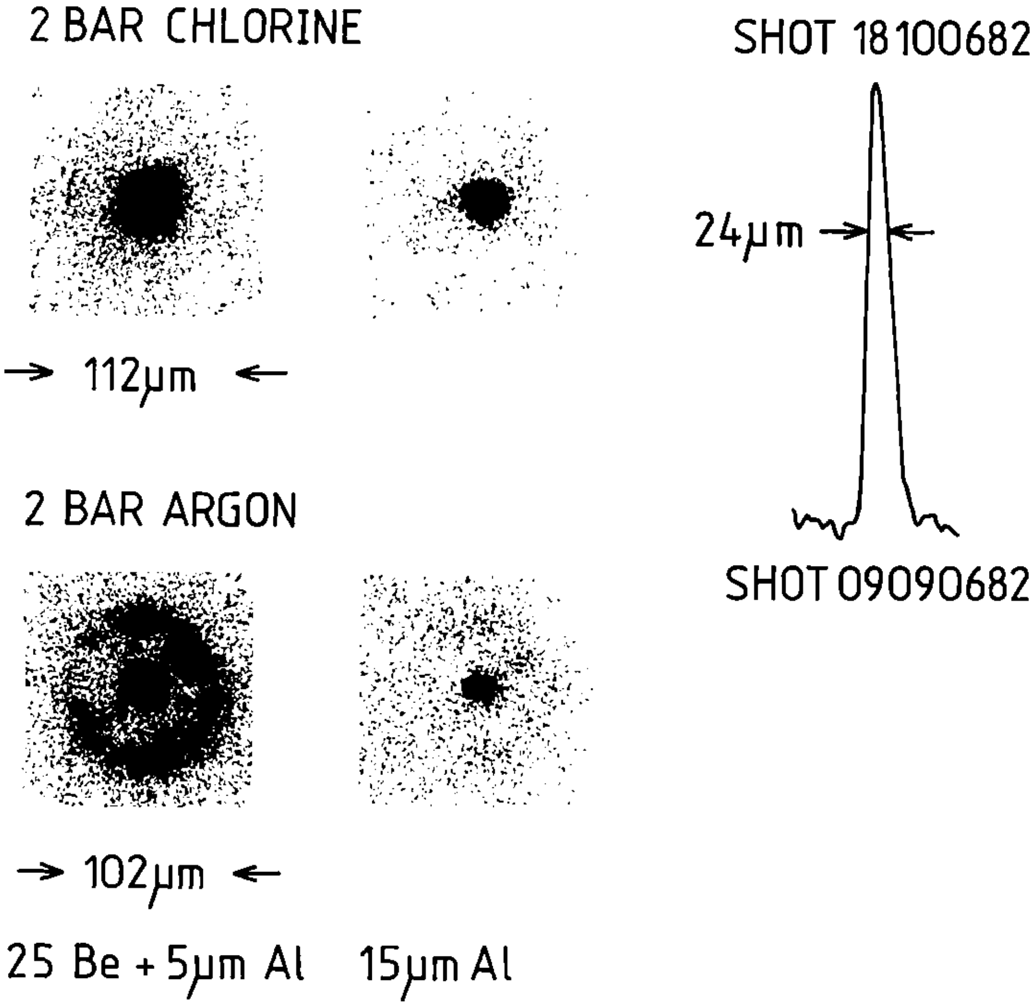

Fig. 5.8. Comparison of X-ray pinhole images of imploded polystyrene and glass microshells.

would be retained by the balloon for a similar length of time. The Chlorine (Z = 17) in the Freon was a suitable diagnostic element due to the high photon energy of its characteristic X-rays, only slightly longer wavelength than Argon lines.

Freon-filled plastic shells were imploded as part of the experiment described in section 5.3.

5.4.1 Experiment

Three plastic microshells were imploded with absorbed specific energies of the order of 0.1 J/ng. The targets had plastic wall thicknesses of the order of 3 μm, and diameters of the order of 110 μm. Although the wall thicknesses were greater than for glass microballoons, the density of plastic is 1.06 g cm^{-3} compared with SiO_2 which has a density of 2.6 g cm^{-3}. Hence a 2.6 μm plastic shell will accelerate at a similar rate to a 1 μm glass shell.

The targets contained one atmosphere of Freon 12 which contains a number density of Chlorine equivalent to two atmospheres if the Freon molecules were broken up. Hence the label on Fig. 5.8 refers to 2 bar of Chlorine. Fig. 5.8 shows two X-ray pinhole image pairs, one set for an Argon-filled glass microballoon, the other for a Freon-filled plastic shell. The image for the Freon-filled target is dominated by the central core emission since the Chlorine in the fill gas is the highest Z element in the target, (Fluorine has Z = 9). The dominance of the core emission means that the noise level, due to emission from the ablation plasma, is low in the X-ray spectra produced.

A typical spectrum is shown in Fig. 5.9. The line profiles were compared with theoretical profiles as before and the electron density determined. Fig. 5.10 shows the digitised experimental profile of

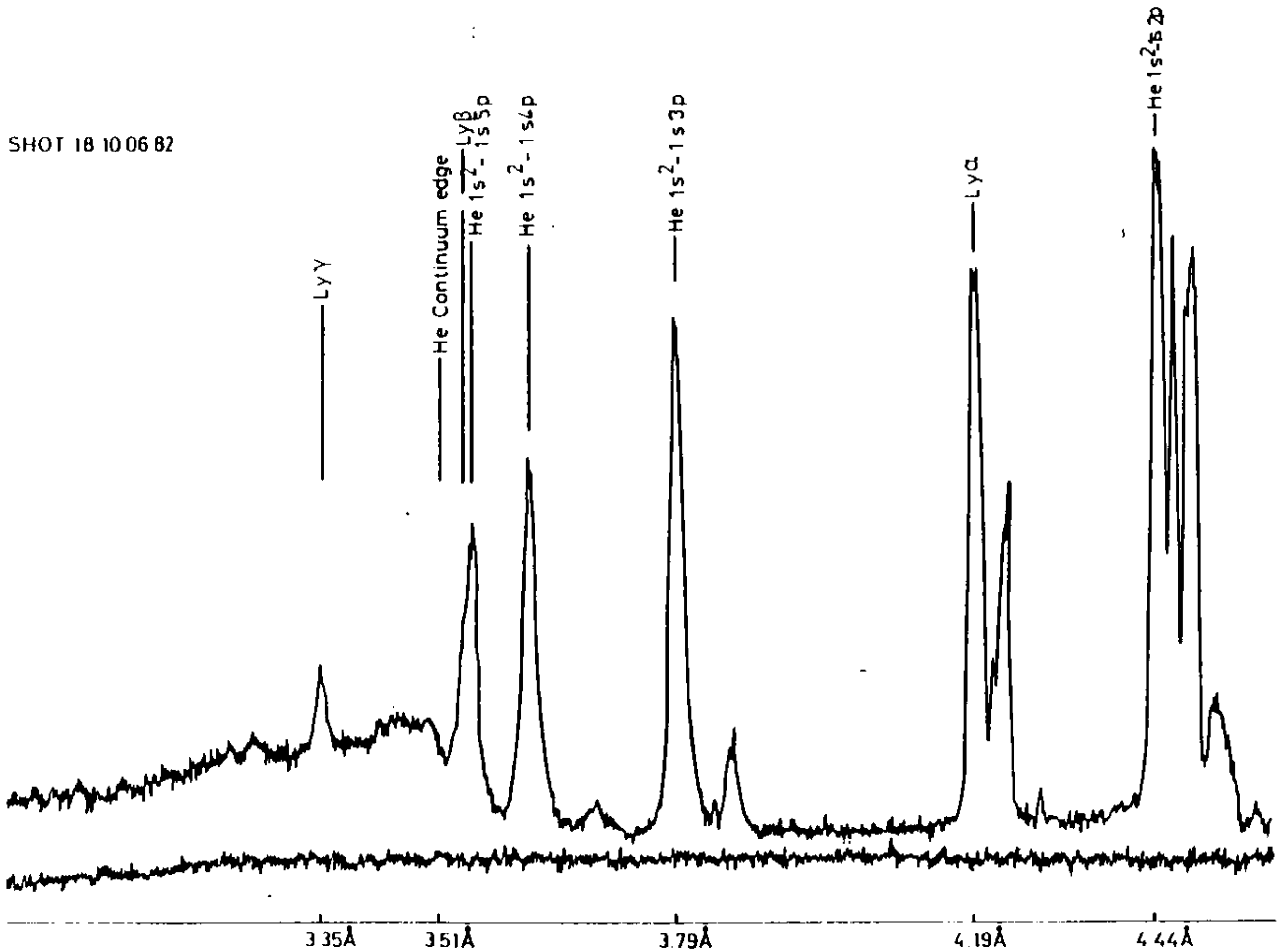

CHLORINE CORE SPECTRUM

Fig. 5.9. Chlorine spectrum from imploded polystyrene microshell containing 1 atmosphere of Freon 12.

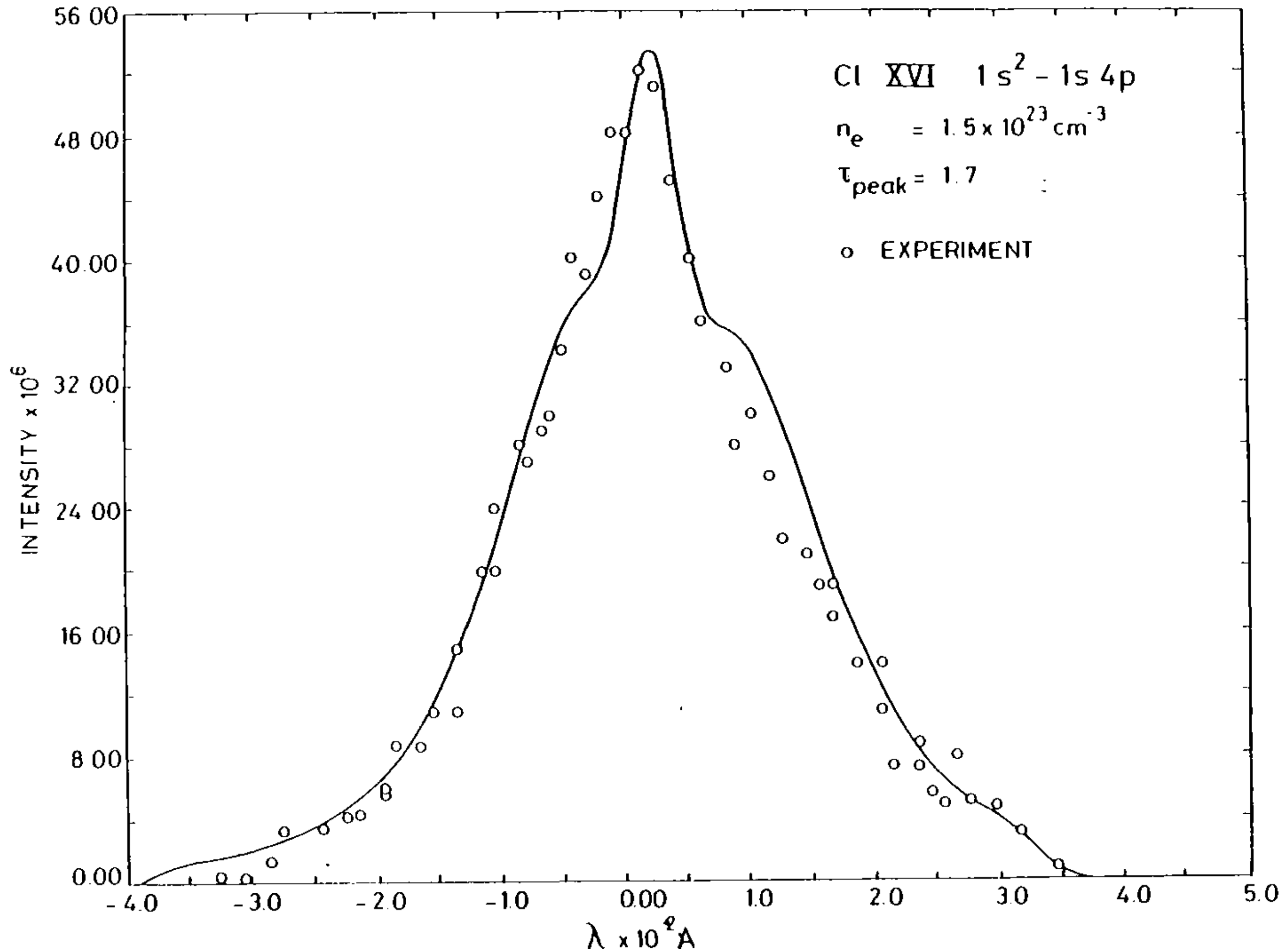

Fig. 5.10. Fit of theoretical line profile of Cl Heγ to digitised experimental line shape.

TABLE III

Shot	Initial Diameter	Plastic Shell Thicmness	Absorbed Irradiance	Specific Absorbed Energy	Compressed Chlorine Electron Density		Compressed Chlorine Electron Temperature
					From Lyα Satellite Ratio	From Line Broadening	
Units	μm	μm	$W\ cm^{-2}$	J/ng	cm^{-3}	cm^{-3}	eV
18 100682	112	2.3	$3.4\ 10^{14}$	0.14	$(1.2\pm0.15)10^{23}$	$(1.5\pm0.1)10^{23}$	810 ± 20
13 110682	110	3.7	$3.7\ 10^{14}$	0.10	$(2.5\pm0.4)10^{23}$	$(2.1\pm0.2)10^{23}$	740 ± 20
12 170682	119	2.9	$2.8\ 10^{14}$	0.09	$(0.6\pm0.5)10^{23}$	$(1.7\pm0.2)10^{23}$	540 ± 40

Cl Heγ fitted to the theoretical profile of a Stark and opacity-broadened Heγ.

The electron temperatures were determined by comparing the Lyα to Heγ intensity ratio with a calculation similar to that of Fig. 5.4 but rerun for Chlorine.

5.4.2 Results

The characteristics of the three implosions are summarised in Table III. A further calculation of electron density was possible from the ratio of the Lyα satellites. The ratio of the $2p^2\ ^1D_2$ - $1s2p\ ^1P_1$ transition to the $2s2p\ ^3P$ - $1s2s\ ^3S$ and $2p^2\ ^3P$ - $1s2p\ ^3P$ transitions has been shown to be an electron number density diagnostic (5.07). The results of comparing the ratios of these satellites of Cl Lyα are given in Table III alongside the line-broadening results. Fig. 5.11 shows Cl Lyα and its satellites for one of the implosions.

Comparison of the results of Table III with the Argon-filled target implosions of Table II indicates that slightly higher densities are achieved with the thicker walled targets listed in each Table. The 3.7 μm thick shell of shot 13 110682 is equivalent in areal density to a glass thickness of 1.5 μm and so can be compared with shot 09 180682 (Table II) which had a 1.7 μm thick shell and produced an only slightly lower density. It is difficult to see a strong correlation between the use of plastic shells and an increase in compressed density from the data available.

The Helium-like recombination edge of Chlorine has been calculated and observed to lie at a wavelength of 3.39 Å(5.08). The spectrum of Fig. 5.9 shows continuum emission up to a wavelength of 3.51 Å. The 'edge' position, corresponding to the energy required to ionise from

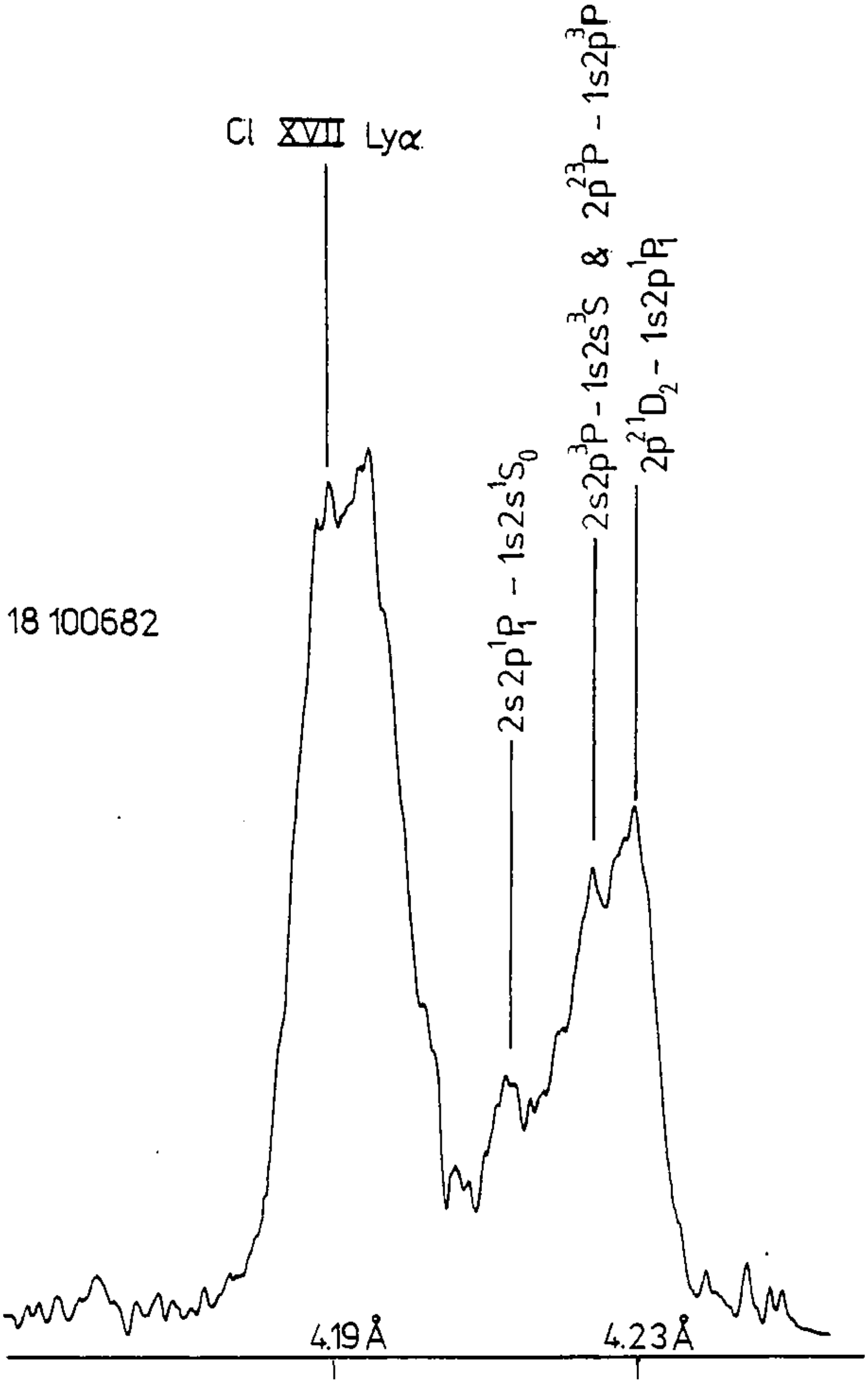

Fig. 5.11. Hydrogen-like Chlorine Lyα plus Helium-like satellites.

the K shell of Helium-like Chlorine, has been shifted due to the effect of the plasma surrounding the ions.

Two effects can shift the apparent position of the edge. The first is Debye depression (mentioned in Chapter 4), where the potential an electron 'sees' due to the ion extends only one Debye length from the ion. The electron will be screened from the ion when it is further than one Debye length from the atom. The depression of the Helium-like ionisation potential E_K is then:

$$E_K = -\frac{(Z-1)^2}{4\pi\varepsilon_0 \lambda_D} \qquad (5.01)$$

where λ_D is the Debye length and Z is the nuclear charge on the ion. It is possible that for high densities the Debye length is smaller than the ion sphere radius R_i defined by

$$\frac{4\pi}{3} n_e R_i^3 = Z_i \qquad (5.02)$$

where Z_i is the net charge on the ion. A sphere with radius R_i contains enough electrons to neutralise the ion's charge. In the limit of λ_D smaller than R_i there are not enough electrons in a sphere of radius λ_D to shield an electron which has been moved a distance λ_D from the ion. Therefore in this limit equation (5.01) is not valid. A reasonable approximation is to replace λ_D by R_i in equation (5.01). The model of Stewart and Pyatt[5.09] handles the limit of $\lambda_D < R_i$ and tends to equation (5.01) in the limit of $\lambda_D > R_i$. The potential depression from their model is:

$$\Delta E_K = -\frac{3}{2}\frac{Z_i e^2}{4\pi\varepsilon_0 R_i}\left[\left(1 - \left(\frac{\lambda_D}{R_i}\right)^3\right)^{2/3} - \left(\frac{\lambda_D}{R_i}\right)^2\right] \qquad (5.03)$$

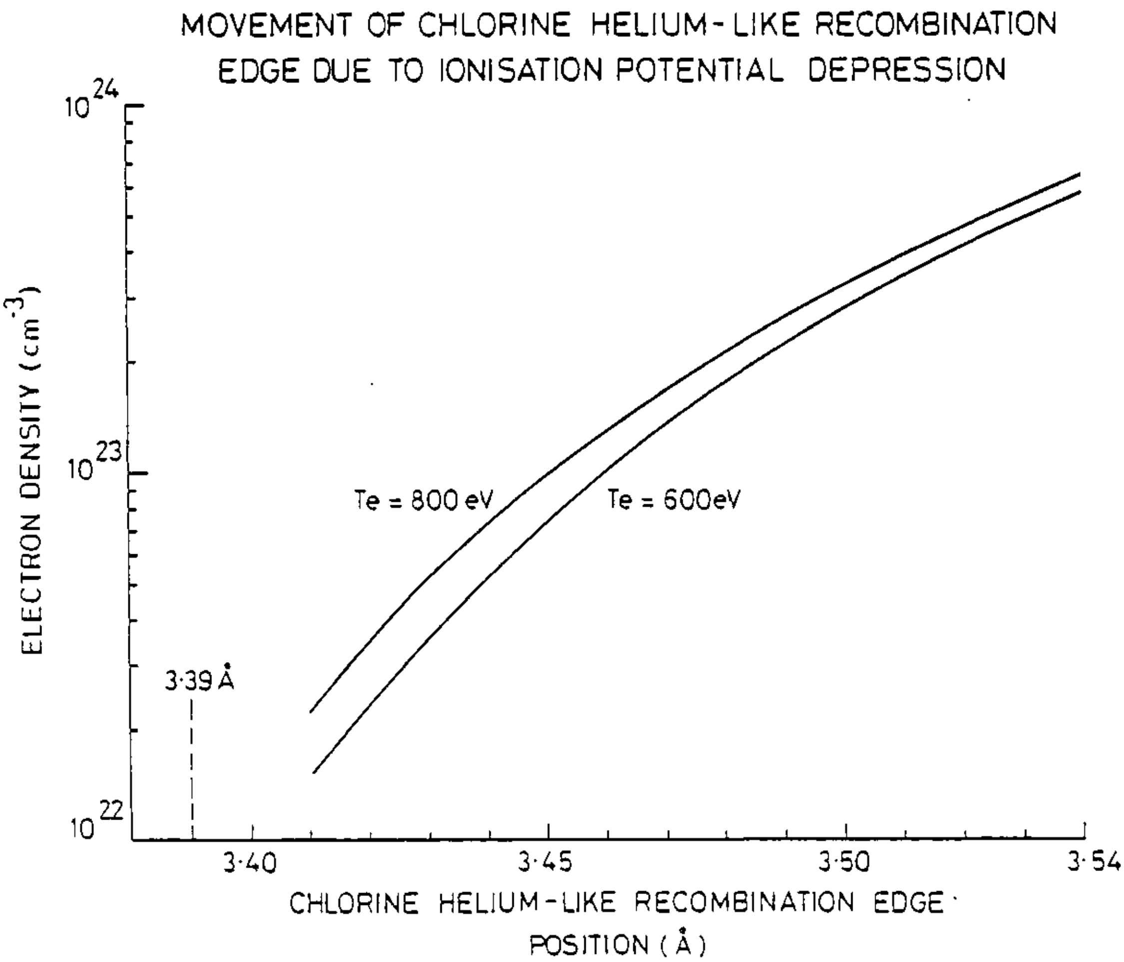
MOVEMENT OF CHLORINE HELIUM-LIKE RECOMBINATION
EDGE DUE TO IONISATION POTENTIAL DEPRESSION
10^{24}
10^{23}
10^{22}
ELECTRON DENSITY (cm^{-3})
Te = 800 eV
Te = 600eV
3·39 Å
3·40
3·45
3·50
3·54
CHLORINE HELIUM-LIKE RECOMBINATION EDGE
POSITION (Å)

Fig. 5.12.

The results of calculating the shift in Helium recombination continuum edge from equation (5.03) are plotted in Fig. 5.12.

The edge shifts observed in the three implosions all moved the edge to 3.5 ± 0.1 Å (e.g. Fig. 5.9). The Stewart-Pyatt model gives an electron density in excess of $3\ 10^{23}\ cm^{-3}$ for shifts of the magnitude observed.

The effect of merging of the upper energy levels with the continuum due to Stark broadening is neglected in Fig. 5.12. This effect is the second process that can shift the edge position. Higher order Helium-like resonance lines such as Heδ, Heε, etc., can be Stark broadened sufficiently that they become part of the continuum. The limit, where the separation between lines is less than twice their Stark width, is called the Inglis-Teller limit[5.10]. An examination of the shape of the recombination continuum edge (e.g. Fig. 5.9) reveals 'bumps' to the short wavelength side of the edge, corresponding to the positions of Heε and Heζ. These 'bumps' are either evidence that the Inglis-Teller limit must be applied, in order to determine an electron density from the edge position, or an effect due to time integration. It is possible that the 'bumps' were lines emitted when the plasma was at low density before the edge was shifted. However the fact that the Stewart-Pyatt model has overestimated the electron density compared with the results in Table III indicates that analysis of the edge position must include the Inglis-Teller limit.

5.5 Conclusions

High intensity implosions using both 0.53 μm and 1.054 μm radiation have been described and compared. The observed electron densities, in the compressed core, are higher for 0.53 μm irradiation by a factor of two, for similar targets and laser energies.

The effect of glass shell opacity in attenuating Argon lines has been inferred from the two experiments and the use of low opacity plastic targets proposed. The use of plastic targets containing a Freon 12 fill gas has been demonstrated, temperature and density diagnosis being from Chlorine emission. The density diagnosis was possible using both line shape fitting and measurement of Lyα satellite ratios. A further diagnostic using the shifted recombination edge position may be useful if sufficient analysis is carried out.

CHAPTER 6

COMPUTATIONAL SIMULATION OF ABLATION

6.0 Abstract

The one-dimensional Lagrangian hydrodynamic simulation code MEDUSA has been extended and used to model the ablation of material from spherical targets. Comparison of simulated mass ablation rates with experimental results at $\lambda = 0.53$ µm and $\lambda = 1.054$ µm has led to the conclusion that heat fluxes in excess of 10% of free streaming are present in the ablation region of laser-irradiated spherical targets.

6.1 MEDUSA

The one-dimensional program MEDUSA was written by J. P. Christiansen et al. at UKAEA Culham Laboratory(6.01) in order to study the hydrodynamic behaviour of a plasma subjected to the large power fluxes found in a laser-irradiated material. The program uses an implicit method of solving the thermodynamic equations on a Lagrangian mesh with explicit hydrodynamics.

6.1.1 Summary of MEDUSA

The program treats the plasma as 'two temperature' in that the electron and ion gases are handled separately although able to exchange energy by ion-electron collisions. In the original version transport of energy was by classical Spitzer conductivity (6.02) cut off at some empirically chosen fraction of the free-streaming limit. Absorption of laser energy was by collisional absorption (inverse bremsstrahlung) in the underdense plasma, coupled with a dump of energy at critical density. The equations of state used were a perfect gas equation for the ions and either a perfect gas or a Fermi degenerate gas for the electrons. The initial form of MEDUSA assumed a fully ionised plasma with only Hydrogen and Helium isotopes present. The action of shock-waves and fluid motion during pellet compression were modelled together with nuclear reaction rates and self heating (ignition) of the fuel.

Subsequently MEDUSA has been modified to allow the inclusion of high Z elements in simulations(6.07). The ε and δ_t parameters have been included in the Spitzer conductivity which was previously correct only for $Z = 1$. The ionisation balance for up to five different elements is now calculated using a modified form of the Saha equation(6.03). The modification to the Saha equation avoids an unphysically high ionisation at low densities and instead approximates to a coronal equilibrium.

The electron gas equation of state now includes the effects of partial degeneracy, ionisation and binding energies through the Thomas-Fermi model(6.04). The model has had optional quantum corrections added(6.05) to handle binding energy in the cold dense solid phase. The equation of state produces essentially zero pressure in the cold solid and tends asymptotically towards an ideal gas equation of state at high temperature and low density. The equation of state has been compared with tabulated data(6.06) and is in good agreement for all regimes found in laser driven targets(6.07).

Fast electron production due to resonance absorption has been included in the code but since a fluid model does not contain enough information to calculate the hot electron temperature T_H an empirical formula is used. The formula is that of Giovanelli et al.(6.08)(6.09) where the fast electron temperature is found to be a function of $I\lambda_0{}^2$, where I is the laser intensity reaching the neighbourhood of critical density and λ_0 is the free space wavelength of the laser. The transport of the fast electrons is performed by dividing the distribution function into ten groups and calculating the rate of energy loss as the groups travel through the target, using standard formulae for fast test particles in a plasma(6.10). The total energy put into fast electrons is set empirically at 10% of that reaching critical density. Some justification for a 10% conversion into fast electrons comes from experiments(6.12)(6.13)(6.14) and also from matching simulations to exploding pusher implosions where the behaviour of the target is dominated by fast electrons(6.15)(6.16).

6.1.2 Modifications to MEDUSA (made by the author)

6.1.2.1 Saturated heat flow. In its original form MEDUSA imposed a limit on the permissible heat flow by calculating the harmonic mean of the Spitzer conductivity and some adjustable fraction f of the free streaming limit or saturation flux q_{sat}.

$$q_{sat} = - n_e \, k_B \, T_e \sqrt{\frac{k_B T_e}{m_e}} \frac{\underline{\nabla} T_e}{|\underline{\nabla} T_e|} \qquad (6.01)$$

Some early work had shown little dependence of target behaviour on the value of f chosen(6.34). This result was found to be due to large numerical errors in the original formulation of the free-streaming flux. On correcting the errors many simulation observables became dependent on

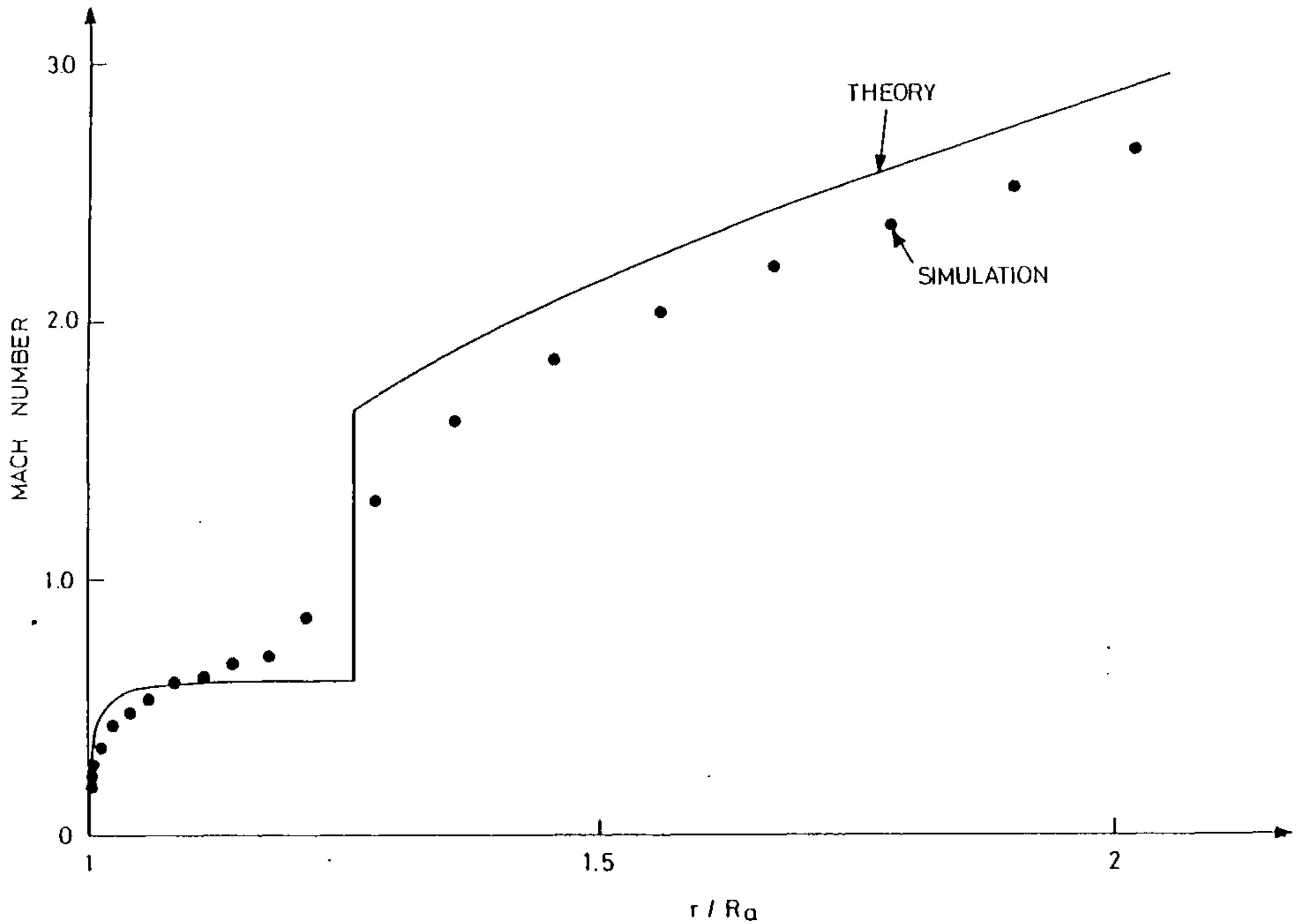

Fig. 6.1. Isothermal flow Mach number as a function of radius normalised to the ablation radius.

the fraction f of the free streaming limit chosen as the upper limit on the heat flow[6.17]. The method of implementing the limit on the heat flow was altered to be an abrupt cut-off of the Spitzer value at $f.q_{sat}$. The algorithm for calculating the saturation flux was taken from the paper of Max et al.[6.18] (Appendix D), which details an analytic model for laser ablation from spherical targets.

The analytic theory of reference 6.18 was used as a comparison with MEDUSA in order to check the hydrodynamics and energy transport. The theory of reference 6.18 is steady state and assumes that all energy from the laser is dumped at critical density. A simulation was run using a flux limit of f = 0.03 and a laser wavelength of 1.054 μm; Lagrangian zoning of $3\ 10^{-6}$ g cm^{-2} was used. An absorbed intensity of $8.33\ 10^{12}$ W cm^{-2} was dumped as electron thermal energy at critical density. The simulation was run for 4 nanosec at constant laser power in order to achieve the steady state required for comparison with the theory. A comparison between observables from the simulation (column B) and the results of Max et al. (column A) is made in Table I below.

Agreement between the analytic theory and the simulation using zones of $3\ 10^{-6}$ g cm^{-2} is good, the worst discrepancy being a 15% over-estimate of the total mass ablation rate by MEDUSA. The isothermal flow Mach number is plotted in Figure 6.1 as a function of radius normalised to the ablation radius. The solid curve representing analytic theory shows a sharp discontinuity at critical density. The finite mesh resolution given by the $3\ 10^{-6}$ g cm^{-2} simulation partially smooths out the discontinuity as shown by the points in Fig. 6.1 but the saturation of the Mach number at M_s = 0.6 (corresponding to flux limit f = 0.03) is evident in the region inside critical density. For a flux limit of 10% the flow is supersonic inside critical and there is

TABLE I

		Column A	Column B	Column C
Observable	Units	Analytic Theory	Simulation $3\ 10^{-6}$ g cm^{-3}	Simulation $0.75\ 10^{-6}$ g cm^{-2}
Temperature at Critical Density	Kelvin	$5.4\ 10^{6}$	$(4.9 \pm 0.1)\ 10^{6}$	$(5.26 \pm 0.07)\ 10^{6}$
Radius at Critical Density	Ablation Radius	1.21	1.26 ± 0.02	1.20 ± 0.01
Ablation Pressure	Mbars	1.72	1.71 ± 0.02	1.73 ± 0.015
Total Mass Ablation Rate	g s^{-1}	81	93	85

no discontinuity at critical density making mesh resolution less important. Column C of Table I will be referred to in a later section.

6.1.2.2 Absorption. MEDUSA had previously been used mainly for long wavelength, high intensity simulations where inverse bremsstrahlung absorption was unimportant, however for comparison with $\lambda = 0.53$ μm experiments inverse bremsstrahlung has become more significant. The previously incorrect Z scaling of the absorption coefficient was modified to agree with the formula of Johnston and Dawson[6.19].

6.1.2.3 Absorption for six-beam irradiation. In order to simulate $\lambda = 0.53$ μm ablation experiments performed using the 6-beam facility at Rutherford Appleton Laboratory it is necessary to model laser absorption in the underdense plasma taking account of refraction of the beams due to incidence at an angle to the density gradient. In order to obtain almost uniform illumination of a sphere by six f/1 beams they must be defocused to three or four target radii beyond the centre of the target. Hence the beams overlap producing illumination uniformity to within ± 10% (as observed from X-ray pinhole pictures) at the expense of low absorption and beam refraction. As most parts of the laser beams are incident at an angle to the density gradient they are refracted around the target being reflected at densities below critical. Therefore the absorption takes place at lower density than for beams focused at the target centre, producing lower ablation rates for the same absorbed intensity.

In order to model illumination by six beams MEDUSA was altered to do a two-dimensional raytrace for a cross-section of half of one beam.

The raytrace was two dimensional as, due to the spherical symmetry of the density gradient, rays refracted around the target have trajectories which remain in a plane, in a manner analogous to particles being deflected by a central field, e.g. gravity. The cylindrical symmetry of the beams meant that a cross-section of half one beam could be split into rays, their paths calculated and the total absorption calculated from the result.

The trajectories of the individual rays were calculated by using Snell's Law:

$$\mu \sin \theta = \text{constant} \tag{6.02}$$

The refractive index μ is simply:

$$\mu = \left[1 - \frac{n_e}{n_c} \right]^{\frac{1}{2}} \tag{6.03}$$

where n_e is electron number density and n_c critical electron number density.

The rays were refracted through a subsidiary mesh of finer spacing than the Lagrangian mesh for the hydrodynamics. The condition of equation (6.02) was applied at each zone interface and the ray's direction of travel changed. Absorption along the ray's path was calculated using the formula of reference 6.19. Altering the resolution of the subsidiary mesh from typically three times that of the hydrodynamics mesh to thirty times did not affect the absorption $U(r,\theta)$ in the two-dimensional raytrace noticeably. Therefore it was deduced that the method of calculating ray trajectories was sufficiently accurate for the calculation required.

The beam was treated as Gaussian in spatial profile with a fill factor of 0.5 incident at f/1, defocused by typically four target radii. After calculating the absorption for one beam the absorption due to the other five beams followed from simple transformations. An example of the results of this calculation is shown in Fig. 6.2 where the absorption $U(r,\theta,\phi)$ in watts/kg is plotted as a function of radius for 3 positions on the target. For comparison, the absorption profile for light incident normal to the surface of the sphere is also plotted where the total specific absorbed energy has been chosen to be the same as in the other three cases. Although the variation in the shape of the absorption profile is noticeable for the three cases shown, the total absorbed energy as a function of θ and ϕ on the target was found to be constant to within 10%, in agreement with X-ray pinhole pictures of targets using the same illumination conditions. The uniformity of the refracted illumination enabled the use of a spherically averaged power deposition U(r).

$$\overline{U}(r) = \int_0^{2\pi} \int_0^{\pi} U(r,\theta,\phi) \frac{\sin\theta}{4\pi} \, d\theta \, d\phi \qquad \text{watts/kg} \qquad (6.04)$$

This one-dimensional deposition profile was then input to MEDUSA producing more absorption at low density than for illumination normal to the target surface. Simulations were run using U(r) taken as the absorption profile at one particular point (θ,ϕ) on the sphere, i.e. one of the particular cases shown in Fig. 6.2. The observables (i.e. ablation rate, pressure, ion velocity and absorption) were found to vary by at most 10% compared with the spherically averaged $\overline{U}(r)$ defined in equation (6.04). Although a 10% variation in ablation pressure would be detrimental to achieving high density in an ablative implosion the 10% difference in ablation rate does not greatly affect

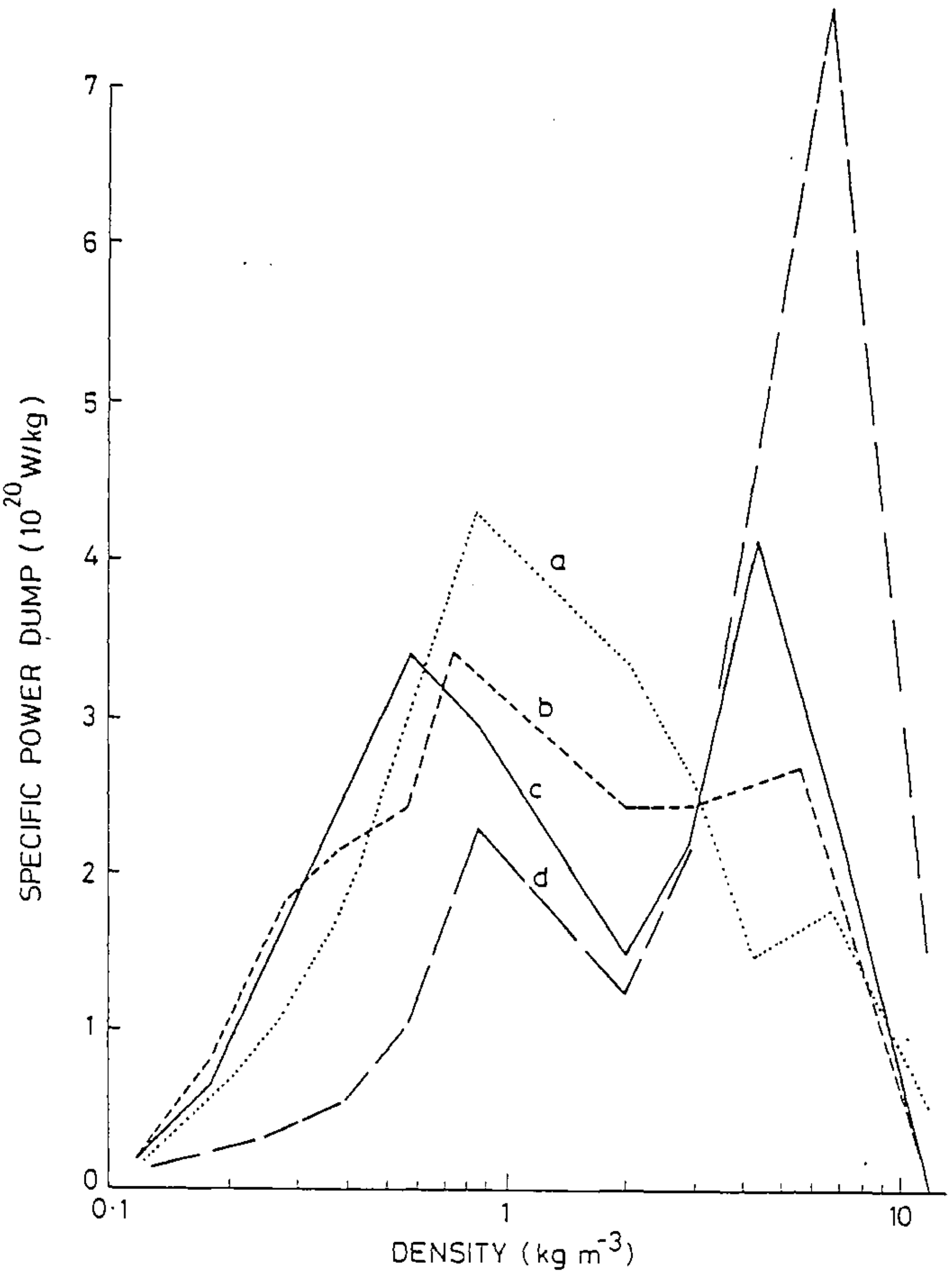

Fig. 6.2. Absorption profiles predicted at different points around a spherical target due to six-beam laser irradiation. The beams are incident with cubical symmetry along the Cartesian axes; the absorption is plotted for three points on the sphere. (a) The centre of one of the beams. In spherical polar coordinates, $\theta=0$, $\phi=0$. (b) The point where two neighbouring beams overlap, e.g. $\theta=45^{o}$, $\phi=0$. (c) The point where three neighbouring beams overlap, e.g. $\theta=45^{o}$, $\phi=45^{o}$. (d) For comparison, the absorption profile for spherically symmetric illumination is plotted.

comparisons with experimental mass ablation rate results. Therefore it seems justifiable to use the spherically averaged $\overline{U}(r)$ to model mass ablation rate experiments.

A comparison of simulations performed with and without refraction effects included is shown in Table II below for a 100 μm diameter target irradiated with a 1 nanosec pulse of λ = 0.53 μm light. The absorbed irradiance was 3.1 10^{13} W cm^{-2}; a flux limit of f = 0.03 was used.

TABLE II

RUN	Illumination Conditions	Specific Mass Ablation Rate g cm^{-2} s^{-1}
A	Normal Incidence Illumination (Standard MEDUSA)	1.42 10^5
B	Six f/1 Beams Refraction Included	1.06 10^5
C	Six f/1 Beams Focused at Target Centre. (Hence no refraction.)	1.30 10^5

Run A using the standard MEDUSA prescription for absorption shows a much larger ablation rate than Run B which includes the refraction effects. Run C uses the ray-tracing modification but for normal incidence illumination. This last case should agree with the first, standard MEDUSA run, however the ablation rate is slightly lower as the standard MEDUSA uses an approximation for anomalous absorption whereby

20% of light reaching critical density is absorbed. The ray-trace modification uses a better treatment of anomalous absorption which will be described in the next section.

6.1.2.4 Resonance absorption in the two-dimensional ray trace.

Resonance absorption from the refracted rays was handled by adapting the results of Forslund et al.(6.20). They used a two-dimensional Particle-in-Cell code to model the interaction of a laser with a linear density gradient from a plane target. They considered a p polarised beam incident at an angle θ_0 to the density gradient. From equations (6.02) and (6.03) the beam is reflected at a density:

$$n_e = n_c \cos^2 \theta_0 \qquad (6.05)$$

The analytic theory of Ginzburg(6.11) has shown that the energy absorbed by resonance absorption is a function of $(k_0 L)^{2/3} \sin^2\theta_0$, where k_0 is the free space wave number of the laser and L is the scale length of the density gradient. The planar results of Forslund et al. are applicable to the case of light incident at an angle to the density gradient from a spherical target provided that the radius of the critical density surface is large compared with the separation of the reflection point of a light ray and critical density. This condition is necessary so that at the point where the ray turns round and its E field contributes to absorption, it sees an effectively planar density gradient leading up to critical density. Fig. 6.3 summarises the results of reference 6.20 as used in the ray trace where absorption for $\sin \theta_0 = 0$ has been set at 20% in order to give better agreement with short pulse experiments(6.33). For long pulse simulations most resonance absorption will take place at large values of $(k_0 L)^{2/3} \sin^2\theta_0$.

Note that the results in Fig. 6.3 are parameterised by $\sin^2\theta_0$ which in the planar case gives the density at reflection (equation (6.05)). In the spherical case the reflection density is a more complicated function of the angle of incidence but Fig. 6.3 can be used by replacing $(k_0L)^{2/3}\sin^2\theta_0$ by $(k_0L)^{2/3}(1 - \frac{n_e}{n_c})$ and inserting n_e directly from MEDUSA at the point of reflection. The density scale length L is calculated by approximating the density gradient joining the reflection point to critical density as linear.

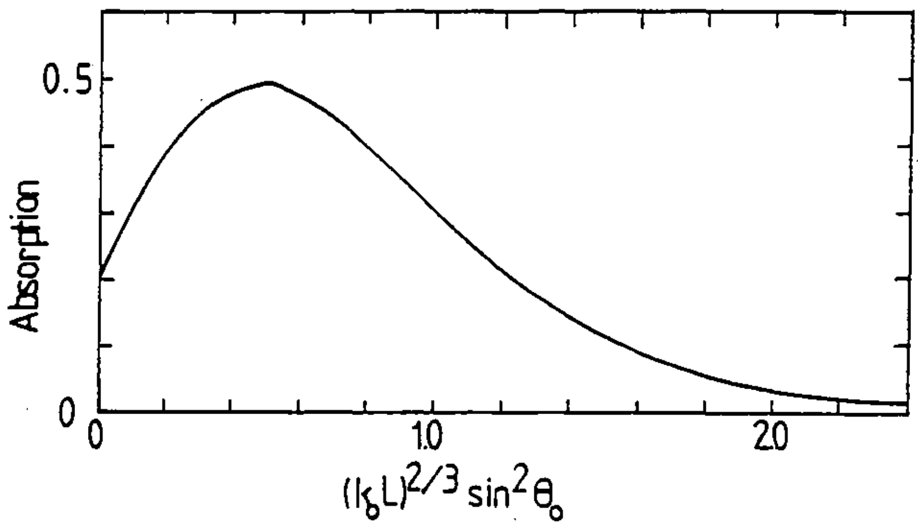

Fig. 6.3. Fraction of beam resonantly absorbed as a function of angle of incidence θ_0 and density scale length L. Adapted from ref. 6.20.

The calculations of reference 6.20 assume the laser is p polarised, i.e. that the E field of the laser lies in the plane of motion of the refracted ray. For polarised light focused onto a spherical target the E field has a p component which varies from zero to $\pm E_0$ where $E_0 = |\underline{E}|$.

As mentioned before, the trajectories of individual rays will lie in planes and the laser E field will have a p polarised component lying in that plane which will vary across the beam as $E_0 \sin \psi$. The s polarised parts of the beam will not contribute significantly to resonance absorption for long pulse simulations at intensities below 10^{16} W cm^{-2}. Therefore to calculate an average absorption for the whole beam the p component of intensity must be averaged around the cylindrical beam. The presence of a preferred direction of polarisation of the laser breaks the cylindrical symmetry that has been assumed so far for each beam. The average p intensity is therefore:

$$I_p = I_0 \frac{\int_0^{2\pi} E_0^2 \sin^2 \psi \, d\psi}{\int_0^{2\pi} E_0^2 \, d\psi} = \frac{I_0}{2} \qquad (6.06)$$

Anomalous absorption can therefore be calculated by assuming the beam is all p polarised, relative to the plane through which it refracts, and then taking half the Forslund value for absorption. This calculation then produces an average absorption but as described in the preceding section, when the effect of six beams is included the variations in total absorption are less than 10% around the sphere.

<u>6.1.2.5 Optimisation of mesh resolution</u>. The resolution of the Lagrangian mesh near critical density is important for the correct representation of heat flux saturation for flux limit of 3% or less. A fine zoned mesh can be applied by starting the simulation with more zones packed closely together, however this will increase the required computer time for two reasons. The first is that the more Lagrangian cells there are the more calculations have to be performed per timestep.

The second reason is that although the treatment of the temperature equation in MEDUSA is implicit, imposing few constraints on the time-step size, the Navier-Stokes equation is differenced explicitly. The timestep is therefore limited by the C.F.L. condition

$$\Delta t \; < \; \frac{\Delta r}{V_s} \; = \; \Delta r \left(\frac{\rho}{\gamma P}\right)^{\frac{1}{2}} \tag{6.07}$$

where V_s is the sound speed in the plasma and Δr is the zone size at that time. For zones in the ablation region, that will not have moved an appreciable distance since the start of the simulation:

$$\rho \; \propto \; \frac{1}{\Delta r} \tag{6.08}$$

The C.F.L. condition can then be rewritten as

$$\Delta t \; \sim \; \left(\frac{\Delta r}{\gamma P} \right)^{\frac{1}{2}} \tag{6.09}$$

Producing a finer mesh by globally reducing the zone sizes Δr, reduces the permitted timestep and increases the required computer time.

The zones which impose the greatest restriction on Δt, in a laser plasma simulation, are on the high density side of the ablation front where material is just about to be removed from the target surface. Here Δr is small and the pressure P is large. Small zones can be used without limiting the timestep if they are created by splitting up larger zones as they leave the target surface. A treadmill rezoner(6.21) was incorporated in MEDUSA to perform this function. The rezoner splits the zones as they are ablated from the target and by the time they flow into the critical density region successive splits can have reduced the zone mass by a factor of 8. To avoid having the number of cells increasing as the simulations progress, the zones are merged back together on reaching the low density side of critical where scale lengths are longer and a coarse mesh can be used.

Table I, Column C, shows the results of a simulation using a treadmill rezoner compared with the analytic theory of reference 6.18 (Column A) and a coarser zoned simulation (Column B). The zoning at critical density was finer by a factor of 4 in the simulation using the treadmill rezoner and this is reflected in the better agreement with the analytic results. However the finer zoned simulation used less computer time by a factor of 3, resulting in a better simulation plus a substantial saving in computer time. The simulation shown in Column B required 80 minutes of CPU time in order to run for the 4 nanosecs of MEDUSA time required.

The minimum zone size that is usable with the rezoner is set when the internal energy of a cell becomes comparable with the heat flowing through it in one timestep. When this happens the timestep must be reduced and the code slowed down as a result.

6.2 Simulation of Experiment

6.2.1 Introduction

At Rutherford Appleton Laboratory as well as other laboratories, much work has been done in order to measure the ablation pressure produced by the action of a laser on a plane target[6.22][6.23][6.24]. In most experiments the quantity measured has been the specific mass ablation rate $\dot{m}_s$. Attempts to match up the measured ablation rates with one-dimensional planar simulations showed that heat fluxes in the simulation had to be restricted to less than 3% of free streaming[6.23]

(6.24). However experiments using plane targets and relatively small focal spots are subject to edge effects which make simulation with a one-dimensional code difficult. The lateral flow of energy away from the focal spot (as described in Chapter 2) reduces the heat flow into the target leading to a reduced mass ablation rate for a particular absorbed energy. Hence when modelling the experiment using a one-dimensional code without edge losses, the heat flux must be strongly inhibited to produce agreement with the measured ablation rate.

Planar measurements of ablation rate also suffer from interpretation difficulties. One method(6.35) of measurement is to observe the delay between emission of characteristic X-rays from different layers in the target as the laser burns through them. The laser focal spot intensity distribution is approximately Gaussian and defining an average intensity in the spot to relate to a uniform intensity illumination in a one-dimensional simulation is difficult. At low intensity when lateral smoothing is low the burn through rate will peak at the peak intensity giving a high reading of ablation rate and at high intensity when flux limiting is important edge losses will make simulation difficult.

Experiments have been performed in spherical geometry using 6 synchronous laser beams to irradiate microballoon targets(6.25). The lack of edge effects and the ability to provide illumination uniformity to within ± 10% by defocusing the beams means that these experiments are more suitable for comparison with a one-dimensional code.

6.2.2. The Experiments

Microballoons of diameters 70 μm to 120 μm were illuminated with laser irradiances in the range $3\ 10^{12}$ W cm^{-2} - $7\ 10^{13}$ W cm^{-2} absorbed, in two separate experiments using wavelengths of 0.53 μm and 1.054 μm. Laser pulse durations of 1.1 nanosecs and 1.3 nanosecs were used. The mass ablation rate was determined in two ways:

(i) Time-resolved X-ray spectroscopy.

(ii) Charge-collecting Faraday cups.

6.2.2.1 Time-resolved X-ray spectroscopy. Glass microballoons were coated with a layer of plastic of thickness 1 - 2 μm. A thin layer of Aluminium (0.1 μm) was coated over the plastic. Time resolution of X-ray line emission from the target enabled the delay τ, between the first appearance of Aluminium emission and the appearance of Silicon emission from the glass, to be measured. The specific mass ablation rate was then:

$$\dot{m}_s^{\times} = \frac{\rho_{CH}\,\Delta r_{CH}}{\tau} \quad \text{g cm}^{-2}\ \text{s}^{-1} \tag{6.10}$$

where ρ_{CH} is the initial plastic density and Δr_{CH} the initial thickness of the plastic. The specific mass ablation rate has been referenced to the initial target surface.

6.2.2.2 Charge-collecting Faraday cups. An array of 5 Faraday cups placed 38 cm from the microballoon collected ions flowing out from the target. The current produced allowed a direct calculation of the total charge on the ions ablated from the target. The delay on the current pulse gave the flight time of the ions and hence their velocity. The total kinetic energy of the ions is given by:

$$E_{ion} = \tfrac{1}{2} M \bar{v}^2 \tag{6.11}$$

where M is the total mass ablated off the target and $\bar{v}$ is the mean ion velocity deduced from the current delay. Note that only ions travelling faster than $2\ 10^7$ cm s^{-1} were included in the calculation of the mean ion velocity due to the fact that the Faraday cup measures current, which is the rate of arrival of charge at the cup. Slow ions tend to have a low charge state so the low velocity remnants of the target are not detected by the Faraday cup and so are not included in the ablation measurement.

The ion kinetic energy was measured by an array of differential calorimeters that select out the absorbed energy E_{abs} contained in soft X-rays and ion kinetic and thermal energy. The soft X-ray fraction f_x has been measured(6.26) to be 15% and 5% of E_{abs} for the target materials considered, for λ = 0.53 μm and 1.054 μm respectively. Correcting E_{abs} for the X-ray component we obtain:

$$M = \frac{2\ E_{abs}}{\bar{v}^2} (1 - f_x) \tag{6.12}$$

The specific mass ablation rate referenced to the initial target radius R is then:

$$\dot{m}_s^I = \frac{2\ E_{abs}}{\bar{v}^2} (1 - f_x) \frac{1}{4\pi R^2\ \tau_L} \quad \text{g cm}^{-2}\ \text{s}^{-1} \tag{6.13}$$

where τ_L is the full width at half height of the laser pulse. The absorbed irradiance is:

$$I_{abs} = \frac{E_{abs}}{4\pi R^2\ \tau_L} \quad \text{W cm}^{-2} \tag{6.14}$$

again referenced to the initial target surface. The resultant scaling of $\dot{m}_s$ with absorbed irradiance is

$$\dot{m}_s = 9.35\ 10^4\ I_{13}^{0.72} \qquad g\ cm^{-2}\ s^{-1} \qquad (6.15a)$$

$$\dot{m}_s = 8.9\ 10^4\ I_{13}^{0.86} \qquad g\ cm^{-2}\ s^{-1} \qquad (6.15b)$$

for λ = 0.53 μm and 1.054 μm respectively(6.27)(6.28), where I_{13} is the absorbed irradiance expressed in units of 10^{13} W cm^{-2}.

The scaling of $\dot{m}_s$ is almost linear with I_{abs} indicating that any error in E_{abs} will not affect the results too greatly as it would affect $\dot{m}_s$ and the corresponding value of I_{abs} in almost equal proportion. The error bar on Fig. 6.5 is thus plotted at 45° to the axes to emphasise the accuracy of this measurement. A more detailed account of these experiments in given by T. J. Goldsack in reference 6.28.

6.2.3 The Simulations

Simulations were performed using target parameters similar to the actual experiments. Microballoons were a range of diameters from 70 μm to 120 μm with glass shell thicknesses of 1 to 2 μm coated with ∿ 1 - 2 μm of plastic and ∿ 0.1 μm of Aluminium. Simulations were run using flux limiters of 30%, 10%, 3% and 1% with the bulk of the work concentrating on 3% and 10% flux limiters. Both λ = 0.53 μm and λ = 1.054 μm simulations were run. Lagrangian zones of 3 10^{-6} g cm^{-2} were used in the ablation region in order to provide resolution of the steep temperature gradients between critical density and the target surface. The zone size increased steadily towards the inside of the glass shell in order to reduce the total number of mesh points. The maximum difference in mass of neighbouring zones was however kept below 10% in order to provide smooth transit of the shock wave through the shell.

The ray trace was used with the six beams defocused 4 radii beyond the target. The laser pulse was trapezoidal in time with a full width at half height of 1.1 nanosec and 1.3 nanosec for the $\lambda = 0.53$ and $\lambda = 1.054$ μm simulations respectively. The pulses were flat topped with a rise and fall time of 100 picosecs, rise and fall times of 500 picosecs were also used but the full width of the pulse was kept constant.

The ablation rate was measured in three ways:

(i) Directly by measuring the total mass removed from the target by the laser.

(ii) Simulating a Faraday Cup signal.

(iii) Plotting the Lagrangian position of the $T_e = 300$ eV isothermal as it moved through the shell.

Method (ii) meant allowing the simulation to run for 3 nanosecs after the laser had switched off, until the ion velocities and charge states had become asymptotic. The coronal modification to the Saha equation meant that the charge state in this low density plasma was a good approximation to the experimental situation. The flow of charge due to each Lagrangian zone could be extrapolated to give an arrival rate at the Faraday cup and hence a simulated current. The detector threshold when applied was found to cut off ions with velocities below $2.0\ 10^7$ cm s^{-1} as in the experiment. The ion kinetic energy as measured by a plasma calorimeter was also calculated and found to contain $\sim$ 90% of the total absorbed energy. The mass ablation rate was then calculated using equation (6.13). The absorbed intensity was calculated from equation (6.14).

Method (iii) was used in order to compare time-resolved X-ray spectroscopic methods of experimentally measuring $\dot{m}_s$ with the Faraday cup method. The position of the $T_e = 300$ eV isothermal is a measure of the amount of the target that is emitting characteristic X-ray line spectra. Hence the speed of motion of the isothermal through the

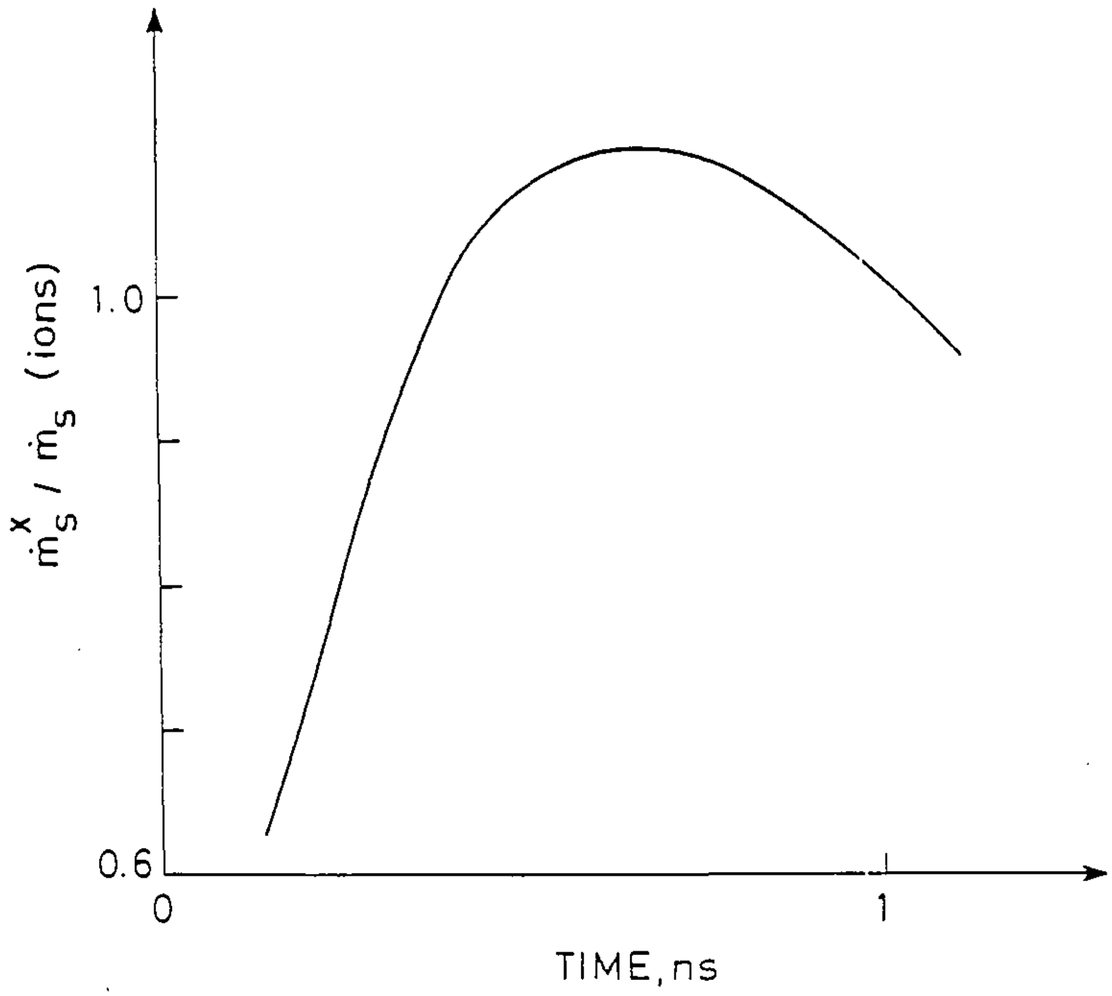

Fig. 6.4. The ratio of the X-ray determined ablation rate to the time-averaged, Faraday cup determined ablation rate as a function of time.

target expressed in g cm^{-2} s^{-1} is the specific mass ablation rate. For a burn through (as measured by X-ray streak camera) at time t, the mass ablation rate will be:

$$\dot{m}_s^x = \frac{1}{t}\int_0^t \dot{m}(t)\ dt\ \frac{1}{4\pi R^2} \tag{6.16}$$

Following the 300 eV isothermal gives a measure of $\dot{m}_s^x$ as a function of time throughout the laser pulse.

<u>6.2.3.1 Observations from the simulations</u>. Method (i) of measuring the mass ablation rate directly compared very well with the simulated Faraday cup method. Agreement was usually better than 10%, improving for longer pulse laser shots and higher intensity illumination. The X-ray spectroscopic method produced a different value of $\dot{m}_s$ depending on what time during the laser pulse was chosen to measure it. Fig. 6.4 shows the X-ray determined $\dot{m}_s^x$ as a function of time normalised to the time-averaged Faraday cup calculation of $\dot{m}_s$, i.e.

$$\frac{\dot{m}_s^x(t)}{\dot{m}_s^I} = \frac{\int_0^t \dot{m}_s(t)}{\int_{-\infty}^{\infty} \dot{m}_s(t)\ dt} \tag{6.17}$$

The X-ray determined ablation rate should be in reasonable agreement with the ion value for burn throughs (i.e. $\dot{m}_s^x$ measurements) after times greater than 400 picosecs.

Fig. 6.2 as described in an earlier section shows the absorption profile at 3 points on the target. The simulation from which the profiles were taken was of a target which had been coated with a 0.1 μm layer of Aluminium. The Aluminium layer was to act as a time marker for time-resolved X-ray spectroscopy. However it is obvious from the profiles (calculated at a time half way through the laser pulse) that the Aluminium is absorbing a significant amount of the incident energy due to its higher Z. The Aluminium layer is acting as a shield preventing energy reaching higher density. Increasing the layer thickness from 0.1 μm to 0.2 μm, as was used on some shots, led to a 17% reduction in $\dot{m}_s$ for a 10% flux limit and a 30% reduction when a 3% flux limit was used. Dispensing with the 0.1 μm Aluminium layer led to a 15% and 20% increase in $\dot{m}_s$ for a 10% and 3% flux limit respectively. Therefore although the mass contained in the thin layer is negligible, its effect on the target behaviour is noticeable and should be allowed for when simulating these kind of experiments.

6.2.4 Comparison of Experiment with Simulation

6.2.4.1 The form factor. The simulations were performed using a trapezoidal pulse shape as described earlier. The pulse used in the experiments was closer to a Gaussian in shape. Since from equations (6.15) the scaling of $\dot{m}$ with intensity is not linear some correction must be applied to allow for the pulse shape. A mean specific mass ablation rate is required such that:

$$\dot{m}_s^I = \frac{\text{Total Mass Ablated}}{\tau_{\dot{m}}\, 4\pi R^2} \qquad (6.18)$$

Where $\tau_{\dot{m}}$ is the full width at half height of the mass ablation pulse

$$\tau_{\dot{m}} = F\, \tau_L \qquad (6.19)$$

where F is the form factor.

From (6.18)

$$\dot{m}_s^I = \frac{\int_{-\infty}^{\infty} \dot{m}(t)\ dt}{F\ \tau_L\ 4\pi R^2} \tag{6.20}$$

Equations (6.15) show that $\dot{m}_s^I$ scales as $\langle I\rangle^x$ where $x < 1$. If the assumption is made that the time-dependent total mass ablation rate $\dot{m}(t)$ scales as $I(t)^x$ then the form factor F can be calculated.

The mean intensity $\langle I\rangle$ is

$$\langle I\rangle = \frac{1}{\tau_L}\int_{-\infty}^{\infty} I(t)\ dt \tag{6.21}$$

$$F = \frac{\frac{1}{\tau_L}\int_{-\infty}^{\infty} I^x(t)\ dt}{\left[\frac{1}{\tau_L}\int_{-\infty}^{\infty} I(t)\ dt\right]^x} \tag{6.22}$$

F = unity if x = 1 or I(t) = constant as is almost the case for the pulse used in some of the simulations. A Gaussian-shaped pulse will have a form factor greater than unity (for $x < 1$) implying that the mass ablation pulse width is greater than the corresponding laser intensity pulse width. For the $\dot{m}_s^I$ scalings of equations (6.15) the form factors are 1.20 and 1.08 for $\lambda = 0.53\ \mu m$ and $\lambda = 1.054\ \mu m$ respectively. The experimental $\dot{m}_s^I$ calculated using equation (6.13) were corrected by dividing them by their form factor to get:

$$\dot{m}_s^I = 7.8\ 10^4\ I_{13}^{0.72} \qquad g\ cm^{-2}\ s^{-1} \tag{6.23a}$$

$$\dot{m}_s^I = 8.2\ 10^4\ I_{13}^{0.86} \qquad g\ cm^{-2}\ s^{-1} \tag{6.23b}$$

for $\lambda = 0.53\ \mu m$ and $1.054\ \mu m$ respectively. The form factor for the trapezoidal pulse used in the simulations was 1.015 and 1.006 for the

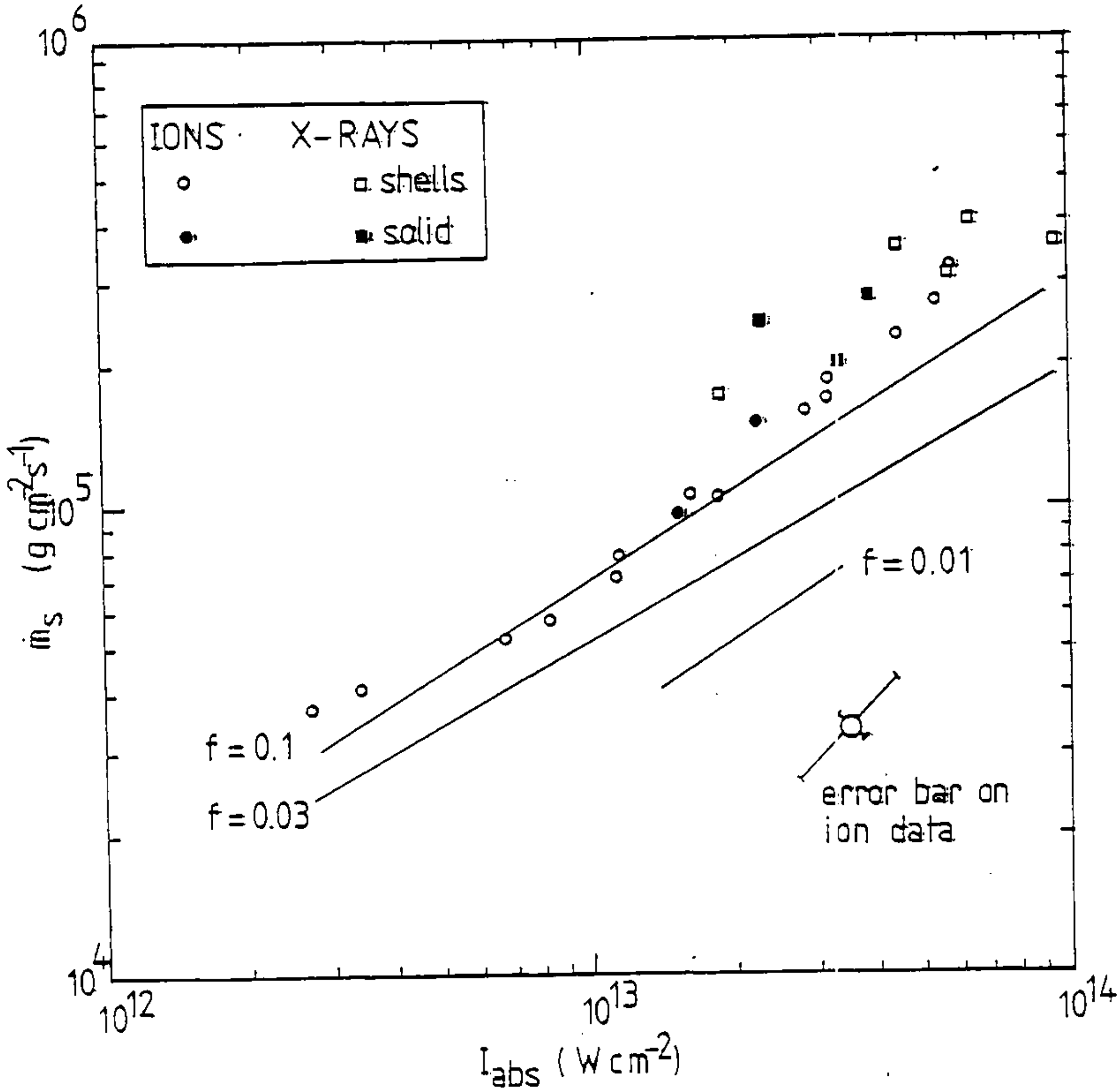

Fig. 6.5. Specific mass ablation rate versus absorbed irradiance for λ = 0.53 μm illumination. Simulation results are shown for flux limits of f = 0.01, 0.03 and 0.1.

two wavelengths using the 100 picosec rise time pulse and 1.08 for the 500 picosec rise time pulses.

<u>6.2.4.2 Results</u>. Figures 6.5 and 6.6 show the $\dot{m}_s$ results of Goldsack et al.(6.27) compared with simulations using 10%, 3% and 1% flux limiters. Figs. 6.7 and 6.8 compare the mean ion velocity measured in the experiments with the simulation values.

It is evident from the comparison that a flux limit of 3% does not produce results agreeing with the experiment. A flux limit of 10% produces much better agreement for the two observables in both 0.53 μm and 1.054 μm experiments. At higher irradiance agreement is poor possibly because of some other energy transfer process such as radiation transport. A flux limit of 10% or greater of the free streaming limit is in disagreement with most but not all(6.29)(6.30) previous experiments measuring the flux limit, however the experiments which disagree with this result were on planar targets dominated by edge effects. Heat fluxes in excess of 10% of free streaming have been predicted by two recent independent theories(6.31)(6.32) for heat conduction in non-turbulent plasmas.

<u>6.2.5 Discussion of Errors</u>

The simulations have been compared with the first experiments measuring a heat flux dependent quantity that are uncomplicated by edge losses or other factors. The spherical geometry of the experiments meant that average quantities such as absorbed energy and ablation rate could be calculated from a large number of separate detectors. The relationship between absorbed energy and ablation rate meant that the results are affected little by errors in the calibration of the plasma

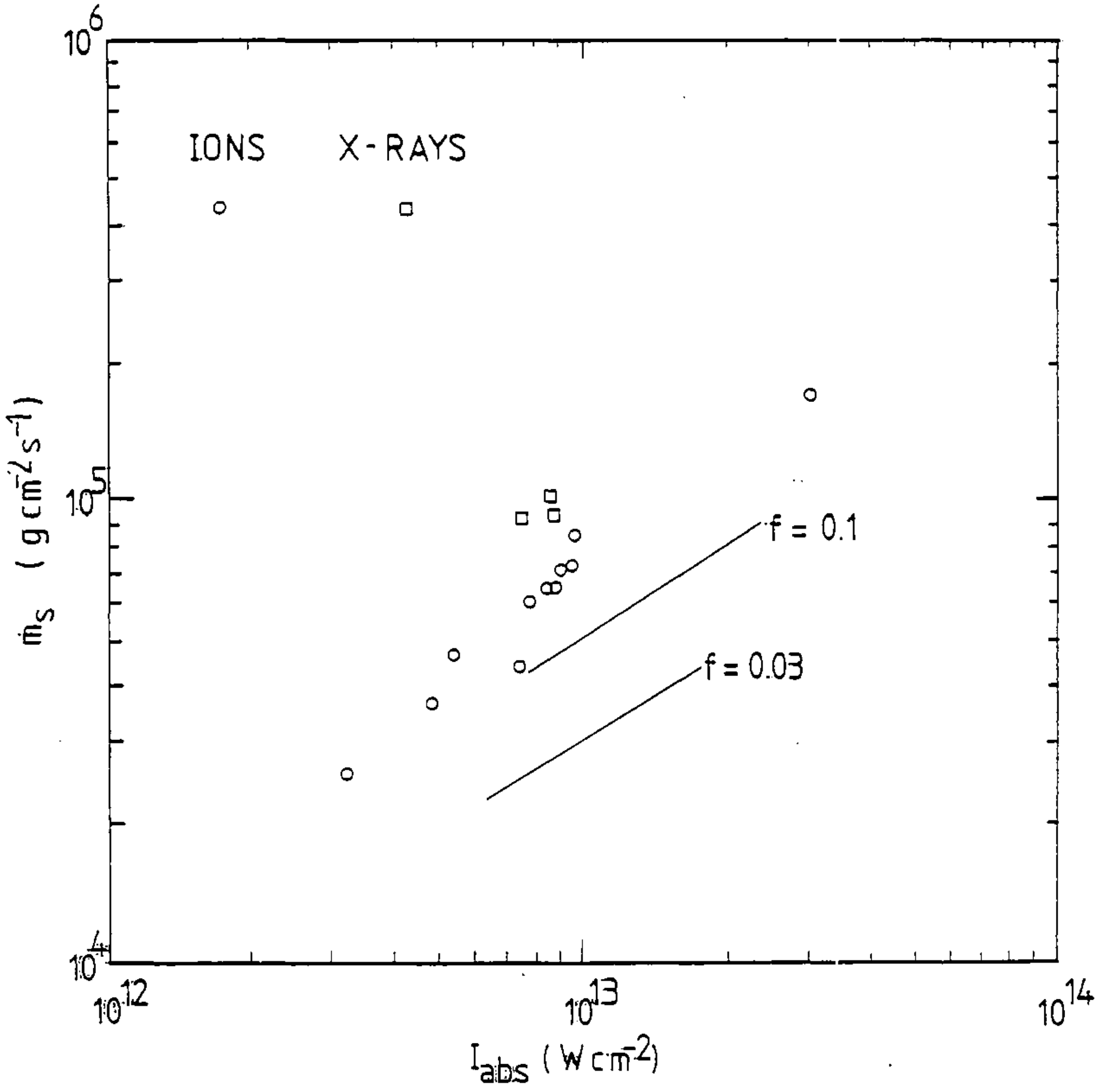

Fig. 6.6. Specific mass ablation rate versus absorbed irradiance of λ = 1.054 μm illumination. Simulation results are shown for flux limits of f = 0.03 and 0.1.

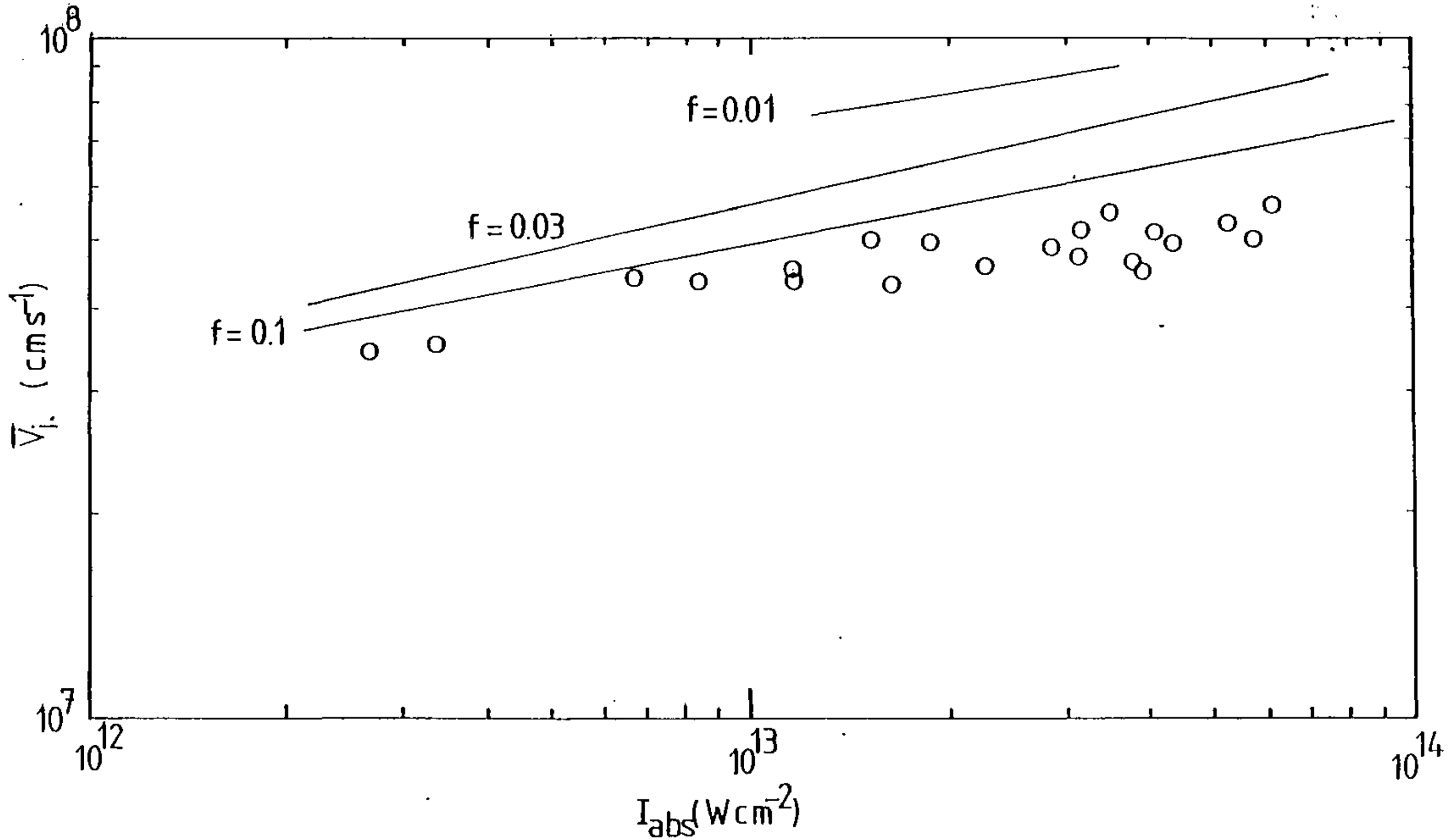

Fig. 6.7. Mean velocity of ablated ions for λ = 0.53 μm illumination.

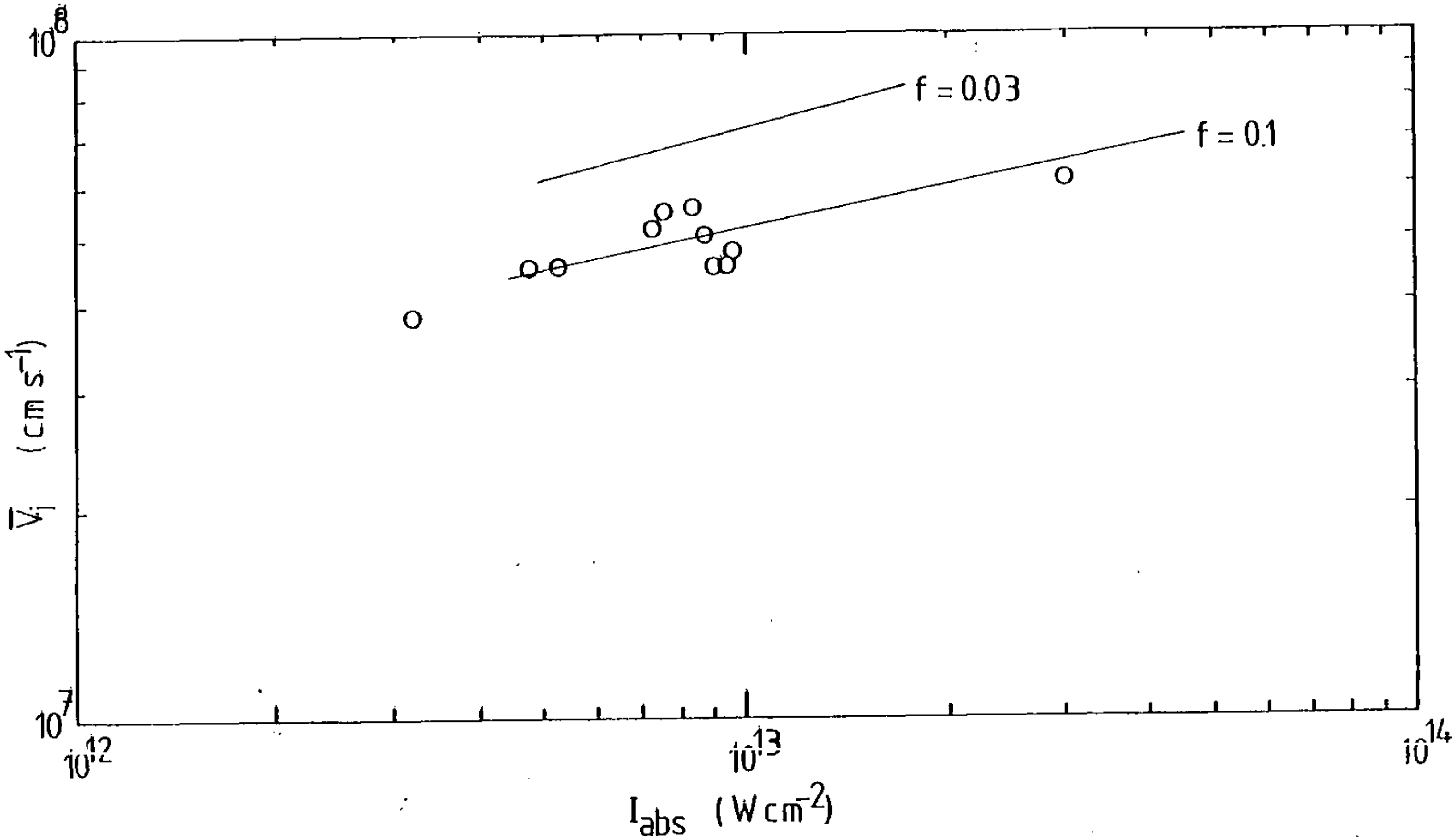

Fig. 6.8. Mean velocity of ablated ions for λ = 1.054 μm illumination.

calorimeters.

The chief source of error in the measurement of the ablation rate would therefore be in the determination of the ion velocity $\bar{v}$ used in equation (6.13). The flight time of the ions was determined to an accuracy of better than 5% contributing an error of 7% to the ablation rate determination. The full width of the ion velocity spectrum for any one shot was typically 17% of the mean value[6.28] making the mean velocity a reasonable quantity to use to calculate $\dot{m}$.

Errors due to poor focusing of the laser beams can be discounted as any irregularity in the illumination would show up as a local enhancement of mass ablation rate or absorbed energy. Any shots where an inconsistency of greater than 20% in the signals from the calorimeters or Faraday cups was observed, were discarded. X-ray pinhole pictures were also used as a check on illumination uniformity.

Shortcomings in the simulations include the neglect of radiation transfer and incomplete treatment of fast electron transport. Enhancement of the mass ablation rate due to transport of energy to high density by radiation or fast electrons could explain the relatively poor agreement between simulation and experiment at high intensity. The high Z fiducial Aluminium layer on the outside of the target will produce X-rays that will penetrate the low attenuation plastic layer to reach the underlying glass. Fig. 6.9 is an example of a time-resolved X-ray spectrum showing a delay between the Aluminium and Silicon lines. An interesting feature of this streak is that there is a precursor to the main emission of the satellites of Si XIII $1s^2\ {}^1S_0$ - $1s2p\ {}^1P_1$. A possible explanation for the occurrence of the precursor is radiation from the Aluminium heating the glass. The precursor emission is seen to disappear after the Aluminium lines lose their intensity and hence

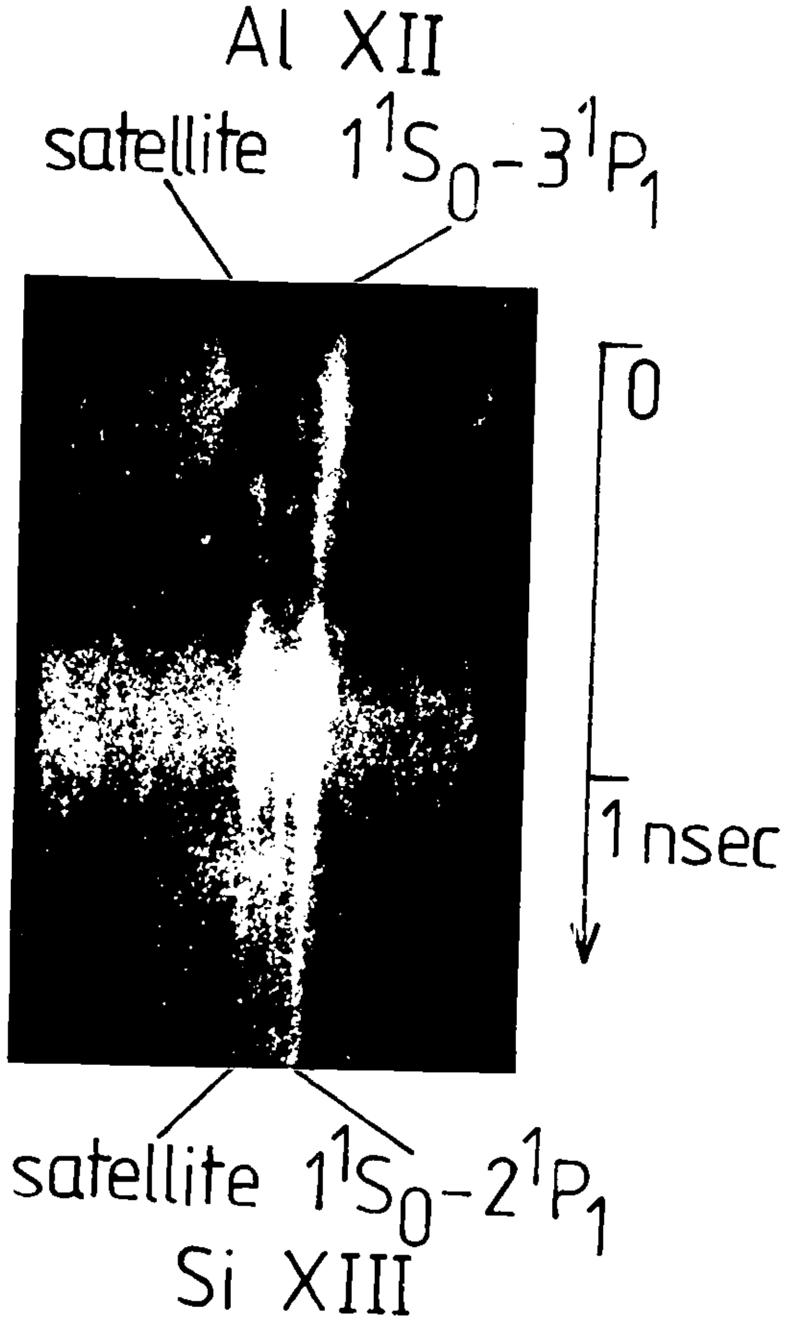

Fig. 6.9. A time-resolved X-ray spectrum from an Aluminium and Plastic coated glass microballoon. The precursor emission of the satellite to the Silicon resonance line is visible 300 picoseconds from the start of the pulse.

cannot supply so much energy to the Silicon in the glass. The precursor is not likely to be due to a defective target coating or filamentation of the laser beam, as if that were the case the Silicon emission would not switch off after the Aluminium has been removed as is seen to happen.

Radiation transport will be of greater importance at high intensity in the $\lambda = 0.53$ μm simulations where the disagreement is most marked.

The treatment of fast electron transport neglects the strong electric fields which will retard the progress of the hot electrons into the target, scattering of hot electrons is also neglected. Hence the fast electron range is greater than it should be by a factor of two or three. The highest $I\lambda^2$ incident in the green experiment was $4\ 10^{13}$ W cm^2 μm^2 indicating(6.09) a hot electron temperature of 2 keV which is comparable to the temperature at critical density. Therefore fast electron transport will be negligible compared with thermal transport for the $\lambda = 0.53$ μm experiment. The $\lambda = 1.054$ experiment had a peak $I\lambda^2$ of $2\ 10^{14}$ W cm^{-2} μm^2 giving $T_H \simeq 4$ keV. Fast electron transport will be more significant in the 1.054 μm experiment and could be the reason for the high values of $\dot{m}_s$ compared with the simulations in Fig. 6.6. However a complete neglect of fast electrons in the 1.054 μm simulations only affects the ablation rate by at most 20% implying that improved modelling of suprathermal electron transport would affect the results only by this amount.

6.2.6 Conclusion

Results of measurements of mass ablation rate and ablation velocity, where the spherical geometry has for the first time eliminated the possibility of lateral power loss, have been compared with the MEDUSA simulation code. It has been observed that a flux limit of f = 0.03 does not describe the experiment. A higher flux limit of f = 0.1 gives better agreement although some extra energy transport process, probably radiation transport, increases the ablation rate above that predicted by simulation at higher intensity. Heat fluxes in excess of 10% of free streaming in non-turbulent plasma have been predicted by two recent theoretical treatments[6.31][6.32].

The MEDUSA code has been extended to allow simulation of irradiation of spherical targets where multibeam illumination makes refraction of the laser an important process. The action of beam refraction in depositing energy at lower density leads to a reduced ablation rate compared with simulations neglecting refraction.

CHAPTER 7

CONCLUSION

7.0 Abstract

The motivation for the work is explained and a brief summary of the high energy lasers currently in use, or planned, is given. The importance of the results of this thesis is stated.

7.1 Introduction: Motivation for this Work

Considerable effort is currently being directed towards the study of laser driven compression. One reason for interest in laser compression is the possibility of using it to generate thermonuclear power in an inertial confinement fusion (ICF) reactor. The confinement of a D-T plasma at thermonuclear ignition temperature could be the basis of a power generation plant which would have several advantages over fission power stations currently in use. Some of the undesirable aspects of nuclear fission are:

(i) environmental hazards caused by transport and storage of fissile materials and long-lived ($\sim 10^4$ years) radioactive waste products;

(ii) the possibility of an accident at a nuclear plant contaminating large areas and rendering them uninhabitable;

(iii) proliferation of nuclear weapons due to the possible production of Plutonium as a by-product of any commercial reactor, or through use of high grade Uranium fuel directly as weapons material;

(iv) the transport of fissile materials making their diversion and use for criminal purposes a possible risk.

A nuclear fusion reactor would produce relatively short lived waste products which would present few storage problems. The fuel would consist of Deuterium and Tritium which could have few environmental hazards if handled correctly. Deuterium, which could be refined from sea water, is harmless (unless consumed in large quantities), whilst Tritium could be manufactured in a closed cycle within the fusion reactor, reducing the need for transporting the radioactive isotope.

Proliferation of nuclear weapons would not be encouraged as much as with fission reactors. Unless Plutonium is bred deliberately, using neutrons from the fusion reactor, no suitable materials for bomb manufacture will be at, or transported between, reactor sites.

Inertial confinement fusion also has been proposed using alternatives to lasers as 'drivers'. The use of ion beams (both heavy and light ions), X-rays and electron beams have all been considered. The relative merits of the different types of driver for ICF are discussed in a paper by Mead[7.01]. The state of research in only laser driven ICF (which is more advanced than for alternative drivers) will now be described.

7.2 High Power Lasers

The number of laboratories capable of doing laser driven compression experiments is limited. Laboratories in the USA dominate research in this field in terms of laser powers available.

The leading laboratory in the USA is Lawrence Livermore National Laboratory (LLNL), which is currently building the largest Nd-doped glass laser in the world. This laser (Novette) will be a two-beam system capable of supplying pulses of 20 kJ of 1 μm wavelength energy and 14 kJ of frequency-doubled 0.53 μm radiation. Novette will be completed in 1982 and will serve as a test bed for the next stage of the USA's ICF programme, which is the 10-beam Nova laser. Nova will (if it is built) provide energies of 100 - 200 kJ at 1 μm, slightly less when frequency doubled. Nova is planned to be completed in 1985. The Shiva laser was put out of service last year after experiments using up to 20 kJ of energy were performed. Currently LLNL has no operating laser engaged in ICF research.

Los Alamos National Laboratory (LANL) in the USA has a CO_2 laser (λ = 10.6 μm) called Helios which produces several kJ of energy in eight beams. The problems caused by fast electron generation, due to the very long wavelength of the laser, make the achievement of high densities with this laser unlikely.

The Laboratory of Laser Energetics (LLE) at the University of Rochester, USA, has a 24-beam Nd glass system which has produced 2 kJ of 1.054 μm radiation. Ablative compression experiments have been performed using this laser to implode thick-walled balloons. Compressed densities up to 6 g cm^{-3} have been diagnosed spectroscopically in radiatively-cooled exploding pusher experiments[7.02]. Plans have been formulated to frequency triple the beams in order to use 0.35 μm radiation for implosion experiments. However preliminary work will be performed using only six 0.35 μm beams possibly in combination with 1.054 μm wavelength beams.

The two-beam Nd glass laser at KMS Fusion has been frequency-doubled to allow 0.53 μm compression experiments using their TBIS 4π illumination system.

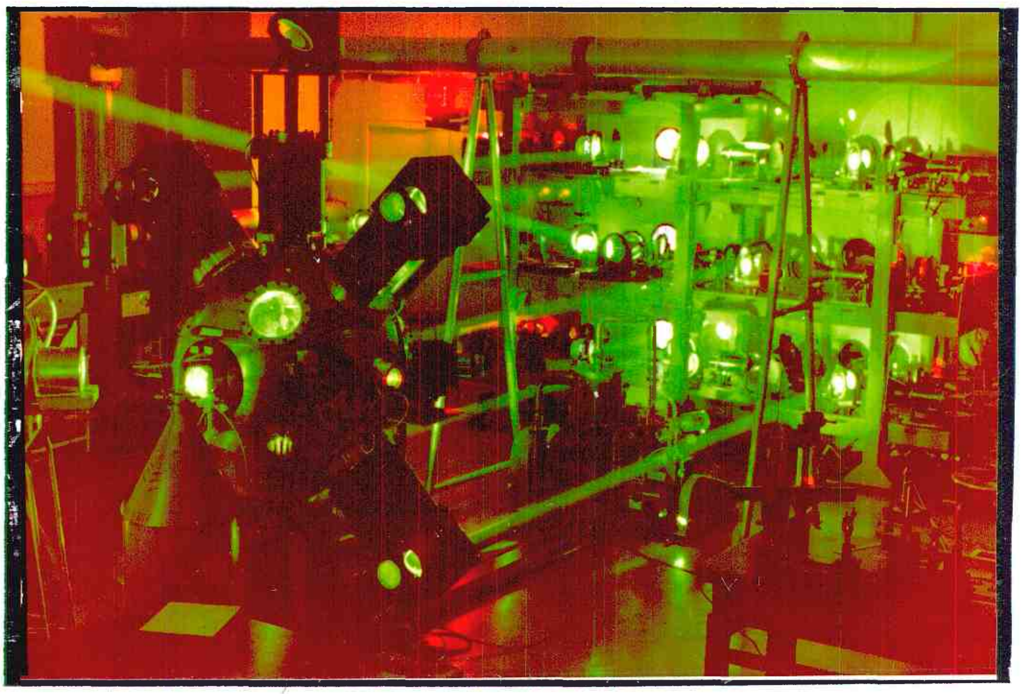

Fig. 7.1. Photograph of the six-beam target area at Rutherford Appleton Laboratory during the λ = 0.53 μm implosion experiment described in Chapter 4. The ½-nanosecond pulse has been time-smeared by the camera.

Picture Steve Knight (Rutherford Appleton Laboratory)

Outside the USA the major contributor the ICF effort is Japan. The 'Kongoh' project at the University of Osaka has a 4-beam, 4 TW laser operating at 1.054 μm and 0.53 μm. A 12-beam system able to supply 30 kJ of energy is planned to be completed at the end of 1982.

In the United Kingdom, Rutherford Appleton Laboratory has a six-beam 0.53 μm facility (described in parts of this thesis) capable of supplying 200J on target in a ½-nanosecond pulse. The laser energy will be doubled in February 1983 when further amplifiers will be added. Fig. 7.1 is a photograph of the Rutherford Appleton Laboratory six-beam target area, taken during the λ = 0.53 μm implosion experiment described in Chapter 4.

7.3 Contribution of this Thesis

The work described in this thesis has been of direct relevance to the ICF programme. The results in Chapter 2 have important consequences for both the subject of fast electron behaviour and analysis of model experiments performed in planar geometry. The implosion experiments described were the first symmetric ablative compressions using 0.53 μm irradiation. Further experiments in direct drive laser ICF will be using short wavelength lasers (e.g. LLE Rochester) for ablative compressions and so this work has been a preliminary examination of the problems involved. In particular, the use of polystyrene targets will be of importance in future experiments.

The modelling of compressions in order to predict the behaviour of different target/laser combinations must be done using good estimates of the transport processes in the implosion. The conclusions regarding the limits on the heat flux possible in laser-irradiated targets are thus important for planning of experiments. The assumption of a flux limit of 3%, or less, of the free streaming flux has been shown to disagree with ablation rate data obtained in spherical geometry experiments. A flux limit nearer 10% more accurately describes the energy transport in these experiments. Therefore a flux limit of 10% should be used in simulations of future laser-driven compression experiments.

Future experiments will be done at Rutherford Appleton Laboratory using 0.53 μm light to implode thick plastic shells. The implosion uniformity can be improved by use of layered targets to investigate irregularities in shell acceleration. It is possible that 12 beams will eventually be used if the six-beam geometry in current use is not conducive to uniform implosions. The problem of radiative preheat causing pusher decompression could be reduced if thicker shells are used. A high Z element could be coated near the surface of the target to act as a radiation screen.

REFERENCES

CHAPTER 1

1.01 J. Nuckolls, L. Wood, A. Thiessen and G. Zimmerman, Nature 239 (1972) 139.

1.02 M. H. Key, 'Lectures on the Physics of the Super Dense Region', 20th Scottish Universities Summer School in Physics: Laser Plasma Interactions, St. Andrews (1979).

1.03 T. J. Goldsack, J. D. Kilkenny, B. J. MacGowan, S. A. Veats, P. F. Cunningham, C. L. S. Lewis, M. H. Key, P. T. Rumsby and W. T. Toner, Opt. Comm. 42(1) (1982) 55.

1.04 T. J. Goldsack, J. D. Kilkenny, B. J. MacGowan, P. F. Cunningham, C. L. S. Lewis, M. H. Key and P. T. Rumsby, Phys. Fluids 25(9) (1982) 1634.

1.05 Amiranoff et al., Phys.Rev.Lett. 43 (1979) 522; Yaakobi et al., Opt.Comm. 39 (1981) 178.

1.06 J. Grun, R. Decoste, B. H. Ripin and J. Gardner, Appl.Phys.Lett. 39 (1981) 545.

1.07 Key et al., Phys.Fluids (in press)

1.08 C. E. Max, C. F. McKee and W. C. Mead, Phys.Fluids 23(8) (1980) 1620.

1.09 C. Fauquignon and F. Floux, Phys.Fluids 13 (1970) 386.

1.10 K. G. Estabrook, E. J. Valeo, W. L. Kruer, Phys.Fluids 18 (1975) 1151.

1.11 D. W. Forslund, J. M. Kindel, K. Lee, E. L. Lindman, R. L. Morse, Phys.Rev.A 11 (1975) 679.

CHAPTER 1 (continued)

1.12 T. W. Johnston and J. M. Dawson, Phys.Fluids 16(5) (1973) 722.

1.13 L. Spitzer, R. Harm, Phys.Rev. 89 (1953) 977.

1.14 L. Spitzer, 'Physics of Fully Ionised Gases', New York: Interscience, 1956.

1.15 S. I. Braginskii, Rev.Plasma Phys. 1 (1965) 249.

1.16 A. R. Bell, R. G. Evans and D. J. Nicholas, Phys.Rev.Lett. 46 (1981) 247.

1.17 D. J. Bond, Bull.Am.Phys.Soc. 26 (1981) 856;
D. J. Bond, Phys.Lett.A 88 (1982) 144.

1.18 E. S. Wyndham, J. D. Kilkenny, H. H. Chuaqui and A. K. L. Dymoke-Bradshaw, J.Phys.D. 15 (1982) 1683.

1.19 J. D. Hares, J. D. Kilkenny, M. H. Key and J. G. Lunney, Phys.Rev.Lett. 42 (1979) 1216.

1.20 F. Amiranoff, R. Benattar, R. Fabbro, E. Fabre, C. Garban and M. Weinfeld, Bull.Am.Phys.Soc. 24 (1979) 1054.

1.21 B. Ahlborn, M. H. Key and A. R. Bell, Phys.Fluids 25(3) (1982) 541.

1.22 D. J. Bond, J. D. Hares and J. D. Kilkenny, Phys.Rev.Lett. 45 (1980) 252.

1.23 D. J. Bond, J. D. Hares and J. D. Kilkenny, Plasma Phys. 24 (1982) 91.

1.24 H. D. Shay, R. A. Haas, W. L. Kruer, M. J. Boyle, D. W. Phillion, V. C. Rupert, H. N. Kornblurn, F. Rainer, V. W. Slivinsky, L. N. Koppel, L. Richards and K. G. Tirsell, Phys.Fluids 21 (1978) 1634.

1.25 R. W. Lee, J.Q.R.T., 26 (1981) 87; 27 (1982) 243; 27 (1982) 249.

CHAPTER 1 (continued)

1.26 B. I. Bennett, J. D. Johnson, G. I. Kerley and G. T. Rood, Los Alamos Report, LA 7130 (1978).

1.27 E. K. Storm, J. T. Larsen, J. M. Nuckolls, H. G. Ahlstroom and K. R. Manes, UCRL 78788 (1977).

1.28 M. D. Rosen and J. H. Nuckolls, UCRL 81343 (1977); M. D. Rosen and J. H. Nuckolls, Phys.Fluids 22 (1979) 1293.

1.29 B. Ahlborn and M. H. Key, Plasma Phys. 23 (1981) 435.

1.30 Storm et al., Phys.Rev.Lett. 40 (1980) 1570.

1.31 Giovanelli et al., 'Proc. IEEE Int. Conf. on Plasma Sciences, Austin, Texas 1976', IEEE, New York, 1976.

1.32 J. Launspach, D. Billon, M. Decroisette and D. Meynial, Optics Comm. 38 (1981) 407.

1.33 M. Richardson, Inst.Phys. Plasma Physics Conference, Oxford 1982.

1.34 R. G. Evans, A. J. Bennet and G. J. Pert, J.Phys.D. (Appl.Phys.) 15 (1982) 1673.

1.35 J. H. Gardner and S. E. Bodner, Phys.Rev.Lett. 47 (1981) 1137.

1.36 A. J. Cole, J. D. Kilkenny, P. T. Rumsby, R. G. Evans and M. H. Key, J.Phys.D. (Appl.Phys.) 15 (1982) 1689.

1.37 Cole et al., Nature 299 (1982) 329.

1.38 J. D. Lawson, Proc.Phys.Soc.(London)B 70 (1957) 6.

CHAPTER 2

2.01 J. P. Freidberg, R. W. Mitchell, R. L. Morse and L. I. Rudinski, Phys.Rev.Lett. 28 (1972) 795.

CHAPTER 2 (continued)

2.02 D. W. Forslund, J. M. Kindel, K. Lee, E. L. Lindman and R. L. Morse, Phys.Rev.A 11(2) (1975) 679.

2.03 D. V. Giovanelli et al., 'Proc. of IEEE Int. Conf. on Plasma Science, Austin, Texas, 1976', IEEE, New York, 1976; B. H. Ripin et al., NRL Report No. 3315, 1976, pp 100-177; F. C. Young et al., Appl.Phys.Lett. 30 (1977) 45; P. Kolodner and E. Yablonovitch, Phys.Rev.Lett. 37 (1976) 1754.

2.04 L. M. Wickens, J. E. Allen and P. T. Rumsby, Phys.Rev.Lett. 41 (1978) 243.

2.05 D. W. Forslund, J. M. Kindel, K. Lee, Phys.Rev.Lett. 39 (1977) 284.

2.06 E. Fabre et al., Paper IAEA-CN-38/1-4, Brussels (1980).

2.07 E. H. Goldman, J. A. Delettrez, E. I. Thorsos, Nuclear Fusion 19 (1979) 555.

2.08 Rapport d'Activité 1979, p80, Groupement de Recherches Coordonnées Interaction Laser Matière, Ecole Polytechnique, 91128 Palaiseau.

2.09 F. J. Mayer et al., 14th ECLIM, Palaiseau 1980 (unpublished); PLF Garching report, PLF 41 (1980).

2.10 S. Witkowski et al., 14th ECLIM, Palaiseau 1980 (unpublished).

2.11 J. D. Hares and J. D. Kilkenny, J.Appl.Phys. 52 (1981) 6420.

2.12 J. D. Hares, J. D. Kilkenny, M. H. Key and J. G. Lunney, Phys.Rev.Lett. 42(18) (1979) 1216.

2.13 D. K. Bradley, Private Communication (1981).

2.14 N. A. Ebrahim et al., Phys.Rev.Lett. 43 (1979) 1995.

2.15 P. A. Jaanimagi et al., Appl.Phys.Lett. 38 (1981) 734.

CHAPTER 2 (continued)

2.16 R. Decoste, J. C. Kieffer and H. Pepin, Phys.Rev.Lett. 47 (2981) 35.

2.17 Campbell et al., Phys.Rev.Lett. 39 (1977) 274;
Basov et al., IPPLM Report No. 3780(57), Presented at 14th ECLIM, Palaiseau, France (1980).

2.18 D. W. Forslund and J. U. Brackbill, Phys.Rev.Lett. 48(23) (1982) 1614.

CHAPTER 3

3.01 Yaakobi et al., Phys.Rev.Lett. 44 (1980) 1072;
S. Skupsky, Phys.Rev.A 21 (1980) 1316;
Kilkenny et al., Phys.Rev. A 22 (1980) 2746;
J. G. Lunney and J. F. Seely, Phys.Rev.Lett. 46 (1981) 342.

3.02 J. G. Lunney, Queen's University, Belfast, Ph.D. Thesis (1980).

3.03 Annual Report to the CLF RL-81-040 (1981).

3.04 B. Yaakobi and V. Bhagavatula, LLE Report #89 (June 1979).

3.05 L. Von-Hamos, Z. Kirstallog. 101 (1939) 17;
C. B. Van den Berg and M. Brinkman, Physica 21 (1955) 85.

CHAPTER 4

4.01 J. Nuckolls, L. Wood, A. Thiessen and G. Zimmerman, Nature 239 (1972) 139.

4.02 R. E. Kidder, Nucl.Fusion 16 (1976) 3.

CHAPTER 4 (continued)

4.03 Storm et al., Phys.Rev.Lett. 40 (1980) 1570.

4.04 Forslund et al., Phys.Rev.Lett. 39 (1977) 284.

4.05 K. Estabrook and W. L. Kruer, Phys.Rev.Lett. 40 (1978) 42.

4.06 Hares et al., Phys.Rev.Lett. 42 (1979) 1216.

4.07 Amiranoff et al., Bull.Am.Phys.Soc. 24 (1979) 1054.

4.08 B. Ahlborn, M. H. Key and A. R. Bell, Phys.Fluids 25(3) (1982) 541.

4.09 Goldsack et al., Phys.Fluids 25(9) (1982) 1634.

4.10 D. E. T. F. Ashby, J. P. Christiansen and K. V. Roberts, Comput.Phys.Commun. 7 (1974) 271.

4.11 Yu. B. Zeldovich and Yu. P. Raizer, "Physics of Shock Waves and High Temperature Hydrodynamic Phenomena", (Academic, New York, 1967) Vols.I and II.

4.12 Handbook of Spectroscopy, Vol.1, C.R.C. Press (Ohio 1974), e.g. p202.

4.13 Haas et al., Phys.Fluids 20(2) (1977) 322.

4.14 Shay et al., Phys.Fluids 21(9) (1978) 1634.

4.15 Mead et al., Phys.Rev.Lett. 37(8) (1976) 489.

4.16 Mead et al., Phys.Rev.Lett. 47(18) (1981) 1289.

4.17 Bennett et al., Los Alamos Scientific Laboratory Report LA-7130 (1978).

4.18 Evans et al., J.Phys.D.(Appl.Phys.) 15 (1982) 711.

4.19 J. D. Hares and J. D. Kilkenny, J.Appl.Phys. 52 (1981) 6420.

4.20 R. G. Evans, A. J. Bennett and G. J. Pert, J.Phys.D (Appl. Phys.) 15 (1982) (in press).

4.21 J. H. Gardner and S. E. Bodner, Phys.Rev.Lett. 47(16) (1981) 1137.

CHAPTER 4 (continued)

4.22 C. E. Max, C. F. McKee, W. C. Mead, Phys.Fluids 23(8) (1980) 1620.

4.23 Cole et al., J.Phys.D. (Appl.Phys.) 15 (1982) 1689.

4.24 J. G. Lunney, Ph.D. Thesis, Queen's University, Belfast, 1980.

4.25 L. L. House, Astro.Journ.Supp.Series No. 155 18 (1969) 21.

4.26 J. C. Stewart and K. D. Pyatt, Astrophys.J. 144 (1966) 1203.

4.27 W. T. Toner, Private Communication (1982).

4.28 A. P. Fews and D. L. Henshaw, Proc. 11th Int. Conf. on Solid State Nuclear Track Detectors, Bristol, U.K. (1981).

4.29 Young et al., Phys.Rev.Lett. 49 (1982) 549.

4.30 A. P. Fews, Ph.D. Thesis, Bristol University, 1982.

4.31 M. H. Key, Private Communication (1982).

CHAPTER 5

5.01 J. G. Lunney, Ph.D. Thesis, Queen's University, Belfast, 1980.

5.02 J. D. Kilkenny, R. W. Lee, M. H. Key and J. G. Lunney, Phys.Rev. A 22 (1980) 2746.

5.03 A. K. Pradhan, D. W. Norcross and D. G. Hummer, Astro.J. 246 (1981) 1031.

5.04 R. W. Lee, Private Telecommunication (1982).

5.05 B. Ahlborn and M. H. Key, Plasma Phys. 23 (1981) 435.

5.06 Calculation using a code (PLASMA) kindly made available by Dr. A. Pritzker (1982).

5.07 J. G. Lunney and J. F. Seely, Phys.Rev.Lett. 46 (1981) 342; J. F. Seely, Atomic Data and Nuclear Data Tables 26 (1981) 137.

CHAPTER 5 (continued)

5.08 J. H. Schofield, UCID 16848 (1975).

5.09 J. C. Stewart and K. D. Pyatt, Astrophys.J. 144 (1966) 1203.

5.10 D. R. Inglis and E. Teller, Astrophys.J. 90 (1939) 439.

CHAPTER 6

6.01 D.E.T.F. Ashby, J. P. Christiansen and K. V. Roberts, Comput.Phys.Commun. 7 (1974) 271.

6.02 L. Spitzer, 'Physics of Fully Ionised Gases', New York: Interscience, 1956.

6.03 Yu. B. Zeldovich and Yu. P. Raizer, 'Physics of Shock Waves and High Temperature Phenomena', Vols.I and II, New York: Academic, 1967.

6.04 R. Latter, Phys.Rev. 99 (1955) 1854.

6.05 D. A. Kirzhnits, Sov.Phys. - JETP 8 (1958) 1081.

6.06 B. I. Bennett, J. D. Johnson, G. I. Kerley and G. T. Rood, Los Alamos Report LA7310 (1978).

6.07 A. R. Bell and R. G. Evans, 'Laser Advances and Applications' ed. R. S. Wherret (Proc.4th Nat. Quantum Electronics Conf. Edinburgh), Chichester: Wiley, 1979.

6.08 D. V. Giovanelli, G. H. McCall and A. H. Williams, 'Proc. IEEE Int. Conf. on Plasma Science, Austin, Texas, 1976', New York: IEEE, 1976.

6.09 D. W. Forslund, J. M. Kindel and K. Lee, Phys.Rev.Lett. 39 (1977) 284.

CHAPTER 6 (continued)

6.10 'NRL Plasma Formulary', ed. D. L. Book, Naval Research Laboratory, Washington, DC 20375;
R. G. Evans, CLF Annual Report, 1980.

6.11 V. L. Ginzburg, 'Propagation of Electromagnetic Waves in Plasmas', Pergamon, New York, 1970.

6.12 Young et al., Appl.Phys.Lett. 30 (1977) 45.

6.13 J. G. Kephart, R. P. Godwin and G. H. McCall, Appl.Phys.Lett. 25 (1974) 108.

6.14 Ripin et al., Phys.Rev.Lett. 34 (1974) 1313.

6.15 Key et al., Appl.Phys.Lett. 34 (1979) 550.

6.16 Key et al., Phys.Rev.Lett. 41 (1978) 1467.

6.17 R. G. Evans, A. R. Bell, B. J. MacGowan, J.Phys.D. 15 (1982) 711.

6.18 C. E. Max, C. F. McKee, W. C. Mead, Phys.Fluids 23(8) (1980) 1620.

6.19 T. W. Johnston and J. M. Dawson, Phys.Fluids 16 (1973) 722.

6.20 Forslund et al., Phys.Rev.A 11(2) (1975) 679.

6.21 D. Tanner, KMS Fusion Inc., Annual Report 1979.

6.22 T. J. Goldsack et al., Opt.Comm. 42(1) (1982) 55;
R. C. Malone et al., Phys.Rev.Lett. 34 (1975) 721;
J. Murdoch et al., Phys.Fluids 24 (1981) 2107;
D. R. Gray et al., 'Laser Advances and Application', ed. B. Wherrett, p211, J. Wiley 1980.

6.23 B. Yaakobi and T. C. Bristow, Phys.Rev.Lett. 38 (1977) 350;
F. C. Young et al., Appl.Phys.Lett. 30 (1977) 45.

6.24 A. Zigler, H. Smora and J. L. Schwob, Phys.Lett. 63A (1977) 275.

CHAPTER 6 (continued)

6.25 T. J. Goldsack, J. D. Kilkenny and P. T. Rumsby, J.Phys.D. Appl Phys. 14 (1981) 147.

6.26 W. C. Mead et al., Phys.Rev.Lett. 47 (1981) 1289.

6.27 T. J. Goldsack et al., Phys.Fluids 25(9) (1982) 1634.

6.28 T. J. Goldsack, Ph.D. Thesis, University of London, 1982.

6.29 E. S. Wyndham et al., submitted to J.Phys.D 1982.

6.30 P. A. C. Moore, J.Phys.D. Appl.Phys. 14 (1980) 1429.

6.31 A. R. Bell, R. G. Evans and D. J. Nicholas, Phys.Rev.Lett. 46 (1981) 247.

6.32 D. J. Bond, B.A.P.S. 26 (1981) 856;
D. J. Bond, Phys.Lett. 88A (1982) 144.

6.33 K. R. Manes et al., Phys.Rev.Lett. 39 (1977) 281.

6.34 R. G. Evans, Private Communication (1981);
also CLF Annual Report 1978.

6.35 Goldsack et al., Optics Comm. 42 (1982) 55.

CHAPTER 7

7.01 W. C. Mead, U.C.R.L. 82426.

7.02 Yaakobi et al., Phys.Rev.Lett. 44 (1980) 1072.